

Computational analysis of cell orientation in response to mechanical stimuli : implications for myocardial repair strategies

Citation for published version (APA):

Obbink - Huizer, C. (2014). *Computational analysis of cell orientation in response to mechanical stimuli : implications for myocardial repair strategies*. [Phd Thesis 1 (Research TU/e / Graduation TU/e), Biomedical Engineering]. Technische Universiteit Eindhoven. <https://doi.org/10.6100/IR780939>

DOI:

[10.6100/IR780939](https://doi.org/10.6100/IR780939)

Document status and date:

Published: 01/01/2014

Document Version:

Publisher's PDF, also known as Version of Record (includes final page, issue and volume numbers)

Please check the document version of this publication:

- A submitted manuscript is the version of the article upon submission and before peer-review. There can be important differences between the submitted version and the official published version of record. People interested in the research are advised to contact the author for the final version of the publication, or visit the DOI to the publisher's website.
- The final author version and the galley proof are versions of the publication after peer review.
- The final published version features the final layout of the paper including the volume, issue and page numbers.

[Link to publication](#)

General rights

Copyright and moral rights for the publications made accessible in the public portal are retained by the authors and/or other copyright owners and it is a condition of accessing publications that users recognise and abide by the legal requirements associated with these rights.

- Users may download and print one copy of any publication from the public portal for the purpose of private study or research.
- You may not further distribute the material or use it for any profit-making activity or commercial gain
- You may freely distribute the URL identifying the publication in the public portal.

If the publication is distributed under the terms of Article 25fa of the Dutch Copyright Act, indicated by the "Taverne" license above, please follow below link for the End User Agreement:

www.tue.nl/taverne

Take down policy

If you believe that this document breaches copyright please contact us at:

openaccess@tue.nl

providing details and we will investigate your claim.

Computational analysis of cell orientation in response to mechanical stimuli; implications for myocardial repair strategies

Christine Obbink-Huizer

$$f_{\varepsilon,p}(\varepsilon\theta) = \begin{cases} 0 & \text{if } \varepsilon < 0 \\ \left(\frac{\varepsilon\theta}{\varepsilon_1}\right)^2 & \text{if } \varepsilon \geq 0 \end{cases}$$

$$\sigma_{\theta}^p = \sigma_{\max} f_{\varepsilon}(\varepsilon\theta) f_{\dot{\varepsilon}}(\dot{\varepsilon}\theta)$$

$$\sigma_{\text{sub}} = \sigma_{\text{NH}} + E_f \lambda_f \vec{e}_f \vec{e}_f$$

$$f_{\dot{\varepsilon}}(\dot{\varepsilon}\theta) = \frac{1}{1 + \frac{2}{\sqrt{5}}} \left(1 + \frac{k_v \dot{\varepsilon} + 2}{\sqrt{(k_v \dot{\varepsilon} + 2)^2 + 1}} \right)$$

$$f_{\text{iso}}(l_c) = \begin{cases} T_0 \tanh^2(a_l(l_c - l_{c0})) & \text{if } l_c \geq l_{c0} \\ 0 & \text{if } l_c < l_{c0} \end{cases}$$

$$\Phi^{\text{tot}} = \Phi^m + \sum_{\theta} w_{\theta} \Phi_{\theta}^p$$

$$f_{\varepsilon,a} = \begin{cases} \exp\left(-\frac{\varepsilon\theta}{\varepsilon_0}\right) & \text{if } 0 < \varepsilon\theta < t_a \\ \exp\left(-\frac{\varepsilon\theta}{\varepsilon_0}\right) \tanh^2\left(\frac{t_a}{\tau_r}\right) & \text{if } t_a < \varepsilon\theta < t_{\max} \\ 0 & \text{if } \varepsilon\theta > t_{\max} \end{cases}$$

$$\sigma_{\text{tot}} = (1 - \rho) \sigma_{\text{nf}} + \rho \sigma_f$$

$$\frac{dl_c}{dt} = (E_a(l_s - l_c) - 1)v_0$$

$$\sigma_a = \frac{l_s}{l_{s0}} f_{\text{iso}}(l_c) f_{\text{twitch}}(t_a, l_s) E_a(l_s - l_c)$$

$$\frac{d\Phi_{\theta}^p}{dt} = (k_0^f + k_1^f \sigma_{\max} f_{\dot{\varepsilon}}) \Phi^m - k_d \Phi_{\theta}^p$$

$$\sigma_{\text{cell}} = \sum_{\theta} w_{\theta} \Phi_{\theta}^p \sigma_{\theta}^p \vec{e}_{\theta} \vec{e}_{\theta}$$

$$S = \sum_{\theta} \frac{FF_{\theta} \cos(2\theta)}{FF_{\theta}}$$

$$\sigma_f = \begin{cases} E_f \varepsilon_f & \text{if } \varepsilon_f \leq 0 \\ 0 & \text{if } \varepsilon_f > 0 \end{cases}$$

$$f_{\dot{\varepsilon}} = \frac{1}{1 + \frac{2}{\sqrt{5}}} \left(1 + \frac{k_v \dot{\varepsilon} + 2}{\sqrt{(k_v \dot{\varepsilon} + 2)^2 + 1}} \right)$$

$$\sigma_{\text{NH}} = \left[\kappa \frac{\ln(J)}{J} \mathbf{I} + \frac{G}{J} (\mathbf{FF}^T - J^{2/3} \mathbf{I}) \right]$$

$$f_{\varepsilon} = f_{\varepsilon,a} + f_{\varepsilon,p}$$

$$\frac{d\Phi_{\theta}^p}{dt} = (k_0^f + k_1^f \sigma_{\max} f_{\varepsilon,a} f_{\dot{\varepsilon}}) \Phi^m - k_d \Phi_{\theta}^p$$

$$\sigma_{\theta}^p = \sigma_{\max} f_{\dot{\varepsilon}}(f_{\varepsilon,a} + f_{\varepsilon,p})$$

$$\sigma = \sigma_p + w_a \sigma_a \vec{e}_f \vec{e}_f$$

$$\sigma_{\text{cell}} = \frac{1}{N} \sum_{\theta} w_{\theta} \Phi_{\theta}^p \sigma_{\theta}^p \vec{e}_{\theta} \vec{e}_{\theta}$$

$$w_a = \begin{cases} k_1 \lambda^2 (\varepsilon - \varepsilon_1)^2 - 1 & \text{if } r > R_1 \\ \frac{r - R_1/2}{R_1/2} & \text{if } R_1/2 < r < R_1 \\ 0 & \text{if } r < R_1/2 \end{cases}$$

$$W = W_v + W_i + W_f = a_5 [\det(\mathbf{F}^T \cdot \mathbf{F}) - 1]^2 + a_0 (\exp^{a_1 I_E^2} + a_2 \mathbf{I} \cdot \mathbf{E} - 1) + a_3 (\exp^{a_4 \mathbf{I} \cdot \mathbf{V}_E^2} - 1)$$

$$f_{\varepsilon,p} = \begin{cases} 0 & \text{if } \varepsilon\theta < 0 \\ \left(\frac{\varepsilon\theta}{\varepsilon_1}\right)^2 & \text{if } \varepsilon\theta \geq 0 \end{cases}$$

$$\sigma_f = \sigma_f \vec{e}_f \vec{e}_f$$

$$\sigma_{\text{nf}} = K \frac{\ln(J)}{J}$$

$$FN = \begin{cases} 0 & \text{if } \lambda_2 \leq 0 \\ \exp^{-2\left(\frac{\lambda_1}{\lambda_2}\right)^2} (1 - \exp^{-c \frac{\lambda_1^2 + \lambda_2^2}{2}}) & \text{if } \lambda_2 > 0 \end{cases}$$

$$\sigma_{\text{cell}} = \sum_{\theta} w_{\theta} \Phi_{\theta}^p \sigma_{\theta}^p \vec{e}_{\theta} \vec{e}_{\theta}$$

$$\vec{\nabla} \cdot \sigma = \vec{0}$$

Christine Obbink-Huizer

**Computational analysis of cell orientation
in response to mechanical stimuli;
implications for myocardial repair
strategies**



A catalogue record is available from the Eindhoven University of Technology Library.

ISBN: 978-90-386-3702-0

© Copyright 2014 by Christine Obbink-Huizer

All rights reserved. No part of this publication may be reproduced, stored in a database or retrieval system, or published, in any form or in any way, electronically, mechanically, by print, photoprint, microfilm or any other means without prior written permission by the author.

Cover design by Christine Obbink-Huizer

Printed by GVO printers & designers B.V.

Financial support by the Dutch Heart Foundation for the publication of this thesis is gratefully acknowledged.

This research forms part of the Project P1.04 SMARTCARE of the research program of the BioMedical Materials institute, co-funded by the Dutch Ministry of Economic Affairs. The research described in this thesis was supported by a grant of the Dutch Heart Foundation (DHF-2008T092)

Computational analysis of cell orientation in response to mechanical stimuli; implications for myocardial repair strategies

PROEFSCHRIFT

ter verkrijging van de graad van doctor aan de Technische Universiteit
Eindhoven, op gezag van de rector magnificus prof.dr.ir. C.J. van Duijn,
voor een commissie aangewezen door het College voor Promoties, in het
openbaar te verdedigen op donderdag 30 oktober 2014 om 16.00 uur

door

Christine Obbink-Huizer

geboren te Veldhoven

Dit proefschrift is goedgekeurd door de promotoren en de samenstelling van de promotiecommissie is als volgt:

voorzitter: prof.dr.ir. F.N. van de Vosse
1^e promotor: prof.dr.ir. F.P.T. Baaijens
2^e promotor: prof.dr. C.V.C. Bouten
copromotor: dr.ir. C.W.J. Oomens
leden: prof.dr. P.A.F.M. Doevendans (UMCU)
prof.dr. V.S. Deshpande (University of Cambridge)
dr. C.C. van Donkelaar

Contents

Summary	v
1 General introduction	1
1.1 The heart	2
1.2 Myocardial infarction (MI)	3
1.3 Cell based strategies after MI	4
1.4 Strategies combining cells with biomaterials after MI	4
1.5 The local cellular environment	6
1.6 Cellular mechanosensing and the cytoskeleton	6
1.7 Rationale and outline	7
2 Controlling the deformation of cells delivered to the heart for cardiac repair: a finite element study	9
2.1 Introduction	10
2.2 Method	11
Model	11
Contact and (an)isotropy variation	12
2.3 Results	13
Influence of microtissue stiffness on microtissue strain	13
Influence of contact definition and (an)isotropy	14
2.4 Discussion	14
3 Computational model predicts cell orientation in response to a range of mechanical stimuli	19
3.1 Introduction	20
3.2 Proposed model	23
Existing models	23
Currently proposed model	24
3.3 Model results	25
Anisotropic substrate stiffness	27
Cyclic strain and high stiffness environment	27

	Cyclic strain and low stiffness environment	28
3.4	Discussion	30
3.5	Conclusion	32
4	Computational and experimental investigation of local stress fiber orientation in uniaxially and biaxially constrained microtissues	33
4.1	Introduction	34
4.2	Experimental method	35
	Experimental model system	35
	Microtissue seeding	36
	Visualization	36
	Image analysis	37
4.3	Computational method	38
	Computational model	38
	Computational model data analysis	40
4.4	Results	42
	Experimental results	42
	Computational results	43
4.5	Discussion	44
	Main findings and implications	44
	Comparison with literature	47
	Experimental limitations	48
	Computational limitations	48
	Conclusion	49
	Supplementary information: Image processing algorithm	50
5	Collagen and fibroblast orientation in the infarcted heart: cause and consequence	53
5.1	Introduction	54
5.2	Method	56
	Model of infarcted left ventricle	56
	Cell orientation model	60
	Variations	62
5.3	Results	63
	Strain comparison	63
	Predicted stress fiber distribution	64
	Stress in LV and cell orientation models	65
	Transmural variation	65
	Points around center node	65
	Excluding strain rate dependence on stress fiber orientation	66
	Increased passive stiffness and active cross-fiber contraction	66
5.4	Discussion	67
	Comparison to literature	70
	Proposed mechanism	71
	Implications	72
5.5	Conclusion	73

Appendix	73
6 General discussion	75
6.1 Introduction	76
6.2 Main findings	76
Limited control over microtissue mechanical environment via stiffness . . .	76
Model describing cellular mechanosensing and response via stress fibers .	77
Model quantitatively describes cell orientation in small tissues	77
Collagen in infarct does not co-align with cells that orient in response to mechanics	78
6.3 Models	78
Interaction between microtissue and environment	78
Stress fiber-based cell orientation model	79
Left ventricle model combined with cell orientation model	80
Comparison to models in literature	81
6.4 Implications and future research	83
Modeling how cells sense and respond to their environment	83
Microtissue-based cardiac regeneration	84
6.5 Conclusion	85
Bibliography	87
Samenvatting	103
Dankwoord	107
Curriculum Vitae	109
List of Publications	111

Summary

COMPUTATIONAL ANALYSIS OF CELL ORIENTATION IN RESPONSE TO MECHANICAL STIMULI; IMPLICATIONS FOR MYOCARDIAL REPAIR STRATEGIES

Myocardial infarction is one of the most common causes of death in the developed world. The oxygen supply to part of the heart is interrupted, causing local but massive death of cardiomyocytes. Because the natural regenerative capacity of the human heart is limited, a noncontractile scar tissue is formed after a myocardial infarction. This reduces heart function and, on the long term, may lead to detrimental remodeling and eventually heart failure. In an effort to enhance regeneration, stem cell therapy has been investigated to treat patients suffering from a myocardial infarction, albeit with limited success. Only a small fraction of delivered cells are retained in the myocardium and robust differentiation into cardiomyocytes has not been observed. It is hypothesized that embedding stem cells in a biomaterial to form small tissue-like constructs that can be injected into the myocardium (microtissues) will improve cell retention. The biomaterial allows enhanced control over the local cellular environment, which in view of the mechanosensitivity of the cells is expected to lead to increased control over cellular behavior. Next to a variety of biological requirements, functional integration of these cells with the myocardium also requires proper alignment of the cells. The goal of the present thesis was to develop a theoretical framework and computational model to analyze and predict cellular orientation in response to mechanical cues in the light of cardiac regeneration using microtissues.

As a first step towards this goal, it was investigated to what extent the local cellular mechanical environment in a microtissue can be controlled (Chapter 2). The local mechanical environment of the cell is determined in part by the mechanical properties of the microtissue (e.g. microtissue stiffness) which can be sensed by the cells, and also by the macroscale mechanical environment including the cyclic deformation of the heart, which will lead to deformation of a microtissue embedded in the heart. The influence of microtissue stiffness on microtissue strain was assessed using a computational model representing a spherical microtissue embedded in a deforming environment. When the stiffness of the microtissue was reduced, the strain in the

microtissue increased, showing that some control over microtissue deformation is possible via microtissue stiffness. However, the maximal average strain obtained in the microtissue was only $2^{1/2}$ times the deformation applied to the environment, while the stiffness of the microtissue was reduced with a factor of one hundred compared to the environmental stiffness. Thus, control over the strain in the microtissue via stiffness changes is only possible within a limited range. Furthermore, strain varied with the location within the microtissue. This effect was strongly influenced by on the contact definition between microtissue and environment and was smallest when microtissue and environment were fixed to each other. This heterogeneity further limits the range within which microtissue strain can be controlled. The results described in this chapter can be used to estimate which levels of strain are reasonable for application during in vitro experiments. Furthermore, the results indicate it is beneficial to fix microtissues to their environment when attempting to control the strain in a microtissue.

In Chapter 3, focus was shifted to the cell scale and cellular orientation. Many adhering cells have internal fibers, mainly directed along the longest axis of the cell. Cells can apply stress to their environment via these stress fibers, that have a molecular motor unit similar to muscle fibers. A computational model was developed to describe the synthesis and degradation of stress fibers. In the model, stress fibers could develop in a number of equally spaced directions. The stress in stress fibers in each direction was based on Hill's model. Stress was maximal if strain and shortening rate were zero, and reduced with absolute strain and with shortening rate. High stress in stress fibers in a direction led to an increased stress fiber production in this direction. With this model, stress fibers preferably developed perpendicular to directions undergoing cyclic strain, in the stiffest direction on an anisotropic surface, and in constrained direction when other directions were free, even when this constrained direction was cyclically strained. All these phenomena correspond to observations in in vitro model systems. These results show that the developed model is promising as a tool to analyze and predict cellular orientation in response to mechanical cues.

As a next step (Chapter 4), the model was applied to 3D small scale tissues. These tissues were constrained either uniaxially or biaxially so cells inside both types of tissues would sense a different mechanical environment. Furthermore, because of the specific method used to constrain the tissues, the local mechanical environment within each tissue was expected to be heterogeneous. Therefore, the model could be rigorously validated by simulating these experiments and quantitatively comparing simulated to experimental stress fiber orientations in every region of the tissues. In both experiment and simulation stress fibers mainly developed in directions with a high resistance to deformation. In the center of biaxially constrained tissues, resistance was high in all directions and a random orientation was observed. On the other hand, for uniaxially constrained tissues and near the tissue edges, resistance to deformation perpendicular to the free edge or constraint was reduced. This led to a preferred alignment in constrained direction and parallel to the edge. In general, a good quantitative agreement between experimental and simulated stress fiber distributions was obtained.

In Chapter 5 the developed computational model was applied to the heart. In tissues like myocardium, cells and collagen fibers are commonly aligned in the same direction. By comparing the cell orientation predicted by the model to an experimentally observed collagen orientation, it is possible to study whether this co-alignment is

driven by the cells. A stress fiber orientation was predicted based on the local deformation in an infarcted heart, estimated with an existing model of the left ventricle. This was compared to experimentally observed collagen orientations described in literature for infarcts at different locations (apex and mid-ventricle) and of different shapes. For the apical infarct the predicted stress fiber orientation was random. This corresponded to the experimentally observed collagen orientation. However, for mid-ventricular infarcts with different shapes the model predicted a preference for the longitudinal direction, while a circumferential collagen orientation was observed experimentally. This indicates that, assuming cellular deformation is similar to the macroscale deformation of the infarcted tissue, the collagen orientation observed experimentally is not due to collagen co-aligning with a mechanics-based cell orientation. These results show that the developed cell model cannot directly be applied to the infarcted heart in its current state and points towards the local structure (e.g. the local collagen orientation) as important aspect of the cellular environment. Including the local structure and contact guidance into the model is an interesting direction for future research.

Altogether this thesis shows that computational modeling can provide a significant contribution to the understanding and prediction of cellular orientation behavior, which is important for myocardial repair strategies such as the injection of microtissues.

Chapter 1

General introduction

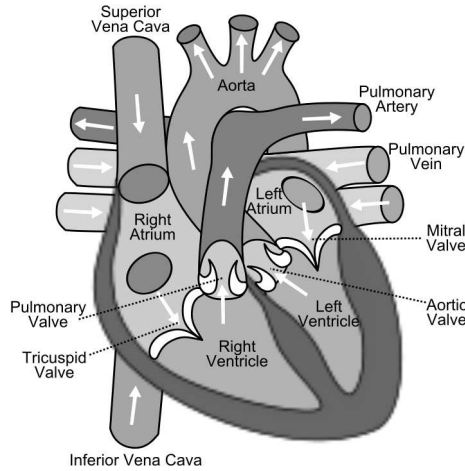


Fig. 1.1: The heart (modified from^[1])

1.1 THE HEART

The heart (Fig. 1.1) is one of the vital organs of the human body. It pumps blood around the body, to allow oxygen and nutrient delivery as well as waste removal, by cyclically contracting. The contraction phase of the cardiac cycle is called systole, while the relaxation phase is termed diastole. The heart is divided in a left part, pumping oxygen-rich blood throughout the body, and a right part, which pumps oxygen-poor blood to the lungs. Each part consists of an atrium that is located above a ventricle. The atria receive blood from the circulation and pump it to the ventricles. This requires minimal contraction and, as a rule, the atria contribute little to the propulsive pumping activity of the heart. The ventricles discharge blood from the heart into the circulation. Valves between atria and ventricles and between ventricles and connecting large arteries ensure blood flows in only one direction. Ventricular function requires more contractile force than atrial function, which is reflected in the more massive wall size of the ventricles compared to the atria. Also, left ventricular wall mass is larger than right ventricular wall mass as the left ventricle pumps against the large resistance of the entire circulatory system. The heart wall consists of three layers: the endocardium on the inside of the heart, the epicardium on the outside of the heart, and the myocardium in between.^[88] The myocardium consists of heart muscle cells or cardiomyocytes, non-muscle cells, and connective tissue called the extracellular matrix (ECM)^[89]. Cardiomyocytes take up the bulk myocardial volume (~75%^[95]), and provide the force that contracts the heart to propel blood^[110]. The cardiac fibroblast, a type of non-muscle cell, is the most numerous cell type and produces, regulates and remodels the ECM^[110]. An important component of the ECM is collagen, as it is the major stress-bearing protein^[110]. The building blocks of cardiac tissue are assembled into a specific three-dimensional structure, which includes a layer-wise alignment of cardiac myocytes^[23]. This (fiber) structure is essential for proper pumping of the heart

and is hypothesized to be mechanically optimal^[122], minimizing the energy required to pump blood.

1.2 MYOCARDIAL INFARCTION

The heart supplies itself with blood via coronary arteries^[88]. The oxygen supply to a part of the myocardium may be interrupted, for example due to a blood clot (thrombus) blocking a coronary artery that already has a reduced diameter due to atherosclerosis^[141]. Unless this situation is resolved within 30 minutes^[13], the restricted blood supply (ischemia) causes local cardiomyocyte cell death^[136]. The left ventricle (LV) is most susceptible to irreversible ischemic damage^[49] and LV myocardial infarction (MI) receives most attention. In the acute phase after MI, patient death may occur due to electrical dysfunction such as ventricular fibrillation (often before a hospital is reached^[147,164]), cardiogenic shock (the most common cause of death in patients hospitalized with acute MI^[138,151]) or structural disorders including free wall rupture (most common death cause after cardiogenic shock^[151])^[11]. Fortunately, acute MI-related mortality is reduced over the last decades^[11,139] due to drugs to reduce thrombus formation and abnormal heart rhythms^[10], as well as catheter-based reperfusion^[139] and stenting^[11]. Because of this, an increased number of patients have healing or healed infarcts^[10,59]. As the natural capacity to regenerate human heart muscle tissue is limited, non-contracting scar tissue is formed after an MI^[73].

The healing process in an infarcted heart shares many characteristics with healing in e.g. skin and follows several phases. The first 12–16 hours after MI correspond to the cardiomyocyte death phase. This is followed by a second, inflammatory, phase, lasting until two or three days after infarction. Degradation of ECM components starts during these initial phases. During a third phase, granulation tissue is formed containing new ECM proteins including collagen produced by myofibroblasts. During the final phase of infarct healing, myofibroblasts in the infarct undergo apoptosis, though some myofibroblasts remain present in the scar^[10]. Cross-linking of the deposited collagen becomes important^[10,59]. Infarct scar tissue often continues to dynamically remodel, without reaching a stable final configuration^[59,133]. LV function may improve during the process of infarct healing^[59]. However, eventually detrimental remodeling of the infarcted heart occurs^[43,65,68] in approximately 20% of the patients^[46,63], especially in those with large MI's^[43,109]. In the case of detrimental remodeling, cardiomyocyte loss leads to progressive left ventricular dilation^[25], possibly because infarct expansion leads to ventricular dilation^[25] and causes increased wall stress, resulting in more ventricular dilation^[109] of the non-infarcted tissue^[25] in a vicious cycle^[65,109]. Though initially patients may be asymptomatic due to compensatory mechanisms, on the long term symptoms of heart failure may occur, with a striking increase in patient mortality^[87,113]. It is thus important to develop new therapies that prevent the development of heart failure, especially after large or recurrent MI's^[43]. In these therapies, left ventricular maladaptive remodeling is a target for treatment^[94].

1.3 CELL BASED STRATEGIES TO PREVENT HEART FAILURE AFTER MI

Most therapies for MI, such as drug therapies and circulatory assist devices, can improve life expectancy^[148] and may attenuate adverse remodeling^[94], but cardiac function is not restored^[148]. An interesting treatment approach to myocardial infarction is cell therapy, involving the transplantation of cells to the infarcted region^[148]. This technique aims at restoration of cardiac function^[148], thus breaking the vicious cycle leading to heart failure. Different cell types (e.g. bone marrow derived cells, skeletal myoblasts, mesenchymal stem cells and cardio-derived progenitor/stem cells) as well as delivery methods (intravenously, intracoronary, or direct injection into the myocardium^[25]) have been investigated for cardiac cell therapy^[134]. However, the optimal cell type and delivery route, as well as cell quantity and timing of delivery are still uncertain^[123]. Though cell therapy was shown to be beneficial in some animal studies, in clinical trials only modest or negligible improvement of heart function is demonstrated^[43]. The number of differentiated transplanted cells in most experimental studies is too small to account for the observed cardiac function improvements. This indicates the mechanism leading to functional improvement may not be directly related to cardiac regeneration by transplanted cells, but to paracrine effects^[86], and the mechanisms by which various cell therapy approaches influence cardiac function require further research^[80]. A main limitation of current cardiac cell therapy approaches is a low cell retention and survival after delivery^[21,86]. Retention is generally below 10% and approximately 90% of the cells that are retained die within the first week^[86]. Increasing cell retention and survival is expected to improve the long-term efficacy of cell therapy, and several strategies to achieve this have been proposed, including physical approaches to retain cells, often using biomaterials^[86].

1.4 STRATEGIES COMBINING CELLS WITH BIOMATERIALS TO PREVENT HEART FAILURE AFTER MI

One possible use of biomaterials is to create cardiac patches^[112], for example by seeding cells on a pre-formed scaffold^[25,112]. An improvement of cardiac function with this technique is shown in small animals^[112]. However, major drawbacks of this method^[113] are the inability to create thick patches due to diffusion limitations^[112], limitation of the delivery region to the epicardial surface, and the invasive procedure that is required to deliver cardiac patches^[112]. The last two drawbacks are avoided if an injectable material is used. Cells embedded in such a material can then be directly injected into the heart^[65,112], using an in situ tissue engineering approach^[25]. Injection of a biomaterial along with cells can improve cell retention and viability^[112]. Also, the biomaterial itself may help preserve cardiac function after a myocardial infarction^[112], by supporting passive cardiac function^[45] and attenuating LV remodeling^[146]. Therefore, approaches incorporating only a biomaterial and no cells have been proposed^[65]. However, the active mechanical function of the heart can only be restored if the number of contractile cells in the infarcted heart is increased, either via exogenous or via endogenous cells^[45]. Exogenous cells must be delivered to the heart. If a non-contractile cell type, such as stem cells, is used, the cells must also be stimulated to differentiate into cardiomyocytes. Endogenous cells must be stim-

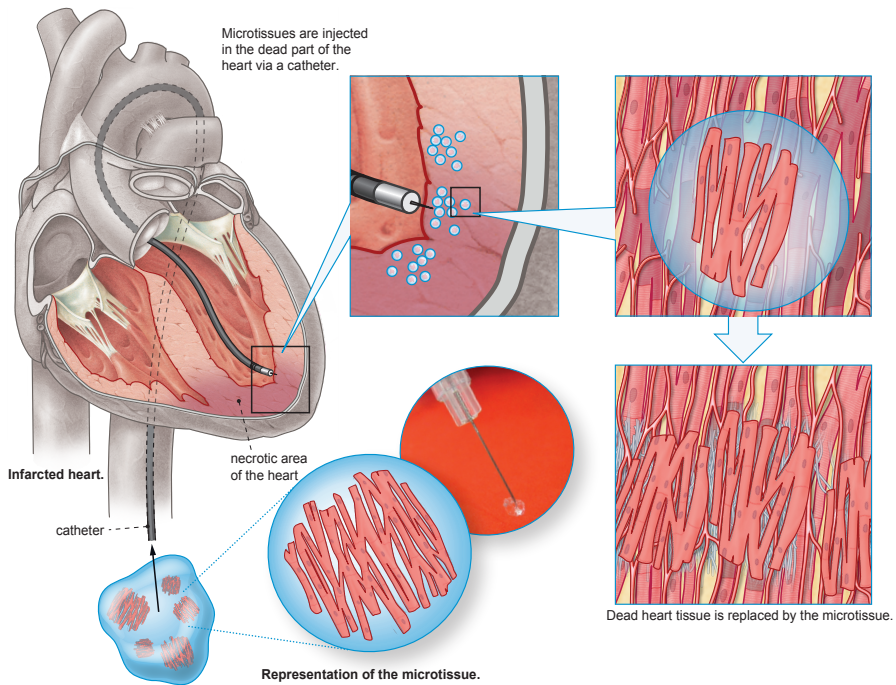


Fig. 1.2: The SMARTCARE project. Cells are surrounded by a biomaterial to form miniature tissues that engraft into the myocardium. Biochemical factors may be incorporated to stimulate beneficial cellular behavior. Biomaterial properties may be tuned to provide optimal mechanical support to both cells and the macroscopic cardiac environment. The small size allow non-invasive delivery to the infarcted myocardium via a catheter. ©BMM/Rogier Trompert Medical Art, adapted

ulated to migrate, proliferate and differentiate. Attracting cells may be possible by delivering a biomaterial scaffold to the infarcted heart that stimulates cellular infiltration^[65], possibly by incorporating biochemical agents such as growth factors that are released in a temporally controlled manner^[113]. Combining these effects, an optimal approach to cardiac regeneration could involve cells embedded in small ($\sim 100 \mu\text{m}$) tissue-like biomaterial constructs (microtissues) also including biochemical factors. Cells may provide active contraction and beneficial paracrine effects. The biomaterial and biochemical factors may increase cell retention and may possibly attract endogenous cells besides providing a suitable local cellular environment for cell survival, differentiation and engraftment. The mechanical properties of the biomaterial may improve passive cardiac mechanics and limit negative remodeling, and the microtissue form allows non-invasive delivery via a catheter. Such a combinatory approach is investigated in the BMM (BioMedical Material) program SMARTCARE (SMART microtissues for CARDiac Regeneration), of which the work presented in this thesis forms a part (Fig. 1.2).

1.5 THE LOCAL CELLULAR ENVIRONMENT

One of the main advantages of incorporating cells in microtissues compared to directly injecting them, is that microtissues allow increased control over the local environment experienced by the cells. This is advantageous because cells are known to react in response to their environment — cells can respond to chemical and physical stimuli by e.g. migrating^[82], differentiating^[30] or even undergoing apoptosis^[35,74]. Control of the cellular environment may thus allow control of cellular behavior. With standard cell therapy, cells are in direct contact with the myocardium, which is pre-defined, so control over the local cellular environment is limited. If the cells are part of a microtissue, they interact with their local environment within the microtissue, while the microtissue interacts with the myocardium on a larger scale. The local cellular environment can thus be influenced via microtissue properties, but the properties of the myocardium will also play a role (Fig. 1.2). This holds for both biochemical and mechanical aspects of the micro-environment. The chemical micro-environment experienced by cells in a microtissue may be influenced by incorporating biochemical agents in the microtissue. This is not discussed in detail here, as the focus of this thesis is on mechanical rather than chemical aspects of the cellular environment. The mechanical micro-environment may be influenced via the mechanical properties of the biomaterial incorporated in the microtissue. In this case, besides microtissue mechanical properties, cardiac deformation will play a role in determining the micromechanical environment inside a microtissue. To understand the behavior of cells delivered to the heart in microtissues, it is thus essential to understand the mechanical interaction between the infarcted myocardium on the macro scale, the microtissue on the meso scale and the cells on the micro scale. Furthermore, it is necessary to understand how cells respond to mechanical stimuli.

1.6 CELLULAR MECHANOSENSING AND THE CYTOSKELETON

The local cellular mechanical environment includes active inputs, such as an applied stress or strain, and passive inputs, such as stiffness^[115]. Both types of input can influence cellular behavior. Examples of responses to passive inputs include reduced cell spreading on soft substrates^[106], and preferred migration^[48,84,119] and orientation^[48,119] in stiffest direction on anisotropic substrates. These are active, biological responses. In response to active inputs, cells can behave passively, by deforming. When the material properties of a cell or tissue are determined, it is commonly assumed that the cellular response to deformation measured is strictly passive^[115]. However, cells may also respond in an active, biological manner to active stimuli^[115]. Examples of such an active response include cellular reorientation to a position perpendicular to cyclic strain^[26,50] and reduced endothelial cell proliferation in response to laminar shear stress^[3]. A cellular response is only possible if the input is sensed. Active inputs can be sensed passively by the cell, because they change the force and/or deformation of the cell, but passive inputs cannot be sensed without cellular activity.

The cellular cytoskeleton plays an important role in determining passive cellular properties, sensing passive and active mechanical inputs and responding to these inputs^[92,124]. The cytoskeleton has three main components: actin filaments, interme-

diate filaments and microtubuli^[22], and also includes their cross-linking proteins^[93]. For cells in solution, only the microtubuli network is well developed^[124], which plays a role in withstanding compressive forces^[22]. Intermediate filaments mainly resist large cellular tensile deformation^[22]. In adhering cells, bundles and networks of actin fibers are commonly under tension, because they are contracted by molecular motor proteins, mainly myosin II^[124]. This causes sliding of actin filaments with respect to each other, unless the actin filament is anchored to an environment that resists this, leading to the build-up of force^[124]. Actin filaments can form different structures, including lamellipodia, protrusions important for cell migration; cortical cell membrane-bound networks regulating cell shape; and stress fibers, contractile actin bundles^[132]. Stress fibers are periodically cross-linked by α -actinin that alternates with myosin II, giving them an appearance that is similar to sarcomeres^[20], the basic contractile units of muscle fibers. Stress fibers mainly form between points where actin contraction via myosin is resisted^[93]. These points are often focal adhesions, transmembrane protein complexes that are anchored to the extracellular matrix^[93]. On 2D anisotropic substrates, stress fibers mainly develop in the stiffest direction^[48,119] and, when cells are embedded in a gel that is constrained in one direction but not in the others, stress fibers mainly develop in constrained direction^[24,102]. Actin stress fibers commonly respond to cyclic strain by orienting away from it, both on 2D substrates^[54,69,70,100,158] and in 3D gel environments^[42,50]. The avoidance of a cyclically strained direction can be dominated by the preference of a constrained direction, if both stimuli are present^[47,102]. The presence and orientation of stress fibers thus depends on the mechanical environment^[20]. Stress fibers influence cellular mechanical properties^[60]. They are thought to be the main generators of force on the cytoskeleton^[124] and are thus required for active mechanosensing. Therefore, the complex interplay between the local mechanical environment and the presence and structure of the stress fiber network inside a cell is important to understand how cells influence their environment and vice versa.

1.7 RATIONALE AND OUTLINE

The interaction between cells and their mechanical environment is extremely complicated and virtually impossible to understand without computer models. In this thesis, I aim to improve understanding of the interaction of cells embedded in microtissues in the heart with their environment via theoretical modeling. Attention is concentrated on how cells respond to their mechanical environment, focusing on their orientation, and on the local mechanical environment experienced by cells in the heart and how this environment is influenced by embedding the cells in a microtissue. First of all, the amount of control over the local mechanical environment in a small tissue injected into the heart was investigated (Chapter 2). The results indicated some control over the strain in an injected tissue is possible by varying its stiffness. However, strain inhomogeneity may be an issue, especially if the injected tissue is not adhered to the myocardial tissue. After this, the focus was shifted to modeling the interaction between the cytoskeleton and the cellular mechanical environment (Chapter 3). Inspired by models by Deshpande et al.^[29] and Vernerey and Farsad^[142], a computational model was developed to describe how stress fibers develop in response to the mechanical

environment that they actively sense. In the model, stress fibers can align in response to both a passive substrate anisotropy stimulus and an active cyclic strain stimulus. The model qualitatively describes stress fiber orientation in response to a range of mechanical stimuli reported in literature for various cell types. The model was then applied to an in vitro model system, in which the local mechanical environment is heterogeneous (Chapter 4). This showed quantitative agreement between simulated and experimental results, increasing confidence in model predictions. Therefore, the model was applied to the stress fiber orientation of cells in the infarcted heart (Chapter 5), by combining it with results from a previously developed ventricular model^[17]. Calculated stress fiber orientations in the infarcted zone were compared to experimentally observed collagen orientations, as cells and collagen commonly co-align. The orientation predicted by the model was opposite to the experimentally observed orientation, implying that instead of collagen orientation in the infarcted heart being determined by the cells, cell orientation may be determined by the collagen organization present. Finally, this thesis ends with a general discussion in which the main findings and the developed models are discussed, and recommendations for further research are given (Chapter 6).

Chapter 2

**Controlling the deformation of cells
delivered to the heart for cardiac
repair: a finite element study**

ABSTRACT

Stem cell therapy after myocardial infarction may be improved by combining cells with a biomaterial. One such approach is to embed the cells in small, tissue-like constructs to form microtissues. After delivery, these microtissues will mechanically interact with the myocardium surrounding them. In this study, reasonable levels of microtissue deformation, a possible mechanical stimulus for cells in the microtissue, are estimated using finite element analysis. Our axisymmetric model represents a spherical microtissue embedded in a cylindrical environment, simulating the myocardium. A uniaxial elongation is prescribed to represent macroscale deformation, and microtissue stiffness is varied to simulate the controllability of microtissue mechanical properties. Local strain in the microtissue was between zero and four times the applied strain, indicating that this is a reasonable range of strains to be applied to cells experimentally. Strain heterogeneity depended on the microtissue-environment contact definition, showing the importance of adhesion of the microtissue to the environment.

2.1 INTRODUCTION

In patients with myocardial infarction, contractile cells in part of the myocardium die due to local ischemia^[136]. Following this injury, the tissue loses its ability to contract and undergoes remodeling, often leading to fatal dilatation of the heart^[59,109]. Cell therapy has been proposed to improve myocardial functioning, attenuate adverse remodeling, and avoid heart failure. However, functional improvement, commonly measured as an increase in ejection fraction, is moderate and inconsistent^[83,91,152]. Only a fraction of the cells is retained^[117,135], and whether significant cardiac regeneration by differentiation occurs is arguable^[114]. Strategies to improve cell retention and differentiation are therefore expected to increase cardiac regeneration and functional improvement. One such strategy is to combine the cells with a biomaterial. The cells can then adhere to the biomaterial as they adhere to the extracellular matrix. This improves cell survival and engraftment^[165]. The biomaterial may in itself improve cardiac function when placed in the heart by providing mechanical support and inhibiting dilation^[64]. Since contractile function cannot be restored without active cells^[45], an approach combining material and cells seems most favorable. Cells and material may be engineered into a tissue in vitro. This allows stimuli to be applied to the cells, aiming to direct them towards differentiation and to create myocardium-like tissue patches^[165]. However, such cardiac patches are commonly so large that their delivery requires invasive open chest surgery^[126]. A tissue-like structure may also be formed in vivo, when cells are delivered in a fluid that gels in the heart after delivery^[126]. With this approach, catheter delivery is possible. However, in vitro tissue formation is impossible, and control over what is experienced by cells in a time- and space-dependent manner is limited. Therefore, we propose the use of small, injectable tissues (microtissues), allowing non-invasive delivery, the possibility of in vitro tissue engineering, and a well-defined local environment for the cells.

In the ideal situation, microtissues are delivered without in vitro stimulation because this requires the least time and effort. The cells embedded in the microtissues should then be guided towards differentiation and cardiac tissue formation by the stimuli received in vivo. If the required stimuli cannot be given in vivo, microtissues need to be engineered in vitro, and the stimuli received in the heart should not undo in vitro

tissue engineering. In both cases, it is important to know which stimuli the cells receive and how they respond to them. So far, environmental control of stem cells has mainly focused on biochemical regulation. There is, however, growing evidence that mechanical signals may also regulate stem cell fate^[34]. For the heart, it is hypothesized that cyclic deformation is of special importance because of its occurrence in vivo and because cells, including cardiomyocytes, respond to it in vitro^[2,8,37]. Thus controlling microtissue deformation is expected to improve control over cell behavior and allow increased cell differentiation and hence cardiac repair.

In a microtissue, the mechanical properties of the biomaterial can be selected, but the properties and deformation of the macro-environment (the heart) cannot. Since the microtissue is mechanically coupled to the macro-environment, not all mechanical stimuli will be possible in the microtissue. In particular, microtissue deformation will be influenced by both the uncontrollable macro-environment and the controllable local mechanical properties. To understand and predict the relationship between the macromechanical environment (the heart) and the micromechanical environment (the microtissue), this study investigates the possible range of mechanical states in a microtissue. This can then be used to guide experimental studies regarding the relationship between mechanical stimuli and cellular behavior. Therefore, the aim of this study is to determine within which range the deformation of a microtissue in a deforming environment can be controlled by varying microtissue stiffness. Several options for the contact definition between microtissue and macro-environment and the amount of anisotropy of the macro-environment are tested since these factors may vary.

2.2 METHOD

Model

A computational model representing a microtissue in a simulated cardiac environment was developed in Abaqus 6.9-2 (Simulia, Providence, USA). This axisymmetric model consists of a sphere with a radius of 50 μm , representing the microtissue, embedded in a cylindrical environment with a radius of 100 μm and length of 200 μm , representing the myocardium. Due to symmetry considerations, only a quarter of the cross-section was modeled and movement at both the axisymmetry axis and the reflection symmetry axis was restricted perpendicular to the respective axes (Fig. 2.1). A macroscopic deformation corresponding to a longitudinal strain of 0.1 was applied. Though this is a simplification of the actual deformation of the heart, it is expected to give a reasonable first impression of the interaction between macro- and microtissue when microtissue deformation is taken relative to macroscopic deformation, as was done here. The microtissue was modeled as an incompressible hyperelastic neo-Hookean material with the Abaqus/standard material library. Microtissue stiffness was varied between 0.3 and 50 kPa. In this sensitivity study, the maximal principal nominal strain (MPNS) was used as a measure of deformation in the microtissue. Specifically the mean MPNS in the microtissue, the range of the MPNS in the microtissue, and the distribution of the MPNS in the microtissue were investigated. Nominal strain was defined as $(\mathbf{F}\mathbf{F}^T)^{1/2} - \mathbf{I}$, with \mathbf{F} the deformation tensor. To calculate the mean MPNS, the MPNS at the integration points in the microtissue was used, and the integration point volume was applied to calculate a weighted mean.

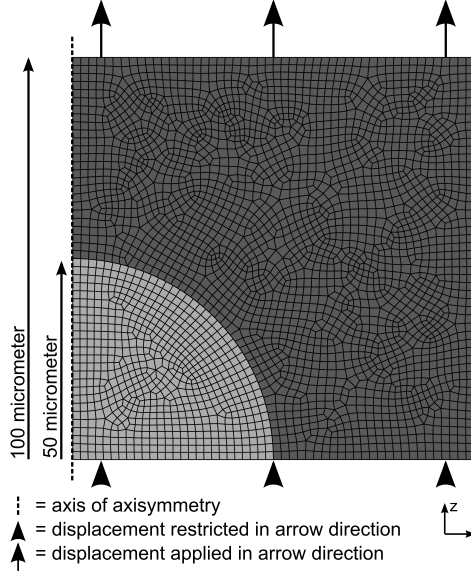


Fig. 2.1: The model consisting of a microtissue (light) surrounded by an environment (dark). Coordinate system, axisymmetry axis, boundary conditions, mesh and size are also shown.

Contact and (an)isotropy variation

Several versions of this model were made, varying in contact definition and (an)isotropy, while the range of microtissue stiffness was maintained for each configuration. The relative motion of microtissue and environment depends on their adherence and friction. Two extreme cases were investigated: infinite friction or affine contact (AFF; adhesion in normal and shear direction) and frictionless shear (FLS; adhesion only in normal direction). This was done by defining default cohesive behavior for the AFF contact and a hard contact in the normal direction without allowing separation after contact for the FLS case. To investigate the influence of microtissue stiffness, irrespective of anisotropy likely for healthy^[97] and infarcted^[59] myocardium, simulations were run for both an isotropic (ISO) and a severely anisotropic (AN) environment as extreme cases. The environment was modeled as a neo-Hookean matrix with linear elastic fibers, comparable to Korhonen et al.^[75], using the user subroutine UMAT. With a rule of mixtures, the non-fibrillar matrix stress (σ_{nf}) and the fiber stress with respect to the global coordinate system (σ_f), are combined into the total stress (σ_{tot}):

$$\sigma_{tot} = (1 - \rho)\sigma_{nf} + \rho\sigma_f \quad (2.1)$$

with ρ the fiber volume fraction^[161]. The non-fibrillar matrix stress is defined as^[75]

$$\sigma_{nf} = K \frac{\ln(J)}{J} \mathbf{I} + \frac{G}{J} (\mathbf{F}\mathbf{F}^T - J^{2/3} \mathbf{I}) \quad (2.2)$$

where \mathbf{F} is the deformation tensor and $J = \det(\mathbf{F})$. The bulk (K) and shear (G) moduli are expressed as $K = \frac{E_m}{3(1-2\nu_m)}$ and $G = \frac{E_m}{2(1+\nu_m)}$, where E_m and ν_m are the Young's

Table 2.1: Model versions and abbreviations used for them.

	Isotropy		Anisotropy	
			Straight fibers	Curved fibers
Affine	AFF-ISO		AFF-AN-S	AFF-AN-C
Frictionless shear	FLS-ISO		FLS-AN-S	FLS-AN-C

modulus and the Poisson's ratio of the non-fibrillar matrix, respectively. The fiber stress is given by

$$\boldsymbol{\sigma}_f = \sigma_f \vec{e}_f \vec{e}_f \quad (2.3)$$

with σ_f the Cauchy stress in fiber direction and \vec{e}_f the current fiber direction, computed as $\vec{e}_f = \frac{\mathbf{F} \cdot \vec{e}_{f,0}}{\|\mathbf{F} \cdot \vec{e}_{f,0}\|}$ with $\vec{e}_{f,0}$ the initial fibril direction^[159]. A linear elastic model is used for σ_f according to^[75]

$$\sigma_f = \begin{cases} E_f \varepsilon_f & \text{if } \varepsilon_f \leq 0 \\ 0 & \text{if } \varepsilon_f > 0 \end{cases} \quad (2.4)$$

where E_f is the fiber stiffness and the fiber engineering strain is chosen as ε_f . For the isotropic model, ρ is zero, so $\boldsymbol{\sigma}_{tot}$ equals $\boldsymbol{\sigma}_{nf}$ (equation 2.1), resulting in a neo-Hookean material. E_m is 50 kPa, comparable to scar tissue^[7,61], and ν_m approaches 0.5. For the anisotropic model, the fiber volume fraction is 90% ($\rho = 0.9$), so $\boldsymbol{\sigma}_{tot} = 0.1\boldsymbol{\sigma}_{nf} + 0.9\boldsymbol{\sigma}_f$. The basic fiber direction is axial. To avoid differences between the isotropic and anisotropic models due to stiffness differences, the stiffness in fiber direction — corresponding to the loading direction — is taken to be comparable to the isotropic stiffness. To achieve this, both E_m and E_f were 50 kPa. In this case, increasing fiber volume fraction leads to a comparable stiffness in fiber direction since E_m and E_f are similar, but reduced stiffness in other directions since $\boldsymbol{\sigma}_f$ is only determined by stress in fiber direction and not by stress in other directions (equation 2.3). Around an inclusion such as a microtissue, fibers may curve instead of abruptly stopping. Therefore, two options for the fiber direction were tested: straight (S) or curved around the microtissue (C) (Fig. 2.2). This leads to a total of 6 model versions (Table 2.1).

2.3 RESULTS

Influence of microtissue stiffness on microtissue strain

For each model version, an example of the strain distribution in the model is shown in Fig. 2.3. In the microtissue, the mean strain, range of strain, and location of minima and maxima vary between model versions. Varying stiffness within a model version leads to differences in the average strain and the range of strain but a similar strain distribution. Therefore, in Fig. 2.4 strain and range of strain versus stiffness are shown for each model version. As microtissue stiffness decreases, mean strain (solid line) and range of strain (filled area) increase for each version. Local strains were between 0 and 4 times environmental strain, while the average strain was between 0.5 and 2.5 times environmental strain.

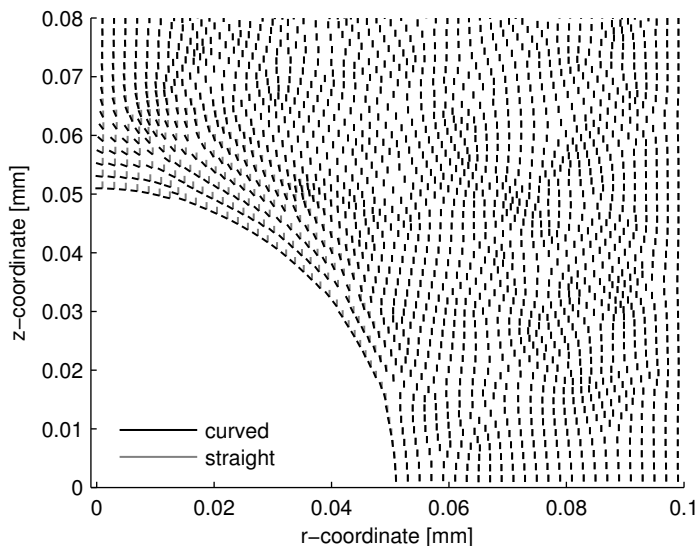


Fig. 2.2: Fiber direction in part of the model with curved fibers (dark lines). Fiber directions in model with straight fibers are also shown (lighter lines) when not coinciding. Curved fibers are parallel to the spherical inclusion along the curved edge, vertical away from this edge and gradually change orientation in between. Straight fibers are vertical everywhere.

Influence of contact definition and (an)isotropy

The FLS-contact (right graph) led to larger strain ranges and slightly smaller mean strains than the AFF-contact (left graph). For the FLS-contact, mean and maximal strains showed comparable trends and minimal strains were close to zero independent of stiffness or (an)isotropy. Strain distributions were also similar, independent of (an)isotropy of the environment (Fig. 2.5 bottom row). For the AFF-contact, the strain distribution did vary with (an)isotropy (Fig. 2.5 top row). For both contact definitions, anisotropy of the macro-environment enhances the sensitivity of the microtissue deformation to the stiffness ratio: strain was larger for compliant microtissues and smaller for stiff microtissues (Fig. 2.4). Also, the curved fibers resulted in a smaller mean strain than the straight fibers and for the AFF-simulations, the strain heterogeneity was larger, especially for high microtissue stiffnesses.

2.4 DISCUSSION

In this study, we computationally investigated the level of control of the deformation of a microtissue embedded in a deforming macro-environment, such as the myocardium. Our model indicates that local microtissue strains range between zero and four times the environmental deformation. We also found that the deformation of the microtissue is heterogeneous: the local strain within the microtissue is location dependent, especially when the microtissue can slide with respect to the environment

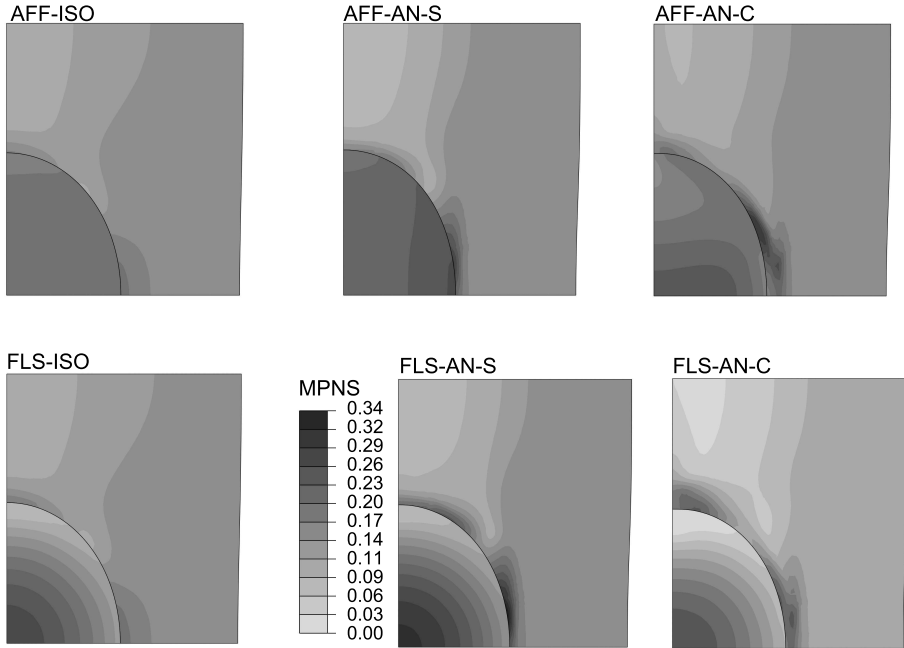


Fig. 2.3: Maximal principal nominal strain distribution for 5 kPa microtissue in all model version. The same scale is used for each model.

(FLS-contact). To our knowledge, the number of computational models of the cellular micromechanical environment presented in literature is limited. Yan et al.^[163] modelled the deformation and damage of cells in a gel during a compression test. Since no fixed macro-environment was under consideration, control of the local mechanical environment was not an issue. The consequences of interventions such as cellular transplantation in dilated cardiomyopathy^[111] and the injection of material into the myocardium after infarction^[145] have also been simulated. Various infarct mechanical properties have been investigated numerically as well^[39]. These studies focus on measurements of macroscale heart function, such as ejection fraction. The intervention is modeled as a regional change in mechanical properties, without separately modeling the infarcted tissue and any material added; therefore, a local mechanical environment cannot be determined from these studies. Our study, on the other hand, specifically addresses the interaction between macro scale and micro scale and shows the local mechanical environment that can be expected in a microtissue when placed into the heart.

Though our model is obviously a simplification of reality, we expect our main conclusions — a relevant strain range between zero and four times environmental strain and the possibility of strain heterogeneity occurring — to be valid. Since deformation relative to the environmental deformation is considered, our results are rather insensitive to variations in environmental deformation. As an example: changing the applied

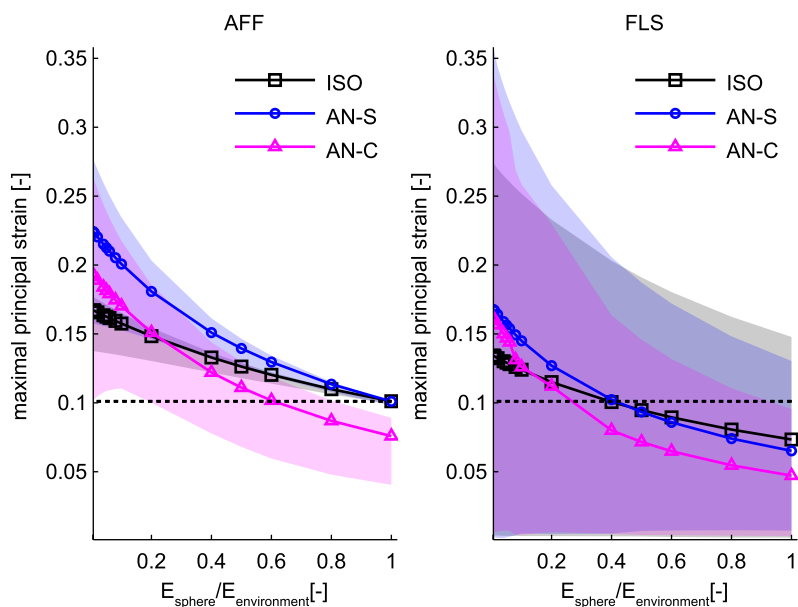


Fig. 2.4: Maximal principal strain for AFF (left) and FLS (right) models. Different lines denote mean in microtissue for different versions of the model. The surrounding filled area in corresponding color corresponds to the range of strain in the microtissue. The dotted line denotes a strain of 0.1, which is the applied strain.

deformation to 10% compression or 40% extension had little influence on the ratio between microtissue deformation and applied deformation (less than 5% difference, data not shown). Other model simplifications, such as the material properties used, or not taking into account any initial deformation that may occur due to delivery of the microtissues, may influence the precise strain occurring at a specific location in a microtissue with specific stiffness. However, the range of strains is not expected to be influenced much, because it is less sensitive to changes. Obviously, experimental input is required to validate the model and to establish data on cellular behavior in response to local mechanical properties.

Reducing stiffness beyond the minimal value investigated here (0.3 kPa, 0.6% of environmental stiffness) may further increase strain. However, the small stiffness required for a significant strain increase does not seem realistic. This is partly because minimal stiffness is limited by cell stiffness: if the stiffness of the cells is larger than the stiffness of the rest of the microtissue, cell stiffness will dominate the deformation. Because in reality the microtissue is not a continuum but consists of cells and surrounding material, the current results can only give an approximation of their combined strain, and not of local cellular strain. Determining strain on a cellular level is an interesting problem. However, the combined cell-local environment strain is currently more relevant, because strain will be applied on a construct level when in vitro experiments are performed to determine cellular response to a specific micromechanical

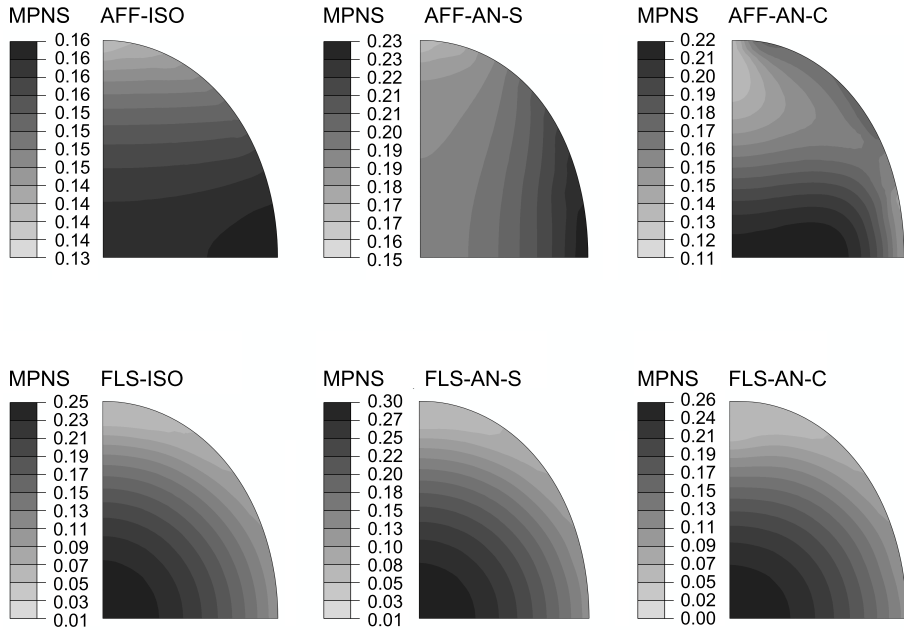


Fig. 2.5: Maximal principal nominal strain distribution in a microtissue with 5 kPa stiffness for each model version. Different scales are used for each model.

environment.

Based on our results, microtissue deformation *in vivo* is expected to be between zero and four times the (macroscopic) deformation of the heart. It is therefore interesting to determine the response of cells to strains in this range *in vitro*. The results can then be used to determine appropriate microtissue material parameters. Since stiffness and deformation are interdependent when environmental boundary conditions are fixed, as is the case in our model, microtissue stiffness was varied to obtain this range of deformations. During *in vitro* experiments, however, stiffness and deformation may be varied separately. Moreover, cells have been shown to respond to stiffness^[99] as well as strain. Therefore, an investigation of the response of cells not only to prescribed deformations, but also to different environmental stiffnesses under a prescribed deformation can be performed, to determine the relative and combined contributions of microtissue stiffness and microtissue deformation on cellular behavior. It should be noted that the frequency of the cyclic deformation in the heart is also a determinant of cellular responses and should be taken into account in these future studies.

The heterogeneity of the strain field within the microtissue may limit the control over the strain in the microtissue because the mechanical stimulus that cells in different parts of the microtissue experience can vary and so can their response. Since deformation was more homogeneous with affine contact than with frictionless shear, this contact is preferable. However, a frictionless shear contact may be more reason-

able for potential microtissue materials, such as hydrogels. In this case, control over the strain field within the microtissue is expected to be improved if a way is found to adhere the microtissue to its environment.

Chapter 3

Computational model predicts cell orientation in response to a range of mechanical stimuli

This chapter is based on:

C. Obbink-Huizer, C.W.J. Oomens, S. Loerakker, J. Foolen, C.V.C. Bouten, F.P.T. Baaijens (2014) *Computational model predicts cell orientation in response to a range of mechanical stimuli*. *Biomech Model Mechanobiol.* 13(1):227-236 doi: 10.1007/s10237-013-0501-4

ABSTRACT

To build anisotropic, mechanically functioning tissue, it is essential to understand how cells orient in response to mechanical stimuli. Therefore, a computational model was developed which predicts cell orientation, based on the actin stress fiber distribution inside the cell. In the model, the stress fiber distribution evolves dynamically according to: (1) Stress fibers contain polymerized actin. The total amount of depolymerized plus polymerized actin is constant. (2) Stress fibers apply tension to their environment. This active tension is maximal when strain rate and absolute strain are zero, and reduces with increasing shortening rate and absolute strain. (3) A high active fiber stress in a direction leads to a large amount of fibers in this direction. (4) The cell is attached to a substrate; all fiber stresses are homogenized into a total cell stress, which is in equilibrium with substrate stress. This model predicts that on a substrate of anisotropic stiffness, fibers align in the stiffest direction. Under cyclic strain when the cellular environment is so stiff that no compaction occurs (1 MPa), the model predicts strain avoidance, which is more pronounced with increasing strain frequency or amplitude. Under cyclic strain when the cellular environment is so soft that cells can compact it (10 kPa), the model predicts a preference for the cyclically strained compared to the compacting direction. These model predictions all agree with experimental evidence. For the first time a computational model predicts cell orientation in response to this range of mechanical stimuli using a single set of parameters.

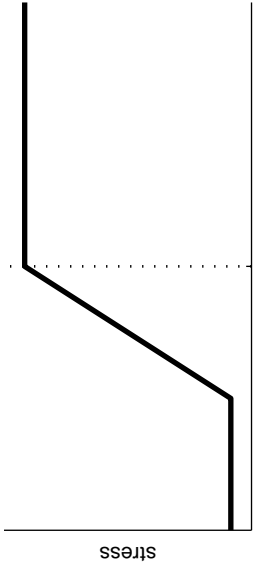
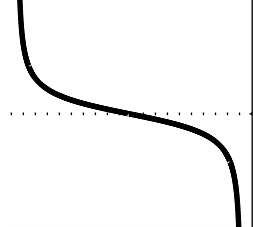
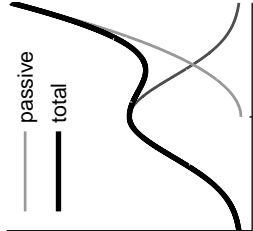
3.1 INTRODUCTION

Many tissues in the human body have a mechanical function. This includes load bearing in bone, damping in cartilage, elastic deformation in skin to accommodate joint movement and active contraction in the heart to circulate blood. When such tissues are damaged their mechanical function is compromised. Repair of damaged tissue, for example by replacement with tissue engineered constructs, can only be successful if the mechanical function is restored as well. For most soft tissues mechanical properties are strongly influenced by the cellular organization, including the orientation of elongated cells. Tissue cells apply traction to their surroundings, mainly in the direction they are oriented in. This is most obvious for muscle cells, but other adhering cells such as fibroblasts and endothelial cells also apply traction forces to their surroundings^[48]. These are mainly generated via the actin cytoskeleton^[5], including actin stress fibers^[28]. Generally, cell and stress fiber orientation coincide^[12,24,26,36,47,48,125]. Cell stiffness is highest in stress fiber direction, and disrupting stress fibers can almost completely abolish mechanical anisotropy^[60]. The influence of cell orientation on tissue mechanics is further increased when the cells produce a collagen matrix parallel to their orientation^[150]. Because cell orientation strongly influences tissue mechanics, understanding and predicting cell orientation is essential to obtain mechanically functioning tissue engineered constructs. Therefore, this paper concentrates on how cells orient in response to mechanical stimuli. Experiments regarding cell orientation in response to mechanical stimuli were initially performed on cells in 2D. When undergoing cyclic strain, different cell types including fibroblasts^[67,98], endothelial cells^[26,69,70,100,125,158,167], smooth muscle cells^[128,169], mesenchymal stem cells^[79], bone marrow-derived progenitor cells^[54] and osteoblasts^[98] respond by orienting approximately perpendicular to the cyclic strain. This has been interpreted as an avoidance response to stretch^[19]. The preference for this orientation increases with

increasing strain rate^[67,137], strain amplitude^[36] or the combination of both^[56,98,149]. A minimal strain amplitude^[12] or frequency^[67] may be necessary for strain avoidance to occur. In a 2D setting, cells have also been shown to orient in response to stiffness anisotropy. In this case, cells orient with a preference for the stiffest direction^[48,119]. Equally increasing the stiffness in both the stiffest direction and the direction perpendicular to the stiffest direction (with a of factor 3.7) did not reveal a noticeable difference in preferred cell orientation, which implies that the difference in stiffness between directions, and not the absolute stiffness, is the predominant factor in this process^[119]. However, when stiffness was extremely large in both directions, the cells could not discriminate between the directions^[119], indicating a (smaller) influence of absolute stiffness. A preferred cell orientation thus develops when cells feel a direction dependent mechanical trigger from their environment. This can either be a difference in amount of cyclic strain, termed *strain anisotropy* here, or a difference of stiffness, termed *anisotropy of mechanical resistance* here.

Next to culturing on a 2D substrate, cells have been cultured in a three dimensional (3D) matrix or gel. In static 3D culture the traction forces applied by the cells lead to compaction of the resulting construct in all directions unless the tissue is constrained^[102]. If the construct is uniaxially constrained, the cells in the construct orient in the constrained direction^[24,47,55,102]. This behavior may be comparable to cells orientating preferably in the stiffest direction in 2D, as in both cases the cells orient towards the direction in which they sense most resistance to deformation. When cyclic strain is applied to such a construct (in the constrained direction) cells still orient preferably in the constrained direction^[47,102]. This strain alignment observed in 3D appears opposite to the strain avoidance observed in 2D and suggests a possible difference in 2D versus 3D stretch^[116]. We hypothesize, however, that cells respond according to the same principles in 2D and 3D. The apparently different behavior in 2D and 3D is then a consequence of the difference in stiffness of the cellular surroundings that are being used: in 2D, cells are often cultured on silicone substrates, including PDMS (about 1MPa^[67]), that are stiffer than the extracellular matrix-like surroundings, such as a fibrin-based matrix (1–12 kPa^[24]) used in 3D. When cells apply traction to a stiff substrate, they sense a high mechanical resistance in all directions independent of the presence of a constraint. When these cells undergo cyclic strain, their orientation is determined by strain anisotropy, as no anisotropy of mechanical resistance is sensed. On or in a low stiffness substrate, on the other hand, the traction forces applied to the surroundings will lead to much larger strains, causing compaction or sensing of a constraint that resists this. A constraint in one direction can therefore be sensed as anisotropy of mechanical resistance. Application of cyclic strain in this case causes the cells to sense both anisotropy of mechanical resistance and strain anisotropy. Our hypothesized theory explains a preference for a cyclically strained but not compacting orientation as a larger influence of the sensed anisotropy of mechanical resistance than of the sensed strain anisotropy. Our hypothesis implies that cells will orient perpendicular to strain in 3D if no anisotropy of mechanical resistance is present. Indeed Gould et al.^[50] found, when biaxially straining collagen hydrogel tissue constructs that were constrained in both directions, most cells oriented in the least strained direction. Also, recent experiments performed by our group^[42] on small scale biaxially constrained cell-populated fibrous tissues suggested that cells

Table 3.1: Similarities and differences between two existing models.

Deshpande et al. [29]	Vernerey and Farsad [142]
<p>Low fiber dissociation at high fiber stress No mass conservation Fiber tension is strain rate dependent</p> 	<p>Stress fibers apply tension to their surroundings Fiber tension is based on a Hill-type muscle model An evolution law leads to most fibers in directions with high tension The separate influence of stress fibers in each direction is homogenized</p> <p>High fiber association at high fiber stress Mass conservation Fiber tension is strain rate and strain dependent</p> 
	

orient away from cyclic strain in 3D, as hypothesized, unless collagen contact guidance dictates otherwise. Because there are fibers in the cyclically strained direction when there is compaction perpendicular to the strain (as is the case in 3D) but not when there is no compaction perpendicular to the strain (2D) our hypothesis implies that the amount of fibers in a certain direction is influenced by mechanical stimuli applied perpendicular to the fiber.

In this paper, we aimed to develop a new model that allows prediction of experimentally observed cell orientations in response to different mechanical stimuli, including anisotropic stiffness of the environment, cyclic tissue deformation, and combined cyclic deformation and compaction of the tissue. Such a model will allow us to predict cell orientation in complex, non-uniform loading conditions.

3.2 PROPOSED MODEL

Existing models

As in general, including the situations discussed here, cell and stress fiber orientation coincide, we will use the main stress fiber orientation as a measure of cell orientation. Two promising models describing stress fiber evolution in response to mechanical stimuli have previously been published: one by Deshpande et al.^[29] and one by Vernerey and Farsad^[142]. In both models, stress fibers apply tension to their environment. This tension is based on a Hill-type muscle model, where a muscle's force depends on its length and shortening velocity, as the structure of stress fibers is similar to that of the myofibrils in myocytes^[142]. Both models have an evolution law where high fiber tension induces either low fiber dissociation^[29] or high fiber association^[142], leading to a large amount of fibers in directions with high fiber tension. In both models, the influence of all stress fibers is homogenized and added to the mechanical properties of the other parts of the cell to determine total cell properties. Here we will not focus on the contribution of other parts, such as intermediate filaments^[29] and cytosol^[142], but we will only consider the contribution of stress fibers to the mechanical properties of the cell. A difference between the two models is that only Vernerey and Farsad take actin mass conservation into account. Furthermore, while a Hill-type contraction law is used in both models, there are differences between the precise laws used. Specifically, Deshpande et al. account for strain rate sensitivity, but not for strain dependency, while Vernerey and Farsad incorporate both. Also, though the general shape of the stress-strain rate function is comparable in both models, they are shifted with respect to each other: in Vernerey and Farsad's model the function is antisymmetric around a strain rate of zero, while in Deshpande et al.'s model it is constant for all positive strain rates. This shift strongly influences the response of the models to cyclic strain. Graphs of these functions, as well as an overview of the similarities and differences between the models, are shown in Table 3.1.

Both models have been shown to accurately predict the static stress fiber concentrations for a square cell attached at its corners, where fiber concentrations are highest in the directions of highest stiffness^[29,142]. Due to the different contraction laws, the models respond differently to certain stimuli. The model by Deshpande et al. predicts strain avoidance in response to cyclic strain, including increased strain avoidance for higher strain amplitudes using a constant frequency^[153] or increased

Table 3.2: Accuracy of expected model predictions for typical experimental tests.

Experiment	Deshpande et al.	Vernerey and Farsad
square cell attached at corners	+	+
strain avoidance for cyclic strain		
at low amplitude	+	+
at high amplitude	+	-
increasing frequency	+	-
increasing strain amplitude	-	+
strain alignment on soft substrate	-	?

+ denotes accurate prediction, - denotes inaccurate, ? denotes unknown

frequency at constant amplitude. As no length-tension relationship is incorporated in this model^[29,153], increased strain avoidance for increasing amplitude at constant strain rate is not described. Also, since in this model cells respond to strain rate only, the influence of cyclic strain generally dominates other stimuli. Strain avoidance will therefore be predicted for cells on or in soft substrates undergoing cyclic strain instead of the strain alignment seen experimentally. Vernerey and Farsad include a length-tension relationship which will cause stress fibers to develop differently for different strain amplitudes. However, because a passive strain hardening response to elongation is incorporated, cyclic strain at large amplitudes will lead to a high fiber tension and thus a (likely unwanted) large amount of fibers in the strained direction. Also, this model does not predict increased strain avoidance for increasing strain frequency, because its velocity-tension relationship is antisymmetric around zero. Since this model takes into account strain and strain rate via separate functions, it can independently sense compaction and cyclic strain. Which of these has the strongest influence on cell orientation depends on the amplitude of cyclic strain compared to compaction and therefore cannot be determined in general. An overview of the accuracy of the expected model predictions for typical experimental tests is shown in Table 3.2.

Currently proposed model

We propose to combine aspects of both of these models, while avoiding their limitations. To allow interdependence of the amount of stress fibers in different directions, actin mass conservation is taken into account^[142] according to:

$$\Phi^{\text{tot}} = \Phi^m + \frac{1}{N} \sum_{\theta} \Phi_{\theta}^p \quad (3.1)$$

with Φ^{tot} total actin volume fraction, Φ^m monomer volume fraction, Φ_{θ}^p stress fiber volume fraction of stress fibers originally having direction θ and N the number of stress fiber directions used. In accordance with Hill's muscle model, stress fibers are assumed to apply tension to their environment in a strain (ε) and strain rate ($\dot{\varepsilon}$) dependent manner:

$$\sigma_{\theta}^p = \sigma_{\text{max}} f_{\varepsilon}(\varepsilon_{\theta}) f_{\dot{\varepsilon}}(\dot{\varepsilon}_{\theta}) \quad (3.2)$$

where σ_θ^p is the stress in a stress fiber which originally had direction θ and σ_{\max} is a constant corresponding to the maximal stress fiber stress. Green-Lagrange strain is used: $\varepsilon_\theta = \frac{1}{2}(\lambda_\theta^2 - 1)$, with λ_θ the stretch ratio in direction θ . The length-tension relationship f_ε is taken from Vernerey and Farsad. It consists of an active component ($f_{\varepsilon,a}$), corresponding to a reduction in active acto-myosin contraction as the absolute strain in a contractile unit differs from zero, plus a passive component ($f_{\varepsilon,p}$) corresponding to a strain hardening response in extension, according to:

$$f_\varepsilon = f_{\varepsilon,a} + f_{\varepsilon,p} \quad (3.3)$$

$$f_{\varepsilon,a}(\varepsilon_\theta) = \exp\left(-\frac{\varepsilon_\theta}{\varepsilon_0}\right)^2 \quad (3.4)$$

$$f_{\varepsilon,p}(\varepsilon_\theta) = \begin{cases} 0 & \text{if } \varepsilon < 0 \\ \left(\frac{\varepsilon_\theta}{\varepsilon_1}\right)^2 & \text{if } \varepsilon \geq 0 \end{cases} \quad (3.5)$$

with ε_0 a constant describing how quickly contraction reduces as strain increasingly differs from zero and ε_1 a constant describing passive strain hardening^[142]. We modeled the velocity-tension relationship $f_{\dot{\varepsilon}}$ comparable to Deshpande et al.^[29] to allow increased strain avoidance when strain rate is increased. For reasons of numerical stability, we replaced the piecewise linear function of Deshpande et al. by a shifted version of the smooth function by Vernerey and Farsad:

$$f_{\dot{\varepsilon}}(\dot{\varepsilon}_\theta) = \frac{1}{1 + \frac{2}{\sqrt{5}}} \left(1 + \frac{k_v \dot{\varepsilon}_\theta + 2}{\sqrt{(k_v \dot{\varepsilon}_\theta + 2)^2 + 1}} \right) \quad (3.6)$$

where k_v is a constant describing how quickly contraction reduces as the rate of shortening increases. As in both existing models, the stress fiber volume fraction is assumed to evolve in time in a stress-dependent manner, with increasing stress fiber stress leading to increased stress fiber formation. However, in our model only the active part of the stress fiber stress influences stress fiber volume fraction, to avoid strain alignment at high strain amplitudes. This leads to (adapted from Vernerey and Farsad^[142]):

$$\frac{d\Phi_\theta^p}{dt} = (k_0^f + k_1^f \sigma_{\max} f_{\varepsilon,a} f_{\dot{\varepsilon}}) \Phi^m - k_d \Phi_\theta^p \quad (3.7)$$

with k_0^f , k_1^f , and k_d constants describing basal stress fiber formation, stress-dependent stress fiber formation, and stress fiber dissociation respectively. The influence of stress fibers in different directions is combined into the total cell stress σ^{cell} as follows:

$$\sigma^{\text{cell}} = \frac{1}{N} \sum_{\theta} \Phi_\theta^p \sigma_\theta^p \vec{e}_\theta \vec{e}_\theta \quad (3.8)$$

where $\vec{e}_\theta \vec{e}_\theta$ is the dyadic product of the unit vector corresponding to the current orientation of a stress fiber originally in direction θ with itself.

3.3 MODEL RESULTS

We aimed to test the performance of the proposed model by analyzing experimental observations. To this end, we implemented the model as a user defined material

Table 3.3: Constants used in all simulations.

parameter	value	unit
Φ^{tot}	$5.0e^{-2}$	-
σ_{max}	$2.0e^{+5}$	Pa
ε_0	$1.2e^{-1}$	-
ε_1	$1.7e^{-1}$	-
k_v	$5.0e^{+1}$	s
k_0^f	$1.5e^{-6}$	s^{-1}
k_1^f	$7.0e^{-7}$	$\text{s}^{-1}\text{Pa}^{-1}$
k_d	$1.0e^{-3}$	s^{-1}

model in the commercial finite element package ABAQUS (SIMULIA, Providence, RI, USA). Model parameters were initially chosen in agreement with literature^[29,142] and manually tuned to obtain qualitative agreement of simulated with experimental results. The resulting set of parameters was used for all results shown in this paper (Table 3.3).

A 2D situation is assumed, where the cell is adhered to a substrate and both experience the same strain. For simplicity, cell and substrate share the same mesh. Twenty stress fiber orientations were taken into account. Initially they are equally spaced in a plane and range from $-\frac{\pi}{2}$ to $\frac{\pi}{2} - \frac{\pi}{N}$. The substrate is modeled as a Neo-Hookean material according to^[160]:

$$\boldsymbol{\sigma}^{\text{NH}} = \left[\kappa \frac{\ln(J)}{J} \mathbf{I} + \frac{G}{J} (\mathbf{F}\mathbf{F}^T - J^{2/3} \mathbf{I}) \right] \quad (3.9)$$

with $\boldsymbol{\sigma}^{\text{NH}}$ the neo-Hookean substrate stress, \mathbf{F} the deformation tensor and $J = \det(\mathbf{F})$. The bulk modulus κ and shear modulus G are defined as $\kappa = \frac{E_{\text{NH}}}{3(1-2\nu)}$ and $G = \frac{E_{\text{NH}}}{2(1+\nu)}$ with ν the Poisson's ratio and E_{NH} the Young's modulus of the neo-Hookean material. Substrate stress is added to cell stress in one user defined material model to simulate stress equilibrium between cell and substrate. A model of a piece of this material, square shaped in the plane in which the stress fibers are defined and with a thickness of 10% of the length of the other edges, was used in all simulations. The momentum equations were solved quasi-statically for this model. All stress fiber volume fractions were initially zero and simulations were run until $t = 10000$ s, when stress fiber volume fractions had reached an equilibrium in all simulations. As the discrete fiber directions taken into account deform with the material, they may no longer be homogeneously distributed when the material is deformed. The amount of fibers in each direction is then a combination of the fiber volume fraction and the density of discrete fibers. We account for the discrete fiber density by dividing the fiber volume fraction in a direction by the ratio of the deformed to the undeformed angle between its two neighboring directions and term the result the scaled fiber volume fraction.

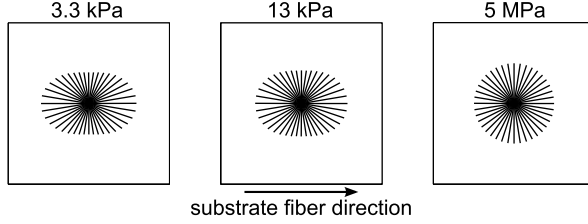


Fig. 3.1: Equilibrium stress fiber distribution for a cell with an anisotropic substrate. The stiffest direction is horizontal, as indicated. In each direction the length of the line is proportional to the scaled fiber volume fraction in this direction. In horizontal and vertical direction, black frames are at a distance from the center corresponding to a scaled fiber volume fraction of 0.1.

Anisotropic substrate stiffness

The predicted stress fiber distribution in response to an anisotropic substrate was determined. To recall, cells orient preferentially in the stiffest direction in vitro, which is mainly determined by the stiffness difference between both directions, unless stiffness is so high that no stiffness difference is sensed^[119]. In this case the substrate was reinforced with linear substrate fibers in a single direction to model anisotropy. The fibers deform with the substrate and their influence is homogenized and added in the substrate material model according to:

$$\boldsymbol{\sigma}^{\text{sub}} = \boldsymbol{\sigma}^{\text{NH}} + E_f \lambda_f \vec{e}_f \vec{e}_f \quad (3.10)$$

where $\boldsymbol{\sigma}^{\text{sub}}$ is the total substrate stress, E_f represents the substrate fiber stiffness, λ_f the substrate fiber Green-Lagrange strain and \vec{e}_f the substrate fiber orientation. Symmetry conditions were imposed to avoid rigid body displacement and no other boundary conditions were applied, to allow free compaction of the material. This homogeneous situation was modeled with 4 hexahedral elements (C3D8). In comparison to Saez et al.^[119], simulations were performed for $E_{\text{NH}} = 3.3 \text{ kPa}$, 13 kPa and 5 MPa , with $E_f = 2E_{\text{NH}}$ in each case (estimated based on Ghibaudo et al.^[48]). Poisson's ratio ν was 0.4 in every simulation. In agreement with experimental results^[119], stress fiber volume fraction was highest in the stiffest direction for the two lower stiffnesses, with no noticeable difference between them, while no preferred direction was observed for the highest stiffness (Fig. 3.1).

Cyclic strain and high stiffness environment

The response of the model to cyclic strain was investigated. To recall, this leads to strain avoidance, which is more pronounced with increased amplitude^[36] and frequency^[137] in vitro. In the simulations a high substrate stiffness of 1 MPa was used, so that cell strain is determined by substrate strain. Two series of three simulations each were performed, one with varying strain frequency and one with varying strain amplitude at constant strain rate. The applied elongation history is shown in Fig. 3.2. The parameters shown in this figure, strain amplitude (A), frequency (f) and time delay (d), as well as the substrate poisson ratio (ν) were chosen in agreement with Faust

Table 3.4: Parameters used in cyclic strain calculations.

	A [-]	f [Hz]	d [s]	ν [-]
1a [†]	0.1	0.01	0	0.19
1b [†]	0.1	0.1	0	0.19
1c [†]	0.1	1	0	0.19
2a [‡]	0.049	0.052	3	0.15
2b [‡]	0.084	0.034	3	0.15
2c [‡]	0.32	0.009	3	0.15

[†] Parameters taken from Tondon et al.^[137]

[‡] Parameters taken from Faust et al.^[36]

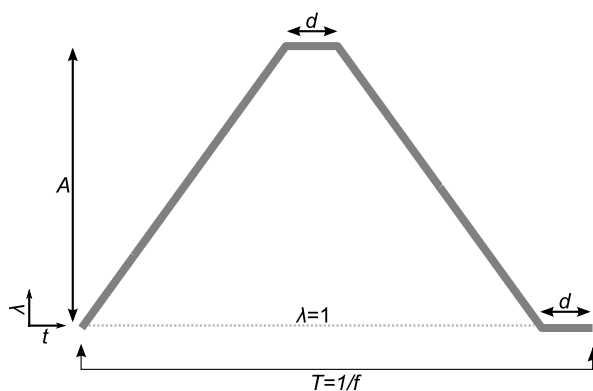


Fig. 3.2: Applied stretch ratio (λ) in time (t) to a cell with a high stiffness substrate during one strain cycle with time period T , equal to the inverse of frequency f . Amplitude (A) and delay between extending and shorting parts of cycles (d) are also shown.

et al.^[36] or Tondon et al.^[137] and are given in Table 3.4. Final stress fiber distributions are shown in Fig. 3.3. It is clear from Fig. 3.3 that indeed the cells avoid strain as the stress fibers are mostly perpendicular to the strain direction, and this effect is stronger with increased strain amplitude or strain frequency.

Cyclic strain and low stiffness environment

The influence of uniaxial cyclic strain on cells in a low stiffness environment was investigated. In this case cell tension compacts the environment in the direction perpendicular to straining. To recall, this is investigated in 3D and cells and stress fibers orient in the strained direction^[47,102] in vitro. However, as the presence of fibrous collagen can influence stress fiber orientation^[42], we adapted an experiment performed previously^[42] to exclude such contact guidance effects. The same model system was used, consisting of silicone posts attached to a flexible membrane with a mixture of cells (human vena saphena cells; $1e^6$ /mL), collagen I (0.45 mg/mL) and matrigel

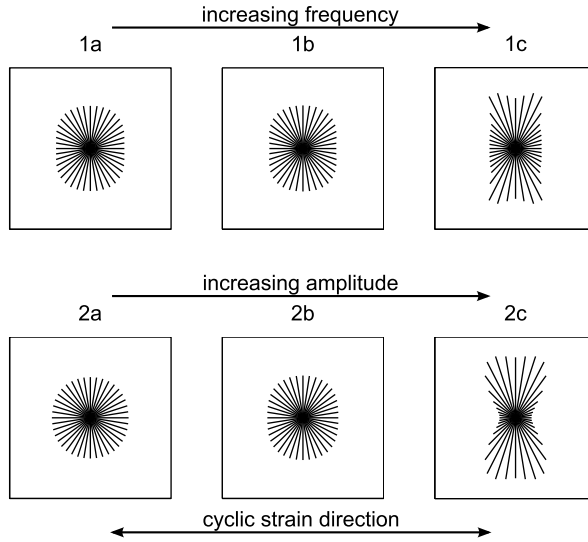


Fig. 3.3: Equilibrium stress fiber distribution for different strain frequencies (*top row*) and strain amplitudes (*bottom row*). Precise simulation parameters are given in Table 3.4. In each direction the length of the line is proportional to the scaled fiber volume fraction in this direction. In horizontal and vertical direction, black frames are at a distance from the center corresponding to a scaled fiber volume fraction of 0.1. Strain is applied in horizontal direction as indicated.

(8.5%) constrained by the posts. The posts prevented compaction in one direction (i.e. a uniaxial constraint) as shown in Fig. 3.4 and Fig. 3.5a. Cyclic strain with a frequency of 0.5 Hz and amplitude of 10% was imposed in the direction of the constraint, by straining the flexible membrane to which the posts were attached. In contrast to the previously published experiment, cyclic strain was now applied immediately after applying the gel in the model system, to investigate the influence of a combination of cyclic strain and anisotropy, and not contact guidance. Upon quantification of the F-actin stress fibers, the dominant orientation was observed to align with the constrained direction, and hence the cyclically strained direction (Fig. 3.5c).

This experiment was simulated using the computational model described previously in this paper. Noting low mechanical resistance and lack of stress fibers in the thickness direction of the 3D gel, stress fibers were modeled in the plane constrained by the posts with the same twenty fiber directions used previously. The gel surrounding the cells was modeled in the same manner as the substrate underlying cells in 2D: as a neo-Hookean material added to the stress fiber stress in a single user defined material model. E_{NH} was 10 kPa, comparable to the stiffness used by Legant et al.^[81] when simulating similar tissue constructs, and ν was 0.4. As described previously, the model was square shaped in the plane in which the stress fibers were defined. Cyclic elongation with a frequency of 0.5 Hz and an amplitude of 10% was applied to one edge of this square, while displacement in y-direction was suppressed along this same edge (at $x = L$) to mimic the influence of the posts. The post geometry is

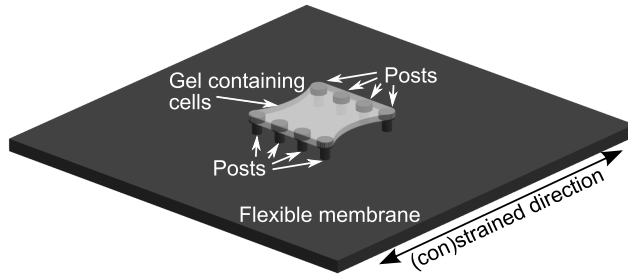


Fig. 3.4: Schematic image of experimental set-up

thus not taken into account explicitly. Symmetry conditions were prescribed to two other edges, so only a quarter of the construct needed to be simulated. The last edge was free to deform. As these boundary conditions lead to heterogeneous deformation, more elements were required compared to previous simulations. A mesh consisting of 145 C3D8 elements was used, with most elements near the corner where the cyclically strained edge meets the free edge, where heterogeneity is largest (Fig. 3.5b). As expected, the relatively low substrate stiffness led to compaction of the construct. In the center region, the main stress fiber direction was oriented with respect to the strained direction, but clearly more stress fibers were oriented in the strained than in the compacting direction (Fig. 3.5d) as was the case experimentally.

3.4 DISCUSSION

A model of mechanically-dependent stress fiber formation was developed by combining features of the models by Deshpande et al.^[29] and Vernerey and Farsad^[142]. In the resulting model, fiber formation increases with increasing active fiber stress, and active fiber stress reduces with increasing absolute strain and with increasing shortening rate. The model qualitatively predicts the following aspects of stress fiber development in response to mechanical stimuli, all observed experimentally:

- development of more fibers in a direction with high resistance to mechanical deformation compared to a direction with lower resistance to mechanical deformation;
- development of fibers mainly in directions not cyclically strained when the cell resides in a high stiffness environment, with increased strain avoidance for increased strain frequency and strain amplitude;
- development of more fibers in a cyclically strained direction than in a non-constrained direction when the cell resides in a low stiffness environment.

We hypothesized that cells behave according to the same principles when subjected to 2D and 3D experimental conditions, despite apparently different behavior when un-

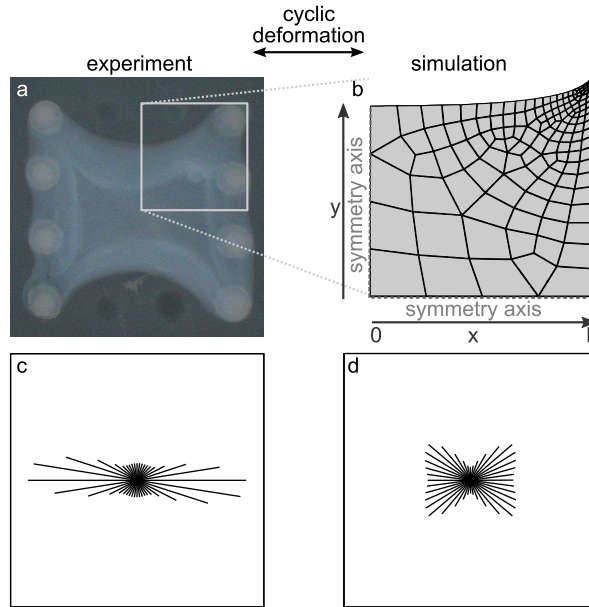


Fig. 3.5: Cell undergoing cyclic strain in a low stiffness environment. **a**: Picture of the experimental set-up (top view). Each circle in this image is the top of a post. **b**: Deformed model at $t = 10000$ s, at this time point the applied strain is 0. Mesh, coordinate system, and symmetry axes are also shown. **c**, **d**: Experimental (**c**) and numerically simulated (**d**) equilibrium stress fiber distribution in the middle of a cell-populated gel undergoing cyclic strain. Both are normalized for comparability. Cyclic strain was applied in horizontal direction while the vertical direction was allowed to compact.

dergoing cyclic strain. Our model predicted both strain avoidance (seen in 2D) and strain alignment (seen in 3D) using the same rules to describe cell behavior. This implies that indeed the seemingly different behavior in 2D and 3D can be caused by the cells “feeling” a different mechanical environment. Although our results correspond qualitatively with experimental observations, there is room for improvement. Particularly, the preferred directions are more distinct experimentally than is predicted by the model. This includes cyclic strain and a low stiffness environment where the main stress fiber direction is oriented with respect to the (con)strained direction, indicating a less dominant response to anisotropy of mechanical resistance compared to strain anisotropy than seen experimentally. The less distinct response may be partly attributed to the single set of parameters used here to describe experiments performed on a range of cell types. Since the overall behavior of different cell types is similar, the use of a single set of parameters to predict the general trends is considered a strength of the model. However, quantitative agreement with experimental results may be improved by optimizing cell type-dependent parameters, as cell type may influence for example the threshold frequency above which a response to cyclic strain occurs^[67]. For cyclic strain and a low stiffness environment we varied the parameters to investi-

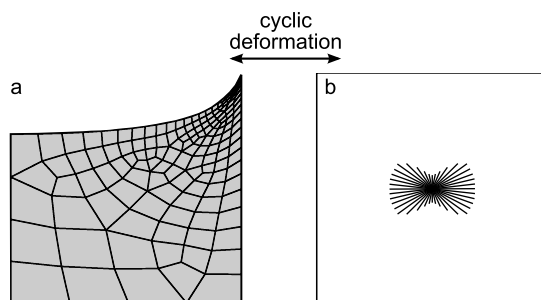


Fig. 3.6: Cell with ε_0 , ε_1 and σ_{\max} multiplied by two undergoing cyclic strain in a low stiffness environment. **a:** Deformed model. **b:** Stress fiber distribution in the center of the construct. Cyclic strain was applied in horizontal direction while the vertical direction was allowed to compact.

gate whether this could lead to a preferred orientation in the (con)strained direction, as seen experimentally and we found that multiplying ε_0 , ε_1 and σ_{\max} by two achieved this (Fig. 3.6).

Also, while the parameters in our model have a physiological interpretation, they were not determined directly from physiological evidence but from parameter tuning to obtain agreement of simulated with experimentally observed stress fiber distributions. It would be an interesting extension of this work to experimentally determine the physiological range of these parameters directly. Furthermore, we did not incorporate any cell components other than the actin cytoskeleton. Though we expect their influence to be small compared to the active contraction of the actin cytoskeleton, such components could add a passive stiffness to the model, comparable to the effect of the substrate we model. If this is taken into account the substrate stiffnesses mentioned are overestimated. This mainly has an influence when substrate stiffness is low, as the passive cell stiffness relative to the substrate stiffness is then largest. We aim to include passive cell properties in the future, but believe our current approach suffices for this qualitative investigation. Other possible future extensions of the model include homogenizing the fiber stress by integration and accounting for non-linear fiber deformation.

3.5 CONCLUSION

We have developed a computational model that accurately predicts trends with respect to stress fiber orientation in response to a range of mechanical stimuli with a single parameter set.

Chapter 4

Computational and experimental investigation of local stress fiber orientation in uniaxially and biaxially constrained microtissues

This chapter is based on:

C. Obbink-Huizer, J. Foolen, C.W.J. Oomens, M. Borochin, C.S. Chen, C.V.C. Bouten, F.P.T. Baaijens (2014) *Computational and experimental investigation of local stress fiber orientation in uniaxially and biaxially constrained microtissues*. Biomech Model Mechanobiol. doi: 10.1007/s10237-014-0554-z. Available online.

ABSTRACT

The orientation of cells and associated F-actin stress fibers is essential for proper tissue functioning. We have previously developed a computational model that qualitatively describes stress fiber orientation in response to a range of mechanical stimuli. In this paper, the aim is to quantitatively validate the model in a static, heterogeneous environment. The stress fiber orientation in uniaxially and biaxially constrained microscale tissues was investigated using a recently developed experimental system. Computed and experimental stress fiber orientations were compared, while accounting for changes in orientation with location in the tissue. This allowed for validation of the model, and additionally, it showed how sensitive the stress fiber orientation in the experimental system is to the location where it is measured, i.e., the heterogeneity of the stress fiber orientation. Computed and experimental stress fiber orientations showed good quantitative agreement in most regions. A strong local alignment near the locations where boundary conditions were enforced was observed for both uniaxially and biaxially constrained tissues. Excepting these regions, in biaxially constrained tissues no preferred orientation was found and the distribution was independent of location. The stress fiber orientation in uniaxially constrained tissues was more heterogeneous, and stress fibers mainly oriented in the constrained direction or along the free edge. These results indicate that the stress fiber orientation in these constrained microtissues is mainly determined by the local mechanical environment, as hypothesized in our model, and also that the model is a valid tool to predict stress fiber orientation in heterogeneously loaded tissues.

4.1 INTRODUCTION

Biological tissues are often mechanically anisotropic. This anisotropy is essential for proper tissue functioning. In the field of tissue engineering, it is therefore necessary to be able to control the anisotropy of engineered neo-tissues. The orientation of cells and their cytoskeletal F-actin stress fibers strongly influences the mechanical anisotropy of tissues. This is both a direct effect, with cells being stiffest in their longitudinal direction^[60] and an indirect effect, with cells producing a collagen matrix parallel to their orientation^[9,150]. One factor influencing cell and stress fiber orientation is their mechanical environment. When cells are embedded in a gel under static loading conditions, their stress fibers are known to orient preferably in directions in which the gel is constrained, both uniaxially^[24,42,55,102] and biaxially^[42,47], leading to a clear anisotropic fiber distribution for uniaxially constrained tissues, or a random fiber orientation for biaxially constrained tissues. In biaxially constrained dynamic conditions, cells tend to avoid cyclic strain^[42,50] unless contact guidance dictates otherwise^[42], while in uniaxially constrained dynamic conditions, cellular stress fibers align in the constrained direction, independent of cyclic strain^[47,102]. It may be possible to induce a preferred direction and degree of cell and stress fiber orientation, as well as tissue anisotropy, by applying appropriate mechanical boundary conditions. A computational model describing how stress fibers orient in response to their mechanical environment can be of great use in determining what these boundary conditions are. Several authors have proposed a model to do this, including Deshpande et al.^[29], Zemel et al.^[168] and ourselves^[103]. Our model qualitatively predicts stress fiber orientation in response to a range of mechanical stimuli with a single parameter set, including strain avoidance in response to cyclic strain and a preferential alignment

in a constrained direction, independent of applied cyclic strain^[103]. In the current paper, we aim to quantitatively validate the stress fiber orientations predicted by our computational model for static boundary conditions. This requires simulating suitable experimental data and comparing experimental and simulated results. Ideally, these experimental data are obtained in a controlled environment that is locally heterogeneous, to validate the response of the model to different mechanical environments as well as the interaction between different regions. Previously, an experimental system to investigate the response of cells to different mechanical stimuli was developed, consisting of posts constraining initially square tissues^[42]. These posts are either located along all edges of the square (biaxial constraint) or in two opposite rows (uniaxial constraint). The mechanical environment in this system is expected to be heterogeneous, in part because boundary conditions are applied to the tissues via discrete posts and not via a continuous constraint. Another interesting system to investigate the interaction between cells and their mechanical environment is the one proposed by Legant et al.^[81], in which two or four small cantilevers constrain a microscale tissue. The small size allows visualization of the entire construct and allows for high-throughput applications, while the deformation of the cantilevers with known bending stiffness quantifies tissue contraction. The small scale is also expected to increase the relevance of heterogeneity within the tissue. In this paper, we combine both systems to obtain small scale tissues that are either uniaxially or biaxially constrained by deformable posts, providing a controlled but heterogeneous mechanical environment in a newly developed high-throughput system. Investigating stress fiber orientation throughout the constrained plane in microtissues allows us to validate the computational model and, additionally, provides data on the heterogeneity of the stress fiber orientation within constrained microtissues. Furthermore, by using two different post heights, corresponding to different post bending stiffnesses, the variety of mechanical environments for the assessment of experimental heterogeneity and the validation of the computational model is increased.

4.2 EXPERIMENTAL METHOD

Experimental model system

Adapted versions of the model system by Legant et al., containing microtissues anchored to posts positioned in four corners^[81], were created (Fig. 4.1). In our system, post geometry and fabrication method were identical to those of Legant et al.^[81]. An array of 8 by 8 microwells was created, containing either a biaxial (12 posts, Fig. 4.1d) or uniaxial (8 posts, Fig. 4.1e) setup, consisting of high (200 μm) or low (125 μm) posts. In short, multilayered masters were manufactured by photopatterning SU-8 photoresist (Microchem) on silicon wafers, via successive spin coating, UV exposure, alignment and baking. Exposure and alignment were performed on a Karl Suss MJB3 mask aligner (Suss Microtec). The masters were developed using propylene glycol methyl ether acetate (PGMEA, Sigma), and were subsequently hard baked. Poly(dimethylsiloxane) (PDMS, Sylgard 184, Dow Corning) replicates were created in a petri dish containing an 0.18 μm thick glass bottom, via an intermediate PDMS casting step to create a substrate. During replication steps, the SU-8 master and PDMS substrate were rendered non-adhesive via plasma treatment (oxygen,

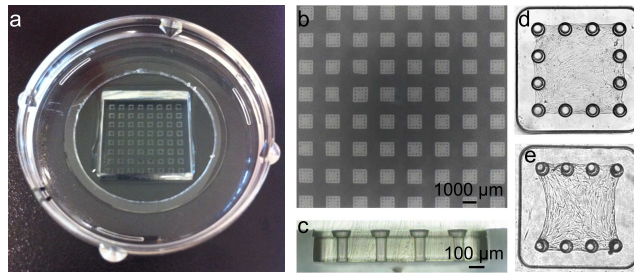


Fig. 4.1: Microtissue model system. **a**: PDMS templates were adhered to a petri dish containing a glass bottom. **b**: Top view of the 8x8 array of microwells; a black pigment was added to the PDMS for a clear overview. **c**: Side view of 4 posts from one microwell. Post diameter was 75 μm at the base and 125 μm at the top, with a total height of 200 μm or 125 μm . **d**: Biaxially constrained microtissue in a single well of 1125 \times 1125 μm . After contraction, the tissues are approximately 800 \times 800 μm . **e**: Uniaxially constrained microtissue

1 min at 100 Watt) and overnight silanization with (tridecafluoro-1,1,2,2-tetrahydrooctyl)-1-trichlorosilane under vacuum. During a second plasma treatment step, PDMS templates were made hydrophilic. Templates were sterilized by treatment with 70% alcohol for 30 min and UV exposure for 15 min. Templates were treated for 2 min with 0.2% Pluronic F127 (BASF) to reduce cell adhesion.

Microtissue seeding

Vascular-derived cells (HVSC, passage 6) characterized as myofibroblasts^[42] were suspended in growth medium (DMEM advanced, 10% FBS, 1% penicillin/streptomycin, 1% glutamax, 260 $\mu\text{g}/\text{mL}$ ascorbic acid). Subsequently, a gel mixture of growth medium, collagen type I (final concentration 1 mg/mL, rat tail, BD Bioscience) and sodium hydroxide, to neutralize the pH of the acidic collagen, was produced in which HVSCs were suspended to obtain a final cell concentration of 14×10^6 HVSCs per mL. To each microwell, approximately 0.16 μL (low posts) or 0.25 μL (high posts) of the cell-gel mixture was pipetted. The microwells were thereby fully submerged. During this procedure, the microwells were kept on ice to prevent evaporation of the gel. Gel seeding was facilitated by making the PDMS hydrophilic in the plasma oxidizer, as previously mentioned. Gels subsequently polymerized in an incubator at 37°C, 5% CO₂ for 10 min. To prevent dehydration of the gel, the petri dish was inverted and sterile water was added to the lid. Subsequently, growth medium was added to the microtissue constructs, which contracted around the posts within 6 h (Fig. 4.2).

Visualization

After 24 h of culturing, microtissues were fixed in 10% formalin for 30 min and permeabilized for 30 min in 0.5% Triton-X in PBS. Microtissues were incubated with phalloidin-Atto 488 (1:100 Sigma) for 30 min at room temperature to visualize F-actin. Fluorescent images were taken with a confocal microscope (Zeiss LSM 510 META NLO, Darmstadt, Germany). The excitation source was an Argon laser (488 nm). The pinhole of the photo-multiplier was set at 8 μm . The photo-multiplier

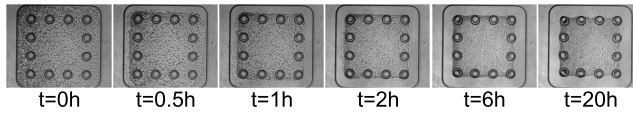


Fig. 4.2: Time span of tissue contraction. Within 6 h of culturing, the tissue is fully anchored around the posts.

accepted a wavelength region of 500–550 nm. No additional image processing was performed. Laser light was focused on the microtissues with a water immersed Achroplan 40×/0.8 NA long distance objective, connected to a Zeiss Axiovert 200 M. Microtissues were visualized through the glass bottom of the petri dish, while the microtissues were still anchored around the posts. Tile scans were produced composed of 4×4 individual images, each individual image measuring 225×225 μm . 2D tile scans were taken at halfway the thickness of the tissue. For each condition (biaxial or uniaxial constraint with high or low posts) five to seven tissues were scanned.

Image analysis

The tile scans showing F-actin fibers throughout the tissues were automatically cropped and divided into four equally sized quarters. These quarters were flipped based on symmetry so that all quarters had the orientation of the quarter in the left top corner. The quarters were divided into four by four equally sized subregions. The F-actin fiber distribution was determined per subregion in a manner comparable to Frangi et al.^[44], originally developed to segment clinical images of blood vessels. The implementation of the algorithm is based on Foolen et al.^[42] and de Jonge et al.^[66]. In brief, a measure of “vesselness” (termed “fiberness” here) is calculated for each point in the image, based on the eigenvalues and eigenvectors of the Hessian matrix of the image intensity (second order derivative). However, in this case the interest is not in a binary value whether or not a vessel or fiber is present on a specific position but in an overall fiber distribution. Therefore, we calculated a histogram of the amount of fibers per direction, where the contribution of the fiber direction at each pixel is weighed with its “fiberness”. Hereby pixels with fiberness close to one, having a high likelihood of belonging to a fiber, strongly contribute to the final histogram, while pixels with a fiberness close to zero have a limited contribution. Pixels with a fiberness below 0.14 were excluded from the histogram, because they could occur without a preferred orientation. Initial trials showed this weighing method increased the smoothness of the histogram, with little influence on the main fiber orientation found, compared with using a cut-off to determine whether or not a pixel(orientation) belongs to a fiber. A more detailed description of the image processing algorithm is provided in Supplementary information: Image processing algorithm. Per subregion the histograms calculated in this manner were summed for all four quarters. This resulted in a total of 16 histograms per image, that were each normalized to have a total weighed amount of fibers of hundred percent. Mean and standard deviation for each point in this series of histograms was then determined over all images corresponding to the same condition (uniaxial or biaxial constraint with high or low posts). From the resulting mean fiber fraction (FF_θ) per direction θ , the direction with largest fiber

fraction (θ_{maxFF}) was determined, along with the strength of alignment around this direction quantified via order parameter S (based on^[168]), defined as

$$S = \frac{\sum_{\theta} FF_{\theta} \cos(2(\theta - \theta_{maxFF}))}{\sum_{\theta} FF_{\theta}}. \quad (4.1)$$

Three regions were defined per tissue (around posts, free edge and central region, shown in Fig. 4.7a, b). For each type of constraint and post height, θ_{maxFF} and S were averaged over the subregions within these regions. As a measure of the force applied by the cells to the posts, the displacement of the posts was determined from the tile scans. The locations of the posts were visible as circular regions without actin staining along the tissue edges. A circle was manually fitted for each post, and the displacement of these circles relative to the designed initial configuration was determined. These displacements were divided in a component parallel and a component perpendicular to the edge, so two displacement values per post per tissue were obtained. Of these 24 (biaxial) or 16 (uniaxial) displacement values per tissue, only 3 (biaxial) or 4 (uniaxial) were expected to be distinct based on symmetry (shown in Fig. 4.6b, e) and all indistinct displacements were averaged.

4.3 COMPUTATIONAL METHOD

Computational model

The experiments were simulated via finite element analysis, using the commercial finite element package ABAQUS (SIMULIA, Providence, RI, USA). The geometry of the entire experimental model system was modeled as a single part, divided into regions to represent the microposts and the cell-populated gel. Only a quarter of the construct was modeled for reasons of symmetry. The dimensions and spacing of the posts correspond to those in the experimental designs. Cells in the relatively large area outside the posts sense hardly any mechanical resistance and undergo extreme deformations. To avoid numerical difficulties arising from these extreme deformations, the simulated initial cell-populated gel geometry was reduced in size compared with the experimental microwell size. The gel was modeled as a cuboid around the tops of the microposts, with 20 μm of gel below and to the sides of the tops of the posts (Fig. 4.3). Four versions of the model were made, corresponding to the uniaxial and biaxial constraint with high or low posts. Linear hexahedral reduced integration elements were used for the microposts and linear hexahedral elements with full integration were used for the gel. A compressible neo-Hookean material model with a Young's modulus (E) of 1 MPa (representative for PDMS^[67]) and a Poisson's ratio (ν) of 0.45 was used to simulate the microposts. The cell-populated gel was modeled as a combination of a cell component, a fibrous collagen component and an isotropic component, all sharing the same mesh. Our previously developed computational model^[103] was used to simulate the cells inside the gel. In brief, in this mechanical model cell stress is determined by a homogenization of the stress in stress fibers in a number of discrete directions. The total stress (σ^{cell}) in all fibers in a direction \vec{e}_{θ} is a weighed (weighting factor w_{θ}) combination of the amount of fibers in this direction (parameterized as

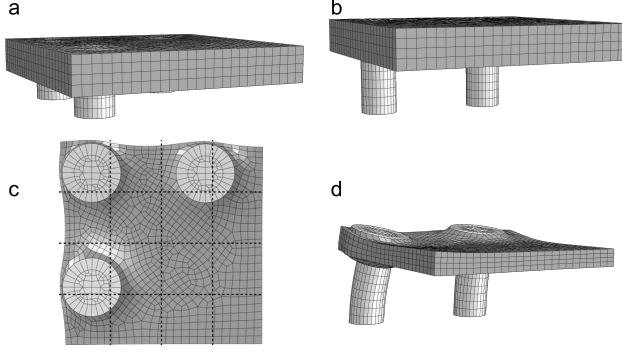


Fig. 4.3: Overview of computational model geometry. Undeformed geometry (**a**, **b**) and deformed geometry (**c**, **d**) for biaxially constrained tissue with low posts (**a**, **c**) or uniaxially constrained tissue with high posts (**b**, **d**). In a top view of the model (**c**) the division in subregions is shown

stress fiber volume fraction Φ_θ^p) and the stress fiber stress in this direction σ_θ^p :

$$\sigma^{\text{cell}} = \sum_{\theta} w_{\theta} \Phi_{\theta}^p \sigma_{\theta}^p \vec{e}_{\theta} \vec{e}_{\theta} \quad (4.2)$$

This stress fiber stress is based on a Hill-type muscle model, where stress is a function of the strain ε (active component $f_{\varepsilon,a}$ plus passive component $f_{\varepsilon,p}$) and the strain rate $\dot{\varepsilon}$ (function $f_{\dot{\varepsilon}}$) according to the following:

$$\sigma_{\theta}^p = \sigma_{\max} f_{\dot{\varepsilon}} (f_{\varepsilon,a} + f_{\varepsilon,p}) \quad (4.3)$$

$$f_{\varepsilon,a} = \exp\left(-\left(\frac{\varepsilon_{\theta}}{\varepsilon_0}\right)^2\right) \quad (4.4)$$

$$f_{\varepsilon,p} = \begin{cases} 0 & \text{if } \varepsilon_{\theta} < 0 \\ \left(\frac{\varepsilon_{\theta}}{\varepsilon_1}\right)^2 & \text{if } \varepsilon_{\theta} \geq 0 \end{cases} \quad (4.5)$$

$$f_{\dot{\varepsilon}} = \frac{1}{1 + \frac{2}{\sqrt{5}}} \left(1 + \frac{k_v \dot{\varepsilon}_{\theta} + 2}{\sqrt{(k_v \dot{\varepsilon}_{\theta} + 2)^2 + 1}} \right) \quad (4.6)$$

A high active stress fiber stress in a direction leads to a large amount of fibers (large stress fiber volume fraction) in this direction according to the following:

$$\frac{d\Phi_{\theta}^p}{dt} = (k_0^f + k_1^f \sigma_{\max} f_{\varepsilon,a} f_{\dot{\varepsilon}}) \Phi^m - k_d \Phi_{\theta}^p \quad (4.7)$$

Furthermore, the total amount of actin, present as either monomer (Φ^m) or fiber (Φ_{θ}^p for angle θ) is constant according to the following:

$$\Phi^{\text{tot}} = \Phi^m + \sum_{\theta} w_{\theta} \Phi_{\theta}^p \quad (4.8)$$

Table 4.1: Material parameters.

parameter	description	value	unit
σ_{\max}	maximal stress fiber stress	$2.0e^{+5}$	Pa
ε_0	how quickly contraction reduces as strain increasingly differs from 0	$1.2e^{-1}$	-
ε_1	passive strain hardening	$1.7e^{-1}$	-
k_v	how quickly contraction reduces as rate of shortening increases	$5.0e^{+1}$	s
k_0^f	basal stress fiber formation	$1.5e^{-6}$	s^{-1}
k_1^f	stress-dependent stress fiber formation	$7.0e^{-7}$	$s^{-1}\text{Pa}^{-1}$
k_d	stress fiber dissociation	$1.0e^{-3}$	s^{-1}
Φ^{tot}	total actin volume fraction	$5.0e^{-2}$	-

The model parameters were unchanged compared with our previous publication^[103] and are given in Table 4.1. Under static conditions, stress fibers mainly develop in directions where they sense large mechanical resistance using this model, as strain is low, and therefore stress is high in such directions. In an extension to our previous work, the discrete fiber directions used, were implemented in 3D and not 2D, with the initial discrete fiber orientations and corresponding weighting factors (w_θ) determined by Lebedev quadrature points^[78]. Since every Lebedev point has a “partner” with the same orientation but opposite direction, only half of the Lebedev grid points are used, in this case 25 orientations, while the weighting factors of both directions are summed. Fibrous collagen was taken into account in the same discrete directions as the stress fibers. The total stress due to all fibrous collagen was a homogenization of the stress in these directions, taking into account the collagen fiber volume fraction, which was 0.02 in all directions. The collagen fibers were assumed to only contribute to stress in extension and an exponential stress-extension (σ - λ) relationship was used:

$$\sigma = \begin{cases} 0 & \text{if } \lambda < 1 \\ k_1 \lambda^2 (\exp^{k_2(\lambda^2-1)} - 1) & \text{if } \lambda \geq 1 \end{cases} \quad (4.9)$$

with k_1 and k_2 taken as 0.676 and 2.75, respectively^[31]. The relatively small influence on tissue mechanical properties of other factors than the ones explicitly taken into account, such as non-contractile cell components and possibly glycosaminoglycans (GAGs), is combined into a single isotropic component, modeled as a low stiffness ($E=50$ Pa, $\nu = 0.2$) neo-Hookean material. This provides some resistance to compression and stabilizes the material. For each of the four model versions, a simulation was run for 10000 s. During this period, an equilibrium stress fiber distribution had developed starting from an initial situation without stress fibers.

Computational model data analysis

To compare experimental and computational results, the output from the simulations — per element the deformation and the stress fiber volume fraction for each direc-

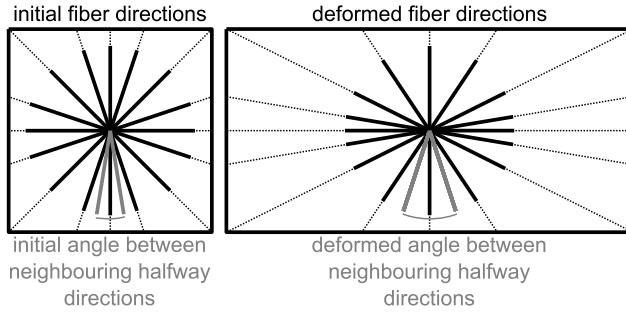


Fig. 4.4: Change in discrete fiber density due to deformation. If there is more extension in one direction than in the other, as depicted here, fiber directions will rotate with the material so the fiber direction density in the most extended direction is increased and fiber direction density in the least extended direction is reduced. To take into account the influence of fiber direction density on fiber fraction, the calculated fiber volume fraction per direction is divided by the ratio of the deformed to the initial angle between the two neighboring halfway fibers. These angles are indicated in the figure for one representative discrete fiber direction

tion — is converted to a series of 4×4 subregion histograms for each case (biaxial or uniaxial with high or low posts). To obtain 2D histograms from the 3D data, the stress fiber volume fractions in the four directions originally in the horizontal plane are considered. Because the number of directions precisely in the horizontal plane is limited, directions under a small angle with respect to the horizontal plane are also included: four directions above the plane (18°) and these four directions mirrored in the plane. Stress fiber volume fractions and initial fiber orientations of mirrored points are averaged, so a total of eight fiber directions and corresponding volume fractions were taken into account per element. The density of discrete fiber directions changes as fibers deform with the material (Fig. 4.4). To take this into account, directions initially halfway between neighboring fiber directions were defined (gray in Fig. 4.4). The stress fiber volume fraction in each direction was then divided by the ratio of the deformed angle between the two halfway directions neighboring the fiber direction to the initial angle between the two halfway directions neighboring the fiber direction. The result is termed the “scaled stress fiber volume fraction”. This scaled stress fiber volume fraction was linearly interpolated between the deformed fiber orientation angles in the horizontal plane to obtain a histogram. The elements were divided into 4×4 same sized subregions, depending on their deformed coordinates (Fig. 4.3c). The histograms of all elements belonging to the same subregion were summed and afterward normalized to have a total value of hundred percent. These are compared with the experimental results. For simulated results θ_{maxFF} and S where determined in the same manner and for the same regions as was done for experimental results, and for each case (biaxial or uniaxial with high or low posts), average values over the different regions (between posts, along free edge, central region) were compared with the corresponding experimental values. To compare the force applied by the cells to the posts in experiment and simulation, for each post, the displacement of the node in the center of the first horizontal layer below the wider top was determined (indicated by

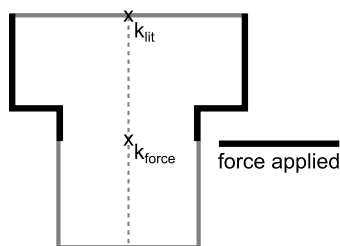


Fig. 4.5: Cut through micropost illustrating bending stiffness calculation. A force is applied equally distributed over the region in contact with the gel when simulating experiments (thick black line). Post displacement is determined at two different locations, to calculate two measures of bending stiffness. Both locations are indicated by an “x” and each is marked with the corresponding stiffness measure.

k_{force} in Fig. 4.5). This location was chosen because in most cases the diameter of the experimentally found post circles was $75\ \mu\text{m}$, the diameter of the base of the post. To estimate the bending stiffness of both a high and a low post, an in time linearly increasing force was applied to each of the posts, evenly distributed over the post surface in contact with the gel when simulating the experiments, corresponding to the entire circumference of the post (Fig. 4.5). Post stiffness was then calculated as the applied force divided by the post displacement in the initial, linear, region. This was done for two measures of displacement: the displacement of the node in the center of the top surface of the post and the displacement of the node in the center of the first horizontal layer below the wider top. Bending stiffness values were termed k_{lit} and k_{force} respectively, as the first stiffness measure is expected to be comparable with literature (including Legant et al.^[81]), while the second measure can be used to estimate the force on the posts from the determined displacement.

4.4 RESULTS

Experimental results

For all conditions (biaxial or uniaxial with high or low posts) close to the posts, stress fibers were mainly oriented between neighboring posts (Fig. 4.6b, d). In the biaxially constrained tissues in the 3×3 subregions not containing posts, there was no dominant orientation and little difference between different subregions (Fig. 4.6b). In the center of the uniaxially constrained tissues, stress fibers were mainly oriented in the constrained direction ($0/180^\circ$). Approaching the free edge of the tissue, the preference became stronger with a main orientation parallel to the free edge. Toward the posts, the preference for the constrained direction reduced (Fig. 4.6d). Results for high and low posts were generally comparable, though in the case of high posts, there was a stronger preference for a single direction in between posts. These effects are also reflected in θ_{maxFF} and S (Fig. 4.7): in regions U1 and B1, and B2, which contain the posts, θ_{maxFF} is 90 or 180° respectively, corresponding to the direction between neigh-

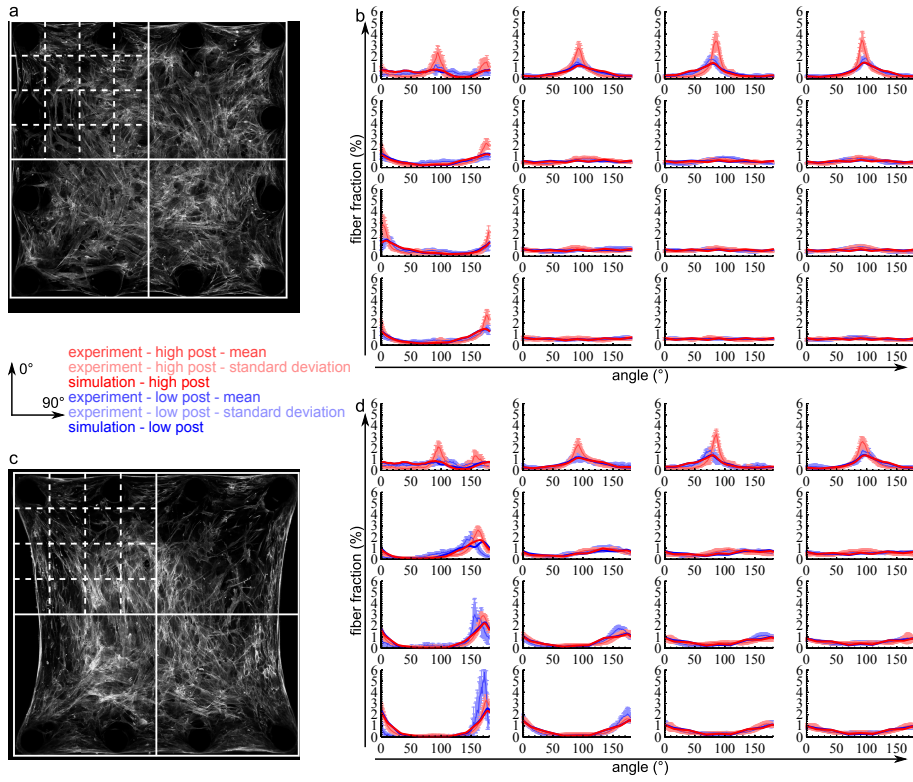


Fig. 4.6: Experimental and simulated results. Representative experimental fluorescent image of F-actin stress fibers, with top left corner divided into subregions (a, c). Histograms showing fiber distribution per subregion (b, d). The arrangement of these histograms corresponds to the grid shown in the top left corner of the representative fluorescent images. A biaxial (a, b) or uniaxial (c, d) constraint is applied

boring posts (Fig. 4.7c, d). In the center of the biaxially constrained tissue (B3) S and thus alignment strength is low (Fig. 4.7f). In the center of the uniaxially constrained tissue (region U3), θ_{maxFF} is close to 180° (the constrained direction, Fig. 4.7c) and S is smaller than the S close to the free edge (region U2), showing alignment strength is less (Fig. 4.7e). θ_{maxFF} was similar in high and low posts, showing the main orientation agreed, while S differed for the post containing regions U1, B1 and B2, showing the strength of this preference differed.

Computational results

Computed and experimental stress fiber distributions agreed well for both the uniaxial and biaxial constraint (Fig. 4.6b, d). Comparable with experimental results, the simulations showed a preferred orientation between neighboring posts, a large homogeneous and randomly oriented central region for the biaxially constrained tissues and a more heterogeneous stress fiber orientation for uniaxially constrained tissues, with

a preferred orientation in the constrained direction or along the free edge. Differences between high and low posts were small in the simulations, as was the case experimentally. The largest discrepancies between experiment and simulation occurred near the posts and along the free edge of the uniaxially constrained tissues. In the numerical simulations, the preference for a specific direction was weaker and no difference between the high and low posts was observed in these regions. Outside these areas, the simulated fiber fraction was almost always within the standard deviation of the experimental mean, indicating quantitative agreement between experimental and simulated results. Again θ_{maxFF} and S values (Fig. 4.7) confirm the results shown in the histograms. For θ_{maxFF} , simulated and experimental mean \pm standard deviation regions overlap for all regions except B3. In this region, alignment is limited, as indicated by a small S , which explains the difference in θ_{maxFF} . Mean simulated S is within a standard deviation of the mean experimental S for the uniaxial free edge and central regions (U2 and U3), but not in the regions containing posts (U1, B1 and B2) as expected based on the histograms (Fig. 4.6b, d). Mean simulated S is more than a standard deviation lower than the mean experimental S in the biaxial central region (B3). Because experimental and simulated histograms are comparable in this region and no preferred orientation is expected based on symmetry considerations, we expect this difference is due to noise on the experimental data, and does not reflect an inaccuracy in the model. Post displacement, which is related to the force applied by the cells in the tissue construct to the posts via post stiffness, was taken into account in the directions indicated in Fig. 4.8a, b. Trends in post displacement were similar in experiment and simulation. For both simulation and experiment, displacement was larger for high posts than for low posts, as expected due to the lower bending stiffness of high posts. For all conditions, post displacement was smallest for the non-corner post in the direction parallel to the edge (direction 3 (biaxial) or 4 (uniaxial) in Fig. 4.8a or b). Displacement in the other directions was approximately equal in most cases. Quantitatively, most of the simulated displacements were larger than the corresponding experimentally observed displacements, but the order of magnitude agreed. The k_{lit} and k_{force} of the high post were 0.8 and 1.4 $\mu\text{N}/\mu\text{m}$ respectively, while the low post had a k_{lit} of 3.6 $\mu\text{N}/\mu\text{m}$ and a k_{force} of 11 $\mu\text{N}/\mu\text{m}$.

4.5 DISCUSSION

Main findings and implications

We aimed to quantitatively validate our computational model, describing stress fiber orientation in response to the mechanical environment. In this model, we assume stress fibers mainly develop in directions in which they can apply high stress, i.e. in directions in which strain and shortening rate are small, even if stress fibers actively try to contract. These are the directions in which the cell senses a large resistance to deformation. When simulating microtissue experiments with our computational model using the same material parameters that were used previously, we found a simulated fiber fraction that was within the standard deviation of the experimentally observed mean throughout most of the mid-plane of the tissue for each of the four conditions investigated (uniaxially or biaxially constrained with high or low posts). When comparing the experimental and simulated displacements, there was qualitative agreement

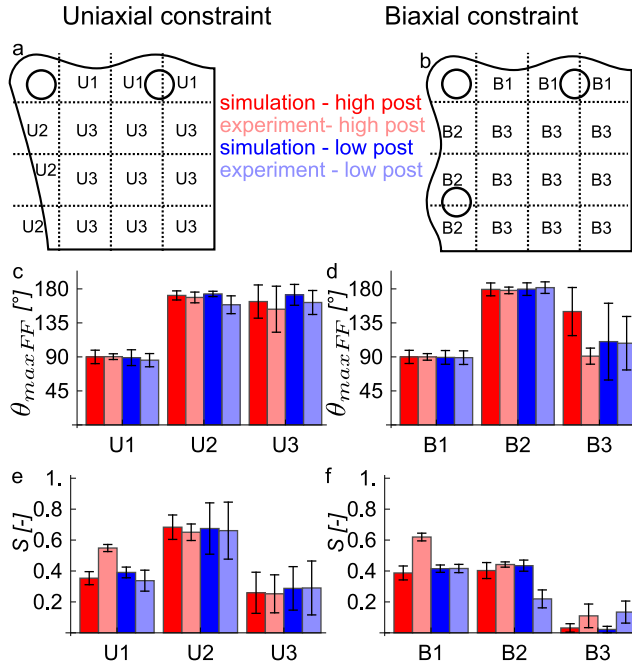


Fig. 4.7: Experimental and simulated stress fiber distributions quantified via θ_{maxFF} and S for different regions. Division in regions is shown for uniaxial constraint (a) and biaxial constraint (b) and results are shown per parameter (θ_{maxFF} (c,d) and S (e,f)) and constraint type (uniaxial(c,e) and biaxial(d,f))

and the orders of magnitude were the same. The agreement between experimental and simulated results supports our hypothesis on stress fiber orientation, as formulated in the model. It indicates that stress fiber orientation in these microtissues is mainly determined by the mechanical environment, and not by, e.g., contact guidance, because our mechanics-based model accurately predicts stress fiber orientation. Because of this good agreement, we suggest that our model can be used to predict stress fiber distributions without the necessity of large amounts of experimental studies, provided mechanical boundary conditions are known. Currently, this is especially the case for static conditions when using comparable tissue constructs, because these conditions have been most extensively validated so far.

Additionally, our experiments provide new evidence on how stress fibers orient in microtissues, including the heterogeneity of stress fiber orientation in these microtissues, while the combination of experimental data with the computational model provides an explanation of why stress fibers orient the way they do. Our experimental results show that the stress fiber orientation is approximately random in biaxially constrained tissues. According to the model, this occurs because cells sense a similar resistance to deformation in all directions in the constrained plane. Between neighboring posts the cells are effectively uniaxially constrained by the posts, and respond

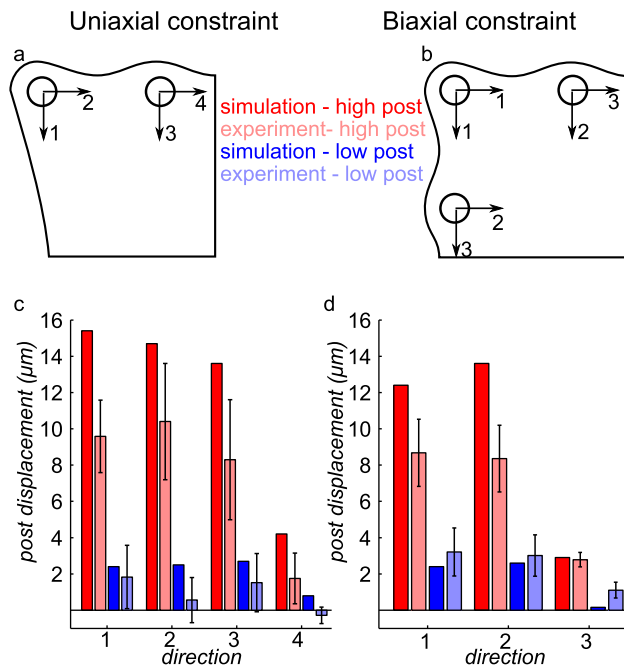


Fig. 4.8: Comparison of simulated to experimental displacements. Definition of directions used to determine displacement for uniaxial (a) or biaxial (b) constraint. Micropost displacement for uniaxial (c) or biaxial (d) constraint including standard deviation over different images for experimental data. This displacement is related to the force applied by the cells in the tissue construct to the posts via post stiffness, which differs between high and low posts.

accordingly. In our model, this happens because cells sense a much larger resistance to deformation in the direction between the posts, than in the perpendicular, free, direction and therefore orient in the direction between the posts. Apart from the subregions containing the posts, no consistent differences between the subregions were found. In the light of our model, this implies resistance to deformation is constant in this region. This homogeneity also indicates that using an off-center or larger image to determine fiber orientation in the biaxially constrained system will not influence results as long as no micropost is directly included in the image used. In the uniaxially constrained tissue, stress fibers develop preferably in the constrained direction, which, according to our model, is due to the increased resistance to deformation in this direction. The stress fiber distribution in the uniaxially constrained tissues is more heterogeneous than in the biaxially constrained tissue. The preferred cell orientation in subregions close to the free edge is more pronounced, while subregions closer to the posts have a less pronounced preferred orientation compared with the center. At the free edge, resistance to deformation is high along the edge, while the material is almost free to deform perpendicular to the edge. In the center of the uniaxially constrained constructs the difference in resistance between constrained and perpendicular direction

is smaller, because in this region the posts provide more resistance to compaction in the perpendicular direction. According to the model, this leads to less pronounced alignment. Closer to the posts, the posts provide even more resistance to compaction, and alignment is further reduced. The preferred direction also changes: from approximately 180° in the center, to 150° (low posts) or 165° (high posts) near the corner post, reflecting a change in the direction of most resistance. Results are thus influenced by the subregion where they are determined in this uniaxially constrained case and this should be taken into account when performing experiments. Also, as the uniaxially constrained microtissues are more anisotropic near the edge, this may be exploited when attempting to develop anisotropic tissues, e.g., by changing the length-width ratio to increase the amount of edge and possibly anisotropy. To test whether an increased tissue length can indeed increase tissue anisotropy, we used our model to predict the stress fiber distribution in a tissue with a twice as high length in constrained direction as the standard simulation. Main stress fiber orientations were similar in the long and the standard tissue. In the center of the construct, the preference for the constrained direction was stronger in the long tissue than in the standard tissue, as expected ($S = 0.6$ in long tissue and 0.2 in standard tissue). In general, this was the case throughout the tissue. However, at the free edge alignment was more pronounced in the standard tissue ($S = 0.7$ at the center of the free edge) than in the long tissue ($S = 0.6$ at the center of the free edge). Apparently, the greater distance to the posts in the long tissue allows a constant alignment strength between construct center and free edge center, while in the standard simulation, the proximity of the posts limits the compaction and therefore alignment at the construct center, while increased compaction is allowed at the free edge, partly due to the presence of tissue material outside the posts. Overall, increasing the tissue length homogenizes the stress fiber distribution around the center of the construct and increases alignment strength except at the free edge. An increased tissue length may therefore be beneficial when attempting to engineer anisotropic tissue constructs.

In general, post height had a limited influence on stress fiber orientation in the range that was tested (125 vs. 200 μm). In the model, competition between directions causes stress fibers to align based on differences in sensed resistance, and not based on absolute resistance. This may explain the limited influence of post height on stress fiber orientation in general. However, higher posts led to a stronger preference for a single fiber direction between posts and, for the uniaxially constrained tissues, a preferred fiber orientation closer to 180° near the corner post. Both effects are consistent with increased compaction for low compared with high posts.

Comparison with literature

The experimental microtissue approach used in the current work is similar to the one described by Legant et al.^[81]. Legant et al.^[81] reported an increase in microtissue tension for cantilevers of increased stiffness. When multiplying the displacement of the posts with the corresponding k_{force} values, we also found an increased force perpendicular to a constrained edge for higher bending stiffness. So, while post stiffness had a limited influence on our main outcome of stress fiber orientation and both bending stiffnesses used in this work are higher than those used by Legant et al.^[81], the bending stiffness difference investigated here was large enough to influence tissue tension.

Legant et al.^[81] also investigated actin orientation and alignment, both experimentally and computationally. As in the current work, actin aligned parallel to free edges, with strongest alignment close to the edges, experimentally and computationally. Due to differences in post locations between Legant et al.^[81] and this work, local actin alignment differed. Notably, a homogeneous region was present in our biaxially constrained tissues, which had additional posts along the edge compared with the four cantilever setup described by Legant et al.^[81]. This homogeneous region, not present in the four cantilever setup, could be valuable when investigating the influence of other factors than mechanical constraints on cell orientation. When comparing the computational modeling approaches, the model used to describe actin fiber development in Legant et al.^[81] is based on Deshpande et al.^[29], while actin fiber development in the current work is based on Obbink-Huizer et al.^[103]. In both models stress fibers mainly develop in directions in which a large resistance to deformation is sensed, but the mechanism by which this is sensed differs: in Deshpande et al.^[29] a low resistance to deformation is sensed as a history of a high fiber shortening rate, while in Obbink-Huizer et al.^[103] a low resistance to deformation is sensed as a large instantaneous negative strain. This different approach influences the versatility of the model to predict the stress fiber distribution, especially in response to mechanical environments with both dynamic strain and an anisotropic resistance to deformation^[103]. Furthermore, unlike Legant et al.^[81], in the current model the post geometry is explicitly taken into account, fiber directions are defined in three dimensions and a fibrous collagen component is included.

Experimental limitations

In some of the images of uniaxially constrained tissues with low posts, part of the tissue was out of focus, so no fibers could be detected. This mainly occurred along the free edges of the tissue and may be due to the attachment height of the tissue to the post. In the subregion corresponding to the center of the free edge, where data are already limited due to the compaction of the tissue, no fibers were found for some images. In another case, only a small amount of fibers were found. If these were to be normalized and averaged with the rest of the data, these few fibers would have dominated results. Therefore, in the mean histogram corresponding to each subregion, only histograms with a total weighed fiber fraction above 5 before normalization were included. We expect this missing data to have limited influence on the mean cell orientation, because it affects fibers independent of their orientation. In the future, in focus images of each part of the tissue can be made by scanning at different depths (3D). We expect this to reduce the standard deviation of the two subregions at the center of the free edge of the uniaxially constrained low-post microtissue, while having little influence on all other results. Therefore, we do not expect an influence on our conclusions.

Computational limitations

The largest discrepancies between experimentally observed and simulated fiber orientation occurred near the microposts and along the free edge of the uniaxially constrained tissue. In these regions, the difference between experimental and simulated geometry was largest: experimentally, the cell-populated gel initially filled an entire

well that was larger than the initial gel geometry taken into account in the simulation. The smaller simulated geometry may lead to reduced compaction perpendicular to the direction constrained by the posts and therefore a less pronounced preferred orientation, as seen in the simulations. Comparing post displacement in experiment and simulation provided an indication of how accurately our computational model describes the force applied by the cells to the post in the experimental model system. The order of magnitude of post displacement in experiment and simulation agreed, but overall the simulation overestimated the displacements. It may be that a difference in attachment height of the tissue to the post causes this discrepancy. In the simulations, we fixed most of the tissue to the top part of the post. Most experimental images showed a post diameter corresponding to the lower part, which might indicate the tissue was mainly fixed at a lower height than assumed in the simulations. The top of the posts requires less force to obtain the same displacement compared with the bottom of the post, which corresponds to a lower bending stiffness at the top than at the bottom of the post. A too high attachment position would result in an overestimation of post displacement in the simulations, which indeed happened in most cases. To accurately assess cell forces in similar microtissues, more detailed experiments are needed, with a more exact and full 3D analysis, including both post displacement and the location on the post where the cells apply force. This is a topic of ongoing research by our group. The difference in effective bending stiffness along the height of the posts did not cause significant differences in stress fiber orientation in different horizontal layers of the tissue, which is consistent with the limited influence of post height on stress fiber orientation that was found. The limited influence of post height on stress fiber orientation along with the more accurate prediction of cell orientation compared with post displacement (and thus force) indicate the stress fiber orientation response is relatively insensitive to changes in stiffness or force. If the tissue was indeed attached lower on the post experimentally than computationally, the true experimental bending stiffness would be higher than the values estimated here. Because uncertainties on the stiffness value lead to increased uncertainty on the force that is calculated from it, we chose to directly compare experimental and simulated deformations as a measure of the force and not the force itself. A continuum approach was taken to model the tissue, while it consists of cells and surrounding matrix, which each have an explicit geometry and interact with each other. As the length scale of the tissue ($\sim 800 \mu\text{m}$) is larger than the size of the cells ($\sim 30 \times 90 \mu\text{m}$), and our simulated results agree well with experimental results, we believe this approach is reasonable. However, if smaller tissues are used, a continuum approach may no longer be valid. While our stress fiber model may still be applicable to the stress fibers themselves, it is likely necessary to include other cell components, such as the nucleus, explicitly. This is beyond the scope of the current work.

Conclusion

Apart from tissue edges where simulated and experimental geometry differed, we obtained good quantitative agreement between experimental and simulated local stress fiber orientations, by assuming stress fibers mainly develop in directions in which they can apply highest stress. In the microtissue system tested, highest stress could be applied in directions in which mechanical resistance was largest: in between neighboring

posts, along a free edge and in constrained directions. In most parts of biaxially constrained tissues, this led to a random and homogeneous stress fiber orientation, while in uniaxially constrained tissues, it led to a heterogeneous stress fiber orientation with an overall preference for the constrained direction, both in the simulations and in the experiments.

ACKNOWLEDGEMENTS

The authors thank F.M.W. Kanters for his contribution to the image processing algorithm.

SUPPLEMENTARY INFORMATION: IMAGE PROCESSING ALGORITHM

The image processing algorithm is based on Frangi et al.^[44] as implemented by Foolen et al.^[42] and de Jonge et al.^[66] and is written using Mathematica 8 (Wolfram Research, Champaign, IL, USA). A grayscale tile scanned image is loaded and its dimensions are determined, typically 4096×4096 pixels. Based on these dimensions, the locations of the tile edges in the image are determined and a mapping matrix is created that has the same size as the image and has a value of 1 for all pixels at least 7 pixels away from tile or image edge and 0 for other pixels. This map is later used to exclude pixels close to (tile) edges when determining fiber distributions, as initial tests showed that edge effects occurred up to 6 pixels from an edge. Subsequently the number of rows/columns with a total pixel value below 3000 is determined starting at each of the outer edges. These rows/columns are not considered part of the relevant image, because they do not show part of the tissue. The relevant image is then divided into four quarters (based on the size of the relevant image) and for each quarter, if available an extra 6 rows/columns are included along each edge, as they will later be excluded due to edge effects. For each quarter, the corresponding part of the mapping matrix is selected. Both image quarter and corresponding mapping matrix section are flipped as necessary so the orientation of all quarters corresponds to the orientation of the left top quarter. Each quarter and corresponding mapping matrix section is then further divided in 4 by 4 subregions, again taking 6 pixels overlap into account. For each subregion, per pixel the Hessian matrix of Gaussian derivatives (second order derivative) is then calculated at scale 2.5. With this scale, fibers found using the image processing algorithm agreed well with visibly apparent fibers. The Hessian matrix was calculated for every pixel in the subregion including tile edges and the 6 pixel wide overlap region on each side, but the result, a matrix containing the Hessian matrix for each pixel, was multiplied by the previously determined mapping matrix section, so only the Hessian matrix at non-edge pixels influences the final result. The eigenvectors and eigenvalues (λ_1 and λ_2 with $|\lambda_1| \leq |\lambda_2|$) of the Hessian matrix were then determined per pixel. A fiber has a gradient of large magnitude perpendicular to the fiber direction (λ_2), and a small gradient parallel to the fiber direction (λ_1), so $\frac{\lambda_1}{\lambda_2}$ is small. Furthermore, for a bright fiber on a dark background as is the case in our images, the fiber will have a higher pixel value than its surroundings, so $\lambda_2 < 0$. The two conditions determined thus far (small $\frac{\lambda_1}{\lambda_2}$ and $\lambda_2 < 0$) are independent of the gray level of the image and therefore background pixels that happen to be brighter than

their surroundings in one direction but not the other may also match these conditions. To avoid this unwanted effect, a third condition is added, that takes into account the absolute value of the eigenvalues and Hessian: $\lambda_1^2 + \lambda_2^2$ and the maximum Hessian norm (c) should be large. All these conditions are combined in a single measure of the likelihood a pixel belongs to a fiber (“fiberness” FN) following:

$$FN = \begin{cases} 0 & \text{if } \lambda_2 \leq 0 \\ \exp^{-2(\frac{\lambda_1}{\lambda_2})^2} (1 - \exp^{-c \frac{\lambda_1^2 + \lambda_2^2}{2}}) & \text{if } \lambda_2 > 0 \end{cases} \quad (4.10)$$

Here the condition is none-zero only for bright fibers on a dark background, the first exponential term is only high for oriented structures and the second term is only high for non-background pixels; higher values of FN thus indicate an increased likelihood of the pixel belonging to a fiber. If a fiber is present, it is oriented in the direction of the eigenvector belonging to λ_1 (v_1). Per subregion, an overall histogram of amount of fibers per direction is determined by summing FN over all pixels with v_1 in the same 1° -wide bin. Each summed FN per angle was then divided by the summed FN of all angles combined and multiplied by 100% to obtain fiber fractions. Only pixels with a $FN > 0.14$ were included, as the first exponential term is 0.14 if $\lambda_1 = \lambda_2$ and no preferred orientation is present. This was done for all subregions in all quarters and all images and histograms where averaged per case (uniaxial or biaxial with high or low posts) and subregion.

Chapter 5

Collagen and fibroblast orientation in the infarcted heart: cause and consequence

This chapter is based on:

C. Obbink-Huizer, C.W.J. Oomens, P.H.M. Bovendeerd, C.V.C. Bouten, F.P.T. Baaijens (2014)
Collagen and fibroblast orientation in the infarcted heart: cause and consequence. Manuscript
in preparation.

ABSTRACT

After myocardial infarction (MI), the mechanical properties of the infarcted myocardium greatly influence the remaining heart function. The orientation of collagen in the infarcted tissue is an important determinant of tissue mechanical properties. The ability to predict infarct collagen orientation may therefore improve rational MI therapy design. A recently proposed model describes collagen orientation as a consequence of cell orientation, with cells preferably orienting in the direction of (cyclic) strain. However, in vitro, cells are known to preferably orient away from cyclic strain. In the current work, we determine expected cell orientations in the infarcted heart based on current knowledge of the in vitro cell orientation response. This was done by using a previously developed left ventricle model to assess infarct deformation throughout the cardiac cycle, and applying this deformation to a previously developed cell orientation model. Variations of the model are tested to investigate the robustness of results under model uncertainties. Though variations in deformation were observed, the preferred cell orientations predicted by our model were consistently perpendicular to experimentally observed main collagen orientations. This indicates that mechanisms other than strain avoidance underlie the cell and collagen orientation in the infarcted heart. We propose an alternative mechanism: under high loading, as occurs in the heart, cells are not able to reorient collagen fibers and align with them instead.

5.1 INTRODUCTION

In patients suffering from a myocardial infarction, the pumping capacity of the heart is reduced because part of the contractile myocardial tissue is replaced by non-contractile scar tissue. The passive mechanical properties of the infarct greatly influence the remaining heart function. Both soft and stiff infarcts can negatively influence heart function: a soft infarct impedes systolic function because the infarct bulges under pressure, while a stiff infarct leads to reduced diastolic filling and reduced shortening of healthy cardiomyocytes bordering the infarcted area^[59]. Besides directly influencing instantaneous cardiac function, an infarct may indirectly cause reduced cardiac function and possibly heart failure on the long term, by triggering left ventricular remodeling^[59]: the infarct causes increased wall stress, leading to left ventricular dilation and further increases in wall stress in a vicious cycle^[109]. Infarct tissue may^[38] or may not^[53] behave isotropically under biaxial mechanical testing. An anisotropic infarct may be beneficial by allowing diastolic filling without systolic bulging and is hypothesized to limit the necessity of ventricular remodeling^[39,40]. Infarct scar tissue primarily consists of collagen and the organization of this collagen is an important determinant of the mechanical properties of the tissue^[155]. In dogs, humans and pigs aligned collagen fibers have been found in infarct scar tissue, one to six weeks after infarction (dog^[156] and pig^[58,170]) and in hearts with end stage ischemic heart disease (human^[157]). In rats, a main collagen orientation (in circumferential direction) has been observed in mid-ventrically located infarcts^[41], but not in infarcts located at the apex^[38,41].

Several therapeutic approaches have been proposed that aim at influencing cardiac mechanics in the infarcted heart, by regenerating the myocardium via attraction or delivery of cells, by preventing negative left ventricular remodeling and dilation via the delivery of a passive, cell-free material, or by combining both approaches^[25,90,112]. Though many studies mention improved cardiac function with such therapies in animal models, the mechanisms by which these therapies influence cardiac function and

left ventricular remodeling are not yet understood^[112]. Computational models may improve our understanding of such mechanisms and allow more rational therapy design. Specifically, a computational model describing how oriented collagen develops in infarcted tissue may aid in determining the influence of various proposed therapies on scar mechanical properties and in designing a therapy that leads to specific anisotropic properties. An interesting step in this direction was taken by Fomovsky et al.^[41] and Rouillard and Holmes^[118]. They developed an agent-based model of infarct healing, taking into account the influence of a mechanical, a contact guidance and a chemical guidance cue on the orientation and migration of fibroblasts in the infarcted tissue, while these fibroblasts produced, degraded and reoriented collagen. Of these cues, the mechanical cue was critical to reproduce the experimentally observed collagen alignment in healing infarcts. End-systolic with respect to end-diastolic strain in circumferential and longitudinal directions were used as mechanical cue. Fibroblasts were assumed to preferably orient in strained direction. However, during *in vitro* experiments, cells commonly align perpendicular to cyclic strain when no other stimuli are present, both on 2D substrates^[26,36,54,67,69,70,79,98,100,125,128,137,158,167] and in 3D gel environments^[42,50]. Because the heart deforms in a cyclic manner, strain is expected to provide an avoidance and not an alignment cue to fibroblasts in the heart. Cardiac deformation is complex and changes in time. This was not fully taken into account as part of the mechanical cue in the model by Fomovsky et al.^[41] and Rouillard and Holmes^[118]. Specifically, end-systolic with respect to end-diastolic strain may not reflect the amount of cyclic strain during an entire cardiac cycle. Furthermore, shear strains and transmural variations in strain may influence the deformation of the tissue. Therefore, in the model by Fomovsky et al.^[41] and Rouillard and Holmes^[118] the direction in which most cyclic strain occurs may be obscured.

We have recently developed a computational model in which a strain avoidance response is included^[103]. This model predicts the orientation of fibroblasts in response to their mechanical environment based on their internal stress fiber distribution. In the current work, we aim to determine whether the main collagen orientation observed experimentally in myocardial infarcts can be explained as a co-alignment of collagen with fibroblasts orienting based on their deformation, as hypothesized by Fomovsky et al.^[41] and Rouillard and Holmes^[118]. We take into account the cyclic deformation of the heart and assume fibroblasts follow the same strain avoidance principles *in vivo* and *in vitro*. We do this via a two-step approach. First, we estimate the deformation in the infarct using a previously developed model of the entire left ventricle^[17]. Then, we apply this deformation to our cell orientation model^[103]. This is done for infarcts of different shapes and at different locations, simulating the infarcts described by Fomovsky et al.^[41]. By comparing the cell orientations predicted by our model to the collagen orientations determined by Fomovsky et al.^[41], we can determine whether it is likely that this collagen orientation is a consequence of strain-induced fibroblast alignment. The results provide increased understanding of the mechanism determining collagen orientation in infarcted myocardium and indicates directions of further research, both *in vitro* and *in vivo*.

5.2 METHOD

Model of infarcted left ventricle

Infarct deformation is calculated using a model of left ventricle (LV) mechanics that has been described previously^[17]. Briefly, endo- and epicardial LV surfaces are modelled as truncated confocal ellipsoids in the stress-free reference configuration, with the space between them representing the thick walled myocardium. The modelled wall and cavity volumes are 136 ml and 44 ml respectively^[15]. Local myofiber direction is defined as a combination of a transmural component (transverse angle α_t) and a base-to-apex component (helix angle α_h) and varies with position as shown in Fig. 5.1^[140].

Myocardial tissue stress σ consists of a passive component σ_p , and an active component σ_a , which is weighed with a factor w_a to allow infarct simulation and contributes to the stress only in muscle fiber direction \vec{e}_f :

$$\sigma = \sigma_p + w_a \sigma_a \vec{e}_f \vec{e}_f \quad (5.1)$$

Active stress in the basic unit of the muscle fiber, the sarcomere, is modelled via a contractile element in series with an elastic element and depends on time elapsed since activation, total sarcomere length and contractile element length^[17]. Details of the active stress definition are given in the Appendix. Passive material behavior is assumed to be nonlinearly elastic, transversely isotropic and nearly incompressible, with passive Cauchy stress related to the strain energy density function W via deformation gradient tensor \mathbf{F} according to^[72]:

$$\sigma_p = \frac{1}{\det(\mathbf{F})} \mathbf{F} \cdot \frac{\partial W}{\partial \mathbf{E}} \cdot \mathbf{F}^T; \quad \mathbf{E} = \frac{1}{2}(\mathbf{F}^T \cdot \mathbf{F} - \mathbf{I}). \quad (5.2)$$

W is defined in terms of invariants (\mathbf{I} , \mathbf{II} , \mathbf{IV}) of the Green-Lagrange strain \mathbf{E} in a material-based coordinate system with f the fiber direction, and s and n located in the transverse isotropic plane: $\mathbf{I}_E = E_{ff} + E_{ss} + E_{nn}$, $\mathbf{II}_E = E_{fs}^2 + E_{sn}^2 + E_{nf}^2 - E_{ff}E_{ss} - E_{ss}E_{nn} - E_{nn}E_{ff}$, $\mathbf{IV}_E = E_{ff}$. W is composed of a part related to volume change (W_v) and a part related to shape change, consisting of an isotropic (W_i) and an anisotropic (W_f) component:

$$\begin{aligned} W &= W_v + W_i + W_f = \\ &a_5[\det(\mathbf{F}^T \cdot \mathbf{F}) - 1]^2 + a_0(\exp^{a_1 \mathbf{I}_E^2 + a_2 \mathbf{II}_E} - 1) + a_3(\exp^{a_4 \mathbf{IV}_E^2} - 1) \end{aligned} \quad (5.3)$$

Parameters were chosen as defined in Table 5.1.

The equations of conservation of momentum are solved in the model:

$$\vec{\nabla} \cdot \sigma = \vec{0}. \quad (5.4)$$

Rigid body motion is suppressed by defining essential boundary conditions at the base. Pressure is zero on the epicardial surface, while a uniform left ventricular pressure p_{lv} is applied to the endocardial surface. During filling and ejection phases p_{lv} is

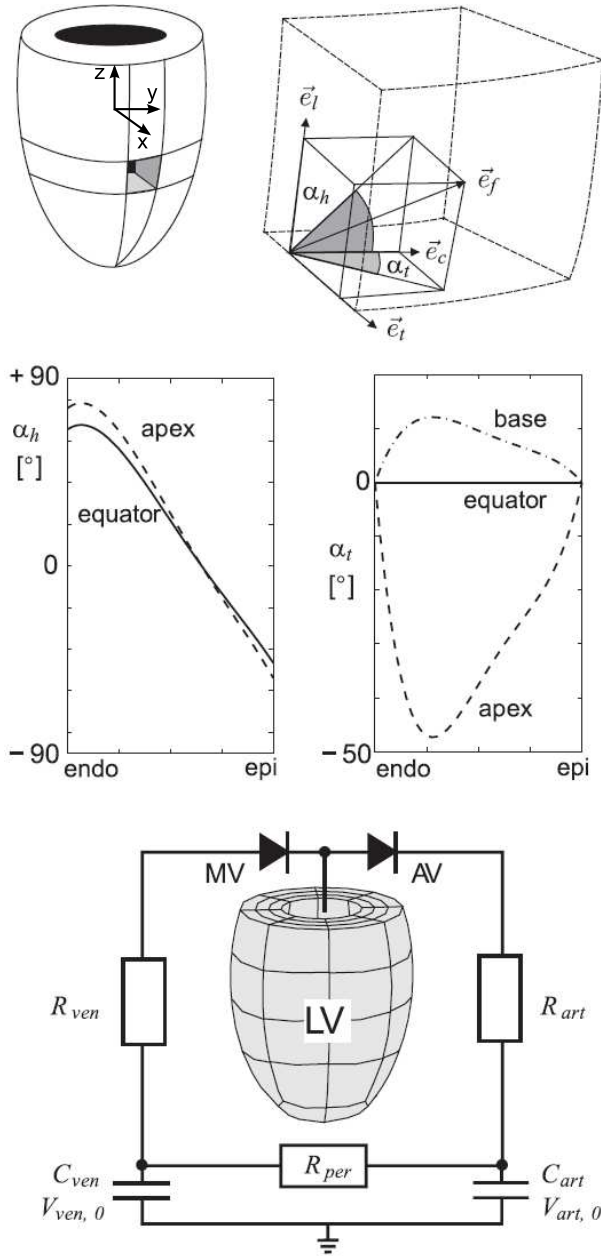


Fig. 5.1: Left ventricle model. *Top row*: ellipsoidal geometry showing global (x,y,z) coordinate system and definition of fiber direction (\vec{e}_f), based on helix angle α_h and transverse angle α_t , defined relative to the local circumferential (\vec{e}_c), longitudinal (\vec{e}_l) and thickness (\vec{e}_t) directions. *Middle row*: Variation of helix and transverse angles between endocardium (endo) and epicardium (epi) used in all simulations. *Bottom*: lumped parameter model of the circulation. Parameters are described in the text and parameter values are given in Table 5.3. Image based on Bovendeerd et al.^[17]

Table 5.1: Passive material parameters as used in equation 5.3. Parameter values are based on Kerckhoffs et al.^[72].

parameter	value	unit
a_0	0.6	kPa
a_1	3	-
a_2	6	-
a_3	0.01	kPa
a_4	60	-
a_5	55	kPa

Table 5.2: Values of parameters in circulation model shown in Fig. 5.1^[17].

parameter	value	unit
R_{art}	0.01	kPa s ml ⁻¹
R_{per}	0.12	kPa s ml ⁻¹
R_{ven}	0.005	kPa s ml ⁻¹
C_{art}	25	ml kPa ⁻¹
C_{ven}	600	ml kPa ⁻¹
$V_{art,0}$	500	ml
$V_{ven,0}$	3000	ml
V_{tot}	5000	ml

computed from the interaction of the LV with the circulation, modelled in a lumped parameter model (Fig. 5.1). Aortic and mitral valves are modelled as perfect diodes, allowing flow in only one direction. Constant resistances representing arteries (R_{art}), peripheral vessels (R_{per}) and veins (R_{ven}) are incorporated, each having a pressure drop of $\Delta p_R = Rq$, with q the flow through the resistance. Capacitances representing arteries (C_{art}) and veins (C_{ven}) are also included, which each have a pressure drop of $\Delta p_C = \frac{V-V_0}{C}$, with V_0 representing the volume at zero pressure. Blood volume in the LV cavity plus the arterial and venous capacitances equals the total blood volume V_{tot} . Parameter values are given in Table 5.2. For each point in time during isovolumetric contraction and relaxation phases, p_{lv} is taken such that LV volume stays constant during these phases.

An infarct is simulated as a local reduction of active contractility, via weighing factor w_a . Following Fomovsky et al.^[41] infarcts of different shapes and at different locations are simulated: a circular infarct at the apex (A), and circular (M), circumferentially oriented ellipsoidal (CE) and longitudinally oriented ellipsoidal (LE) infarcts at the mid-ventricle. Per infarct, a center point was defined on the epicardial wall at $y = 0$ (Fig. 5.2). The size of our LV model was larger than the rat hearts analysed by Fomovsky et al.^[41]. Because rat heart volume was not given, but rat mass was,

Table 5.3: Parameters describing the geometry of the different infarcts, including short to long axis ratio (r_{sl}), radius in long axis direction (R_l), radius in short axis direction (R_s) and parameters to orient ellipsoidal infarcts (r_y and r_z).

	A	CE	M	LE
area (mm ²)	756	713	1355	807
r_{sl}	1	1/2	1	1/2
R_l (mm)	16	21	21	23
R_s (mm)	16	11	21	11
r_y	1	1	1	r_{sl}
r_z	1	r_{sl}	1	1

we multiplied rat body weight by an LV weight to body weight ratio of 2.15 mg/g^[38] and divided the result by a tissue density of 1.06 g/cm³^[41], to obtain an estimated rat heart volume. Comparison of this estimated rat heart volume to the LV wall volume in our model led to a volume scaling factor f_V . From this, an area scaling factor of $f_V^{3/2}$ was derived, equal to 33.6. The infarct areas given by Fomovsky et al. were scaled by this factor. Infarcted regions were modeled as ellipsoids with a shortest axis length (R_s) to longest axis length (R_l) ratio of r_{sl} . R_l then equals $\sqrt{\frac{A}{\pi r_{sl}}}$. For each node in the model, the ellipsoidal radius to the infarct center point was determined as $r = \sqrt{dx^2 + (\frac{dy}{r_y})^2 + (\frac{dz}{r_z})^2}$ with dx , dy and dz the distance from the node to the infarct center in the global x, y and z direction respectively and r_y and r_z enabling ellipsoidal infarct shapes at the mid-ventricle (Table 5.3). The active weighing factor was assumed to have a constant value of zero in the center of the infarct, while w_a linearly increases with the ellipsoidal radius towards the infarct borders, according to:

$$w_a = \begin{cases} 1 & \text{if } r > R_l \\ \frac{r-R_l/2}{R_l/2} & \text{if } R_l/2 < r < R_l \\ 0 & \text{if } r < R_l/2 \end{cases} \quad (5.5)$$

Conservation of momentum was solved numerically using a Galerkin-type finite element method. The LV-wall was represented by 432 27-noded hexahedral elements, using tri-quadratic interpolation of the displacement field. The model was run for 3200 ms, corresponding to 4 cardiac cycles. At this point, a cyclic steady state was obtained. For each simulation, output from the last cycle was analysed, starting at end diastole, defined as the time point when venous inflow to the heart becomes zero. Per node, the deformation tensor in the global (x,y,z) coordinate system with respect to the unloaded reference state was written as output for each point in time.

For comparison to the experimentally observed strains given by Fomovsky et al.^[41], in each simulation the deformation of the center infarct node on the epicardial surface was selected. Because Fomovsky et al.^[41] determined strain at end systole with respect to end diastole, the deformation tensor with respect to the unloaded state at end

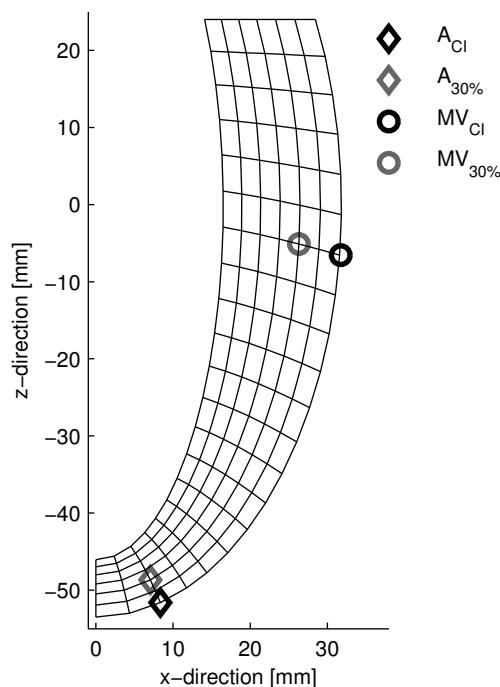


Fig. 5.2: Cross-section of half the LV showing all nodes in a grid while highlighting the position of the center infarct (CI) node and the node closest to 30% transmural thickness towards the endocardium (30%) for an infarct at the apex (A) and at the mid-ventricle (MV).

systole (end aortic flow) was multiplied by the inverse deformation tensor at end diastole (end venous flow). From this deformation tensor \mathbf{F}_{ED} the Green-Lagrange strain tensor $\mathbf{E}_{ED} = \frac{1}{2}(\mathbf{F}_{ED}^T \cdot \mathbf{F}_{ED} - \mathbf{I})$ was calculated and the strains in circumferential and longitudinal direction were extracted. Circumferential and longitudinal strains for all simulations were plot in a histogram, along with the corresponding values obtained experimentally by Fomovsky et al.^[41].

Cell orientation model

After LV deformation was calculated, the next step in our two-step approach was to determine the expected orientation of fibroblasts in the infarcted region, based on the internal stress fiber orientation that is predicted using a previously developed computational model^[103]. For this, fibroblasts were assumed to be adhered in parallel to the infarcted heart. They therefore deform along with the infarcted heart, so the infarct tissue deformation tensor also describes the cellular deformation. As a measure of cell orientation, stress fiber orientation was calculated for the node closest to the point at 30% wall thickness towards the endocardium relative to the epicardial infarct center node (Fig. 5.2), for comparison to the collagen orientations found by Fomovsky et al.^[41]. The amount of stress fibers (parameterized as stress fiber volume fraction

Φ_θ^p for direction θ in the model) was taken into account in 385 unique directions, corresponding to Lebedev quadrature points^[78] each having a corresponding Lebedev weight factor w_θ . The orientation of these fiber directions was chosen in such a way that there was a fiber pointing exactly in each of the local cardiac system directions: circumferential, longitudinal and thickness direction. Green-Lagrangian strain and strain rate in each of these directions were calculated from the deformation tensor with respect to the unloaded state for each point in time during the cardiac cycle. Stress fibers were assumed to cyclically deform according to this deformation pattern. In our model^[103], stress fiber stress in direction θ (σ_θ^p) is based on a Hill-type muscle model. σ_θ^p depends on strain (ε_θ) via an active ($f_{\varepsilon,a}$) plus passive ($f_{\varepsilon,p}$) function and on strain rate $\dot{\varepsilon}_\theta$, via the function $f_{\dot{\varepsilon}}$ according to:

$$\sigma_\theta^p = \sigma_{\max} f_{\dot{\varepsilon}}(f_{\varepsilon,a} + f_{\varepsilon,p}) \quad (5.6)$$

$$f_{\varepsilon,a} = \exp^{-\left(\frac{\varepsilon_\theta}{\varepsilon_0}\right)^2} \quad (5.7)$$

$$f_{\varepsilon,p} = \begin{cases} 0 & \text{if } \varepsilon_\theta < 0 \\ \left(\frac{\varepsilon_\theta}{\varepsilon_1}\right)^2 & \text{if } \varepsilon_\theta \geq 0 \end{cases} \quad (5.8)$$

$$f_{\dot{\varepsilon}} = \frac{1}{1 + \frac{2}{\sqrt{5}}} \left(1 + \frac{k_v \dot{\varepsilon}_\theta + 2}{\sqrt{(k_v \dot{\varepsilon}_\theta + 2)^2 + 1}} \right). \quad (5.9)$$

The amount of fibers in each direction changes in time depending on active stress fiber stress according to:

$$\frac{d\Phi_\theta^p}{dt} = (k_0^f + k_1^f \sigma_{\max} f_{\varepsilon,a} f_{\dot{\varepsilon}}) \Phi_\theta^m - k_d \Phi_\theta^p \quad (5.10)$$

Furthermore, stress fibers contain actin, which is present either as monomer (Φ^m) or as fiber (Φ_θ^p), while the total amount of actin is constant:

$$\Phi^{\text{tot}} = \Phi^m + \sum_\theta w_\theta \Phi_\theta^p. \quad (5.11)$$

All parameter values are given in Table 5.4 and were chosen according to Obbink-Huizer et al.^[103].

An equilibrium stress fiber distribution was calculated using an explicit integration scheme starting without fibrous actin for each of the infarct shapes. The final stress fiber volume fractions of fiber directions initially in the circumferential-longitudinal plane were plotted for each simulation and this stress fiber distribution was assumed to be representative of the distribution of fibroblast cell orientations. The total stress developed in the cell due to the stress fibers (σ^{cell}) was also calculated, as:

$$\sigma^{\text{cell}} = \sum_\theta w_\theta \Phi_\theta^p \sigma_\theta^p \vec{e}_\theta \vec{e}_\theta. \quad (5.12)$$

Here \vec{e}_θ is a unit vector oriented in current direction θ . For comparison, stress was extracted from the LV model at the position where cell orientation and stress were determined.

Table 5.4: Stress fiber development model parameters.

parameter	description	value	unit
ε_0	how quickly contraction reduces as strain increasingly differs from 0	$1.2e^{-1}$	-
k_v	how quickly contraction reduces as rate of shortening increases	$5.0e^{+1}$	s
k_0^f	basal stress fiber formation	$1.5e^{-6}$	s^{-1}
k_1^f	stress-dependent stress fiber formation	$7.0e^{-7}$	$s^{-1}Pa^{-1}$
k_d	stress fiber dissociation	$1.0e^{-3}$	s^{-1}
Φ^{tot}	total actin volume fraction	$5.0e^{-2}$	-

Variations

Several aspects of the model were changed, to determine whether inaccurate assumptions in these factors would influence results. First of all, the predicted stress fiber distribution was calculated for nodes at all transmural depths relative to the center infarct node. This shows whether small differences in transmural location are likely to influence the predicted cell orientation, and also whether transmural changes in cell orientation are expected at all. Secondly, the strain was determined for the 9 nodes closest to the infarct center on the epicardial wall, i.e. the center infarct node and the 8 nodes surrounding it. Stress fiber distributions were calculated for the 9 nodes at 30% transmural depth closer to the endocardium compared to these nodes. This was done so no conclusions will be drawn based solely on a very local effect. Thirdly, the stress fiber distribution was calculated assuming the amount of fibers is only influenced by strain rate, and not by strain:

$$\frac{d\Phi_\theta^p}{dt} = (k_0^f + k_1^f \sigma_{\max} f_\varepsilon) \Phi^m - k_d \Phi_\theta^p. \quad (5.13)$$

Since fibroblasts may actively compact their local environment, the difference between tissue strain and cellular strain is expected to be larger than the difference between tissue strain rate and cellular strain rate. By excluding the influence of strain on stress fiber distribution, we ascertain that the predicted stress fiber distribution is not dominated by the influence of strain. These three variations did not require additional simulations with the LV model. Furthermore, we increased the passive stiffness of the infarcted region proportional to the reduction in active contraction, by multiplying passive stress with a factor. This factor was two at the center of the infarct. This shows whether stiffening of the infarct, as could for instance occur within hours after infarction due to oedema^[59], would significantly influence results. Finally, contractile stress perpendicular to the fiber direction may be necessary to accurately simulate cardiac deformation^[144]. To take this into account, we reran the LV model incorporating 20% active cross-fiber contraction: $\sigma = \sigma_p + w_a \sigma_a (\vec{e}_f \vec{e}_f + 0.2(\vec{e}_n \vec{e}_n + \vec{e}_s \vec{e}_s))$ ^[17]. Each variation was applied to all 4 versions of the standard model (A, CE, M, LE).

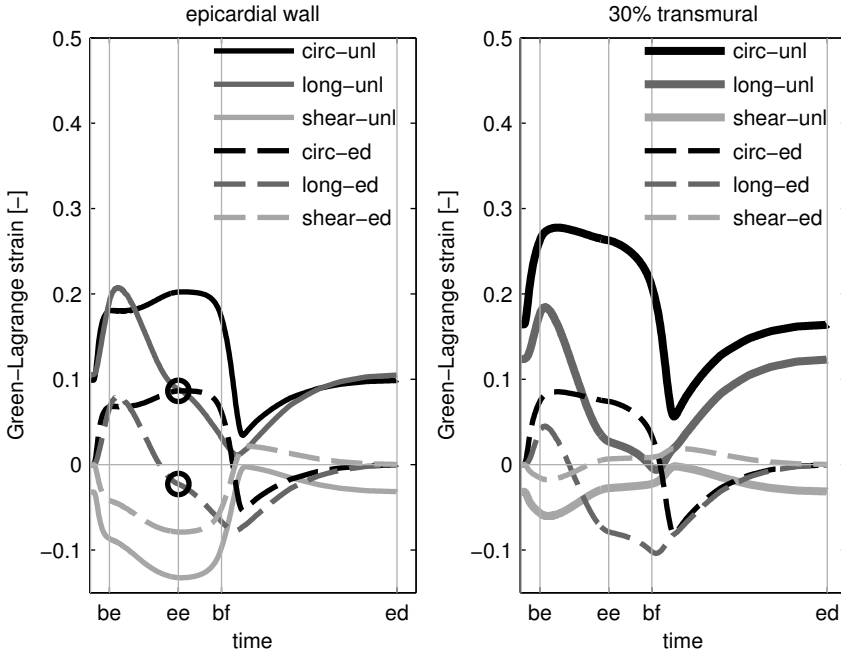


Fig. 5.3: Strain for round infarct located at mid-ventricle at epicardial wall (*left*) and at 30% transmural depth closer to endocardium (*right*). Strain is plotted with respect to the unloaded state (unl, solid line) and with respect to end diastole (ed, dashed line). Strain in circumferential (circ) and longitudinal (long) direction as well as circumferential-longitudinal shear (shear) are shown. The phases of the cardiac cycle are indicated: begin ejection (be), end ejection (ee), begin filling (bf) and end diastole (ed). The strain values that are compared to literature^[41] are indicated by a circle (*left graph*), while the strains that are used to calculate the predicted stress fiber distribution are marked with thicker lines (solid lines in *right graph*).

5.3 RESULTS

Strain comparison

An example of strain during the cardiac cycle (Fig. 5.3) shows that calculated strain in the infarct changes during the cardiac cycle, differs between locations (epicardial wall and 30% transmural depth closer to the endocardium), and depends on choice of reference configuration (unloaded or end diastole). The strain at end systole with respect to end diastole (marked with a circle in Fig. 5.3) as given by Fomovsky et al.^[41] does not incorporate the complete cyclic deformation; end diastole and end systole are not the points in time with minimal and maximal strain.

An overview of strain at end systole with respect to end diastole for all standard simulations compared to experimental data reported by Fomovsky et al.^[41] is given in Fig. 5.4. For the apex in longitudinal direction and for the mid-ventricle, simulated strains are within or close to a standard deviation of the experimentally observed

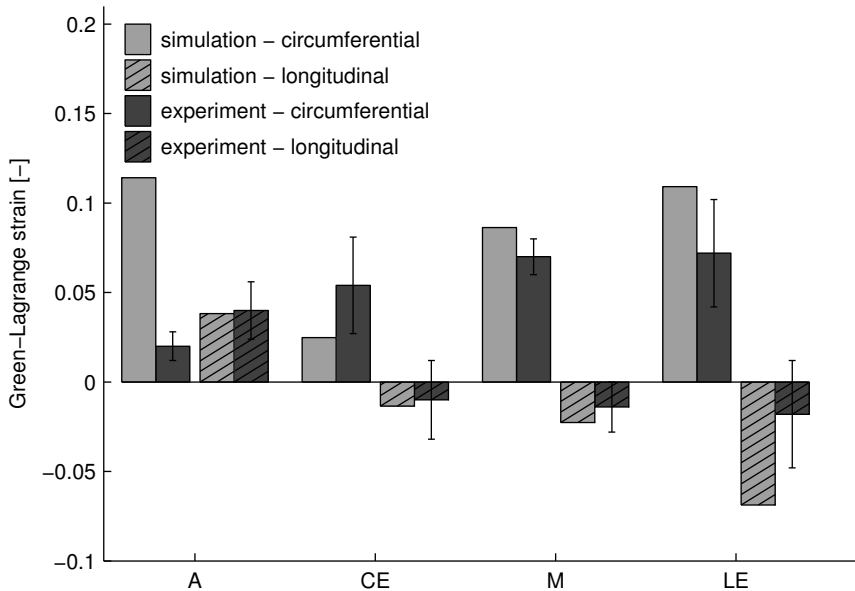


Fig. 5.4: Comparison of strains in simulations to the strains including standard deviations reported by Fomovsky et al.^[41]. End-systolic with respect to end-diastolic strain is given in circumferential (C) and longitudinal (L) direction for round infarct at apex (A), circumferentially oriented infarct at mid-ventricle (CE), round infarct at mid-ventricle (M) and longitudinally oriented infarct at mid-ventricle (LE).

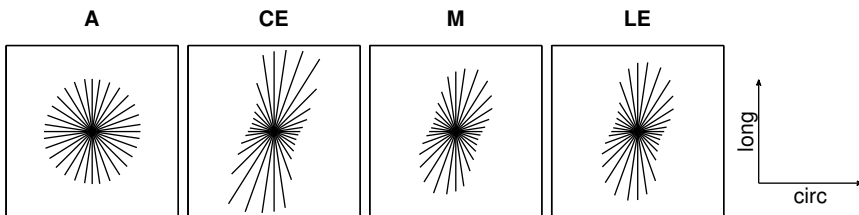


Fig. 5.5: Predicted stress fiber distribution for all infarct shapes and locations (round at apex (A) and circumferentially oriented (CE), round (M) and longitudinally oriented (LE) at mid-ventricle).

mean. Strain in circumferential direction at the apex is overestimated by the simulations.

Predicted stress fiber distribution

The predicted stress fiber orientations showed almost no preferred orientation in the apical infarct and a preference for the longitudinal direction in all the mid-ventricular infarcts (Fig. 5.5).

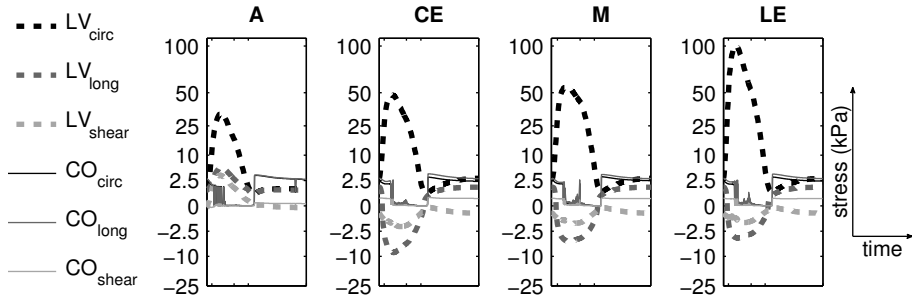


Fig. 5.6: Calculated stress in circumferential and longitudinal direction as well as circumferential-longitudinal shear stress during a cardiac cycle for all infarct shapes and locations (round at apex (A) and circumferentially oriented (CE), round (M) and longitudinally oriented (LE) at mid-ventricle) in left ventricle model (LV) and cell orientation model (CO). NB: a quadratic scale is used on the y-axis.

Stress in LV and cell orientation models

Stress varied during the cardiac cycle in both the LV and the fibroblast cell orientation model (Fig. 5.6). During the filling phase, the last part of the cycle in Fig. 5.6, stress in both models is of the same order of magnitude and fibroblast stress exceeds LV model stress in some cases. During systole however, stress in circumferential direction is much higher in the LV model than in the fibroblast cell orientation model: maximal stress is 25–100 kPa in the LV model versus 2.5 kPa in the cell orientation model. In longitudinal and in shear direction, differences are less consistent during the systolic phase, but in general LV stress magnitude clearly exceeds fibroblast stress magnitude.

Transmural variation

Strain varies with transmural position, which causes differences in preferred stress fiber orientation (Fig. 5.7): the preferred orientation changes from halfway between circumferential and longitudinal (mid-ventricular infarcts) or random (apical infarct) at the epicardium to longitudinal at the endocardium. Preferred orientation is less pronounced for the apical infarct than for the mid-ventricular infarcts. The amount of fibers in the circumferential-longitudinal plane reduces from epicardium towards endocardium. Infarct shape has little influence on the calculated stress fiber distribution. Preferred alignment in circumferential direction is never observed for mid-ventrically located infarcts.

Points around center node

When comparing the end-systolic with respect to end-diastolic strain for the 9 nodes on the epicardial wall closest to the infarct center, large differences were found (Fig. 5.8). For infarcts at the mid-ventricle, circumferential extension is highest in the middle column of the infarct (bar 2, 5, 8), while longitudinal shortening is relatively small in the middle row of the infarct (bar 4–6). Predicted stress fiber distributions at 30% transmural depth of the 9 nodes closest to the infarct center is relatively constant compared

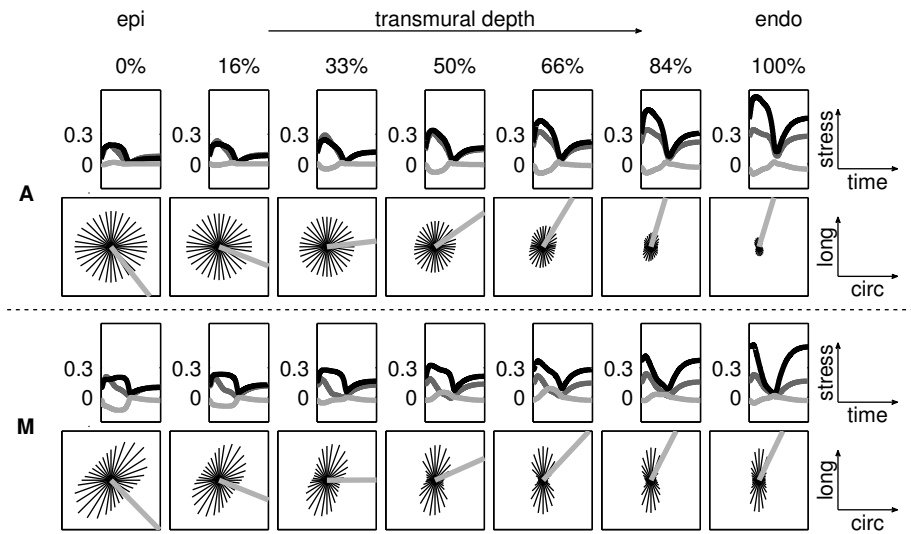


Fig. 5.7: Strain (*first and third row*) and predicted stress fiber distribution (*second and fourth row*) at different depth in simulations with infarct at apex (*top two rows*) and round infarct at mid-ventricle (*bottom two rows*). Gray lines in stress fiber distribution plots denote original local muscle fiber orientation. Colors in strain plots correspond to colors in Fig. 5.3 .

to the differences in strain at the epicardial wall. For the mid-ventricular infarcts the main stress fiber orientation is in longitudinal direction in most cases and it is always closer to the longitudinal than the circumferential direction. For the apical infarct the preferred direction is less pronounced. If a preference was found, it is for the longitudinal direction.

Excluding strain rate dependence on stress fiber orientation

When stress fiber development is only influenced by strain rate and not by strain, preferred orientations are much less pronounced. However, for the infarcts located at the mid-ventricle any preference remaining is for the longitudinal direction (Fig. 5.10).

Increased passive stiffness and active cross-fiber contraction

With both increased passive stiffness and active contraction perpendicular to the fiber direction, end-systolic strains on the epicardial wall at the infarct center (Fig. 5.11) are in general comparable to the corresponding strains in the standard simulations (Fig. 5.4) and in literature^[41]. Compared to the standard simulation, strain in circumferential direction is slightly increased. For most infarcts, this increases the difference between simulated and experimental strain in circumferential direction. With respect to the preferred stress fiber orientation (Fig. 5.12), in both increased passive stiffness and active cross-fiber contraction there is no clear preferred orientation for the apical infarct and a preference for the longitudinal direction for the mid-ventrically located

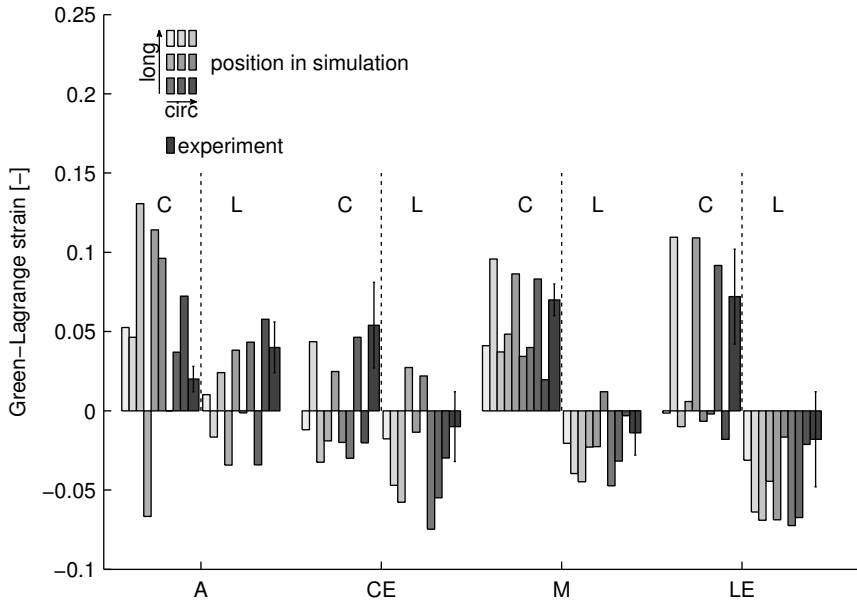


Fig. 5.8: Histogram showing circumferential (C) and longitudinal (L) end-systolic with respect to end-diastolic strain for infarcts of all shapes and locations (round at apex (A) and circumferential oriented (CE), round (M) and longitudinally oriented (LE) at mid-ventricle). Experimentally observed^[41] strain is also indicated. Colors denote different positions with respect to infarct center as indicated in grid in top left corner denoted position, where the horizontal and vertical directions in the grid correspond to circumferential and longitudinal direction respectively in the positions. In general, the indicated points lie just within the region where active contractility (w_a) is zero.

infarcts. This was also the case in the standard simulations. The predicted amount of stress fibers in the circumferential-longitudinal plane at 30% transmural depth is increased with increased passive stiffness.

5.4 DISCUSSION

Our results show that, when driven by deformation, fibroblasts are expected to prefer orienting in the longitudinal direction rather than the circumferential direction in infarcts located at the mid-ventricle, while no preferred orientation is expected for infarcts located at the apex. Although our modeling approach has limitations, we do not believe these limitations are the cause of the observed orientations. The healthy left ventricle model has been validated and the calculated end-systolic with respect to end-diastolic strain is similar to strain observed by Fomovsky et al.^[41]. This gives confidence to the calculated deformation. Because this comparison did not include deformation at all points in time, minor inaccuracies in deformation may occur. These are not expected to have a significant influence on the outcome of predicted cell orientation, in part because the predicted cell orientation is consistent for all mid-ventricular

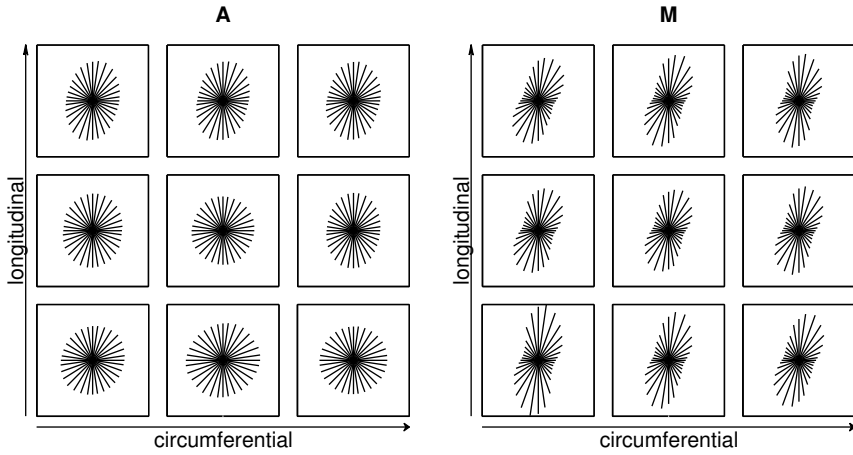


Fig. 5.9: Predicted stress fiber distribution at 30% transmural depth for the 9 nodes closest to the infarct center, for both apical infarct and round mid-ventricular infarct. Infarct center is at the center of each 3x3 grid.

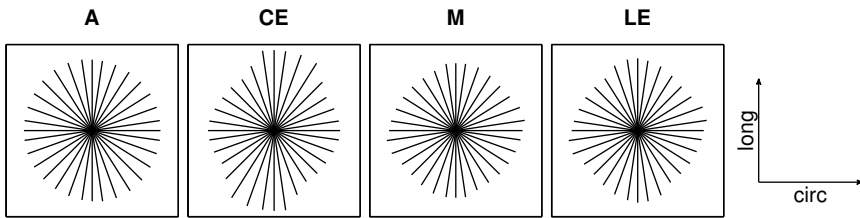


Fig. 5.10: Predicted stress fiber distribution when stress fiber developments depends on strain rate, but not on strain for nodes at 30% transmural thickness closer to the endocardium in line with infarct center node. All infarct shapes and locations (round at apex (A) and circumferential oriented (CE), round (M) and longitudinally oriented (LE) at mid-ventricle) tested for the standard model are shown.

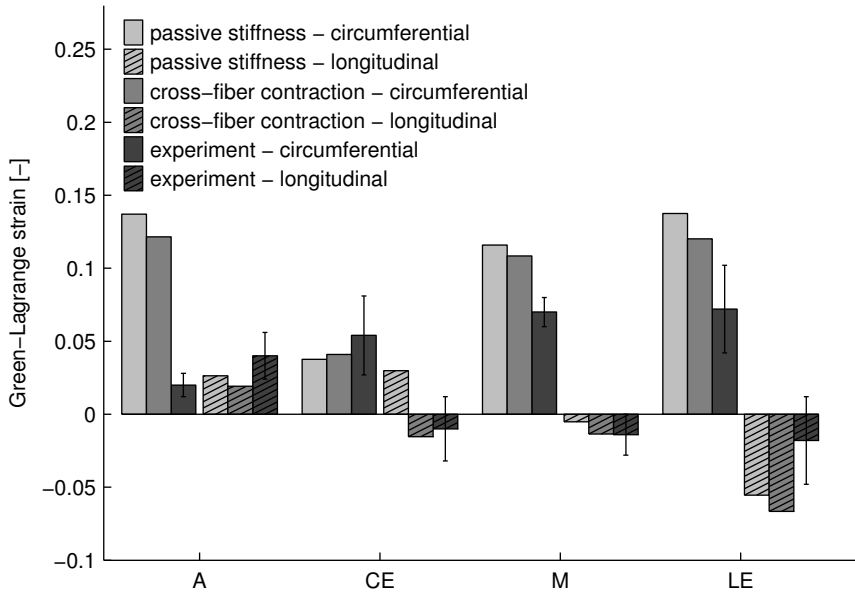


Fig. 5.11: Strains in the simulations with increased passive stiffness or cross-fiber contraction. Experimentally observed strains including standard deviations^[41] are shown for comparison. End-systolic with respect to end-diastolic strain is given in circumferential (C) and longitudinal (L) direction for round infarct at apex (A), circumferentially oriented infarct at mid-ventricle (CE), round infarct at mid-ventricle (M) and longitudinally oriented infarct at mid-ventricle (LE).

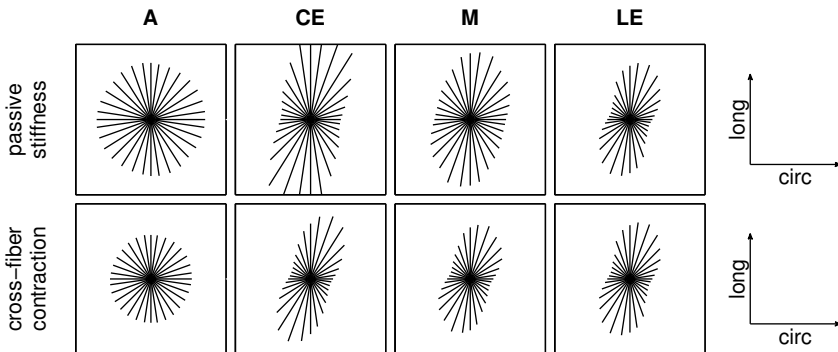


Fig. 5.12: Predicted stress fiber distribution for the simulations with increased passive stiffness or cross-fiber contraction for all infarct shapes and locations (round at apex (A) and circumferentially oriented (CE), round (M) and longitudinally oriented (LE) at mid-ventricle).

infarct simulations, even when end-systolic with respect to end-diastolic strain differs. In our modeling approach, cells are assumed to deform along with the infarcted material. This is the case if the cells are added in parallel to the cardiac tissue and they have a much smaller stiffness than their surroundings. In that case, they do not significantly influence the combined mechanical properties. In reality, cells may mechanically interact with their local environment. They may increase local stiffness and thus reduce deformation due to external loading, possibly in an anisotropic fashion. Furthermore, fibroblasts may actively contract and apply a load causing deformation in addition to the deformation caused by cardiomyocyte contractility. These effects are not taken into account. Our current focus is on the influence of the local mechanical environment on cellular orientation. As described in our cell orientation model, a preferred stress fiber orientation develops based on differences between directions in cyclic strain or in sensed resistance to deformation, with both mechanisms competing against each other. In the heart, circumferential and longitudinal direction are not expected to significantly differ in resistance to deformation, as the shape and internal pressure of the heart resist deformation in both directions. Therefore, differences in cyclic strain are expected to be the major determinant of mechanics-based stress fiber orientation in the heart. While cell deformation may differ from myocardial deformation, as indicated previously, the direction of largest cyclic strain is not expected to be influenced unless the cell becomes extremely anisotropic. This is only likely to occur after stress fibers are formed, and would then strengthen the orientation already present. Thus, differences between cellular and cardiac deformation are not expected to cause a different preferred stress fiber orientation. Our cell orientation model accurately describes the strain avoidance response observed for fibroblasts under in vitro loading^[103] when cells are free to change their orientation. Therefore it is expected to accurately predict cell orientation in the infarcted heart, if this orientation is mainly determined by the local cellular mechanical environment. However, our model assumptions lead to different results than the mechanisms in the model by Fomovsky et al.^[41] and Rouillard and Holmes^[118]. Collagen orientation based on the cell orientation predicted by our model, does not agree with the collagen orientation observed experimentally by Fomovsky et al.^[41]. Because our cell orientation model was based on mechanisms observed in vitro, this indicates these in vitro results cannot be translated to the infarcted heart. In the next section, we will provide an overview of reports on the deformation and orientation in the infarcted heart. This will aid in understanding the cellular environment in an infarcted heart and determining a hypothesis on cell orientation in the infarcted heart that is consistent with in vitro cellular behavior.

Comparison to literature

Some groups have described the deformation of acutely ischemic regions^[6,57,77,143], other groups described collagen orientation in infarcted myocardial tissue^[58,105,156,157], and sometimes both deformation and collagen orientation are given^[38,41,170]. When the left anterior descending coronary artery (LAD) is occluded, an anterior-apical infarct develops^[38]. This leads positive strains in circumferential and longitudinal direction that are comparable in magnitude, as observed by Fomovsky et al.^[41] for apical infarcts, in rats (Fomovsky and Holmes^[38]; epicardial) and in dogs^[143]. Deformations were less consistent when occluding (one or more branches of) the left

circumflex coronary artery (LCX), which leads to a non-apical infarct^[41]. Longitudinal strain was negative and lower than circumferential strain in pigs^[57] and sheep^[77]. In contrast, Zimmerman et al.^[170] investigated deformation in acutely ischemic pigs (5 min after infarction) and found a positive strain in longitudinal direction, which was larger than circumferential strain. Their results are of special interest because collagen orientation three weeks after infarction was also measured as was the influence of changing deformation by creating a slit. They reported that collagen orientation three weeks after infarct creation depended on transmural position and was oblique towards the apex (negative angle) in the epicardium, near circumferential (0°) at the midwall and oblique towards the base (positive angle) at the endocardium. When a slit was created next to the infarcted region by incising the endocardium in longitudinal direction directly after infarct creation, circumferential strain became negative. Main collagen orientation did not differ significantly from collagen orientation without slit at any transmural depth, though the angular deviation around the orientation was significantly increased. This indicates that the pre-infarct collagen orientation plays a larger role in determining final collagen orientation than infarct deformation, at least in this pig model of an LCX infarct. A similar collagen orientation with transmural gradient (-51° at 15% depth to 11° at 75%, most collagen fibers within 30° of circumferential orientation) was found for pigs with three week old scars by Holmes et al.^[58]. These results are consistent with the mid-ventricular infarct observed by Fomovsky et al.^[41]. With a LAD infarct, a random orientation was found in rats after one to six weeks^[38], consistent with the apical infarct observed by Fomovsky et al.^[41]. Omens et al.^[105] determined a preferred collagen orientation in rats two weeks after infarction, though the standard deviation was high, and observed that the healthy transmural gradient in collagen orientation tended to disappear (-14° at 21% and -28° at 66% transmural depth). Whittaker et al.^[156] also observed a preferred orientation with reduced transmural gradient in dogs six weeks after infarction (subepicardium: $-14.0 \pm 3.5^\circ$; midmyocardium: $1.4 \pm 0.4^\circ$; subendocardium: $12.7 \pm 2.1^\circ$). As collagen alignment was present in this case, collagen orientation may be species-dependent. Though healing after infarction undergoes several phases — cardiomyocyte death and inflammatory phases, during which ECM degradation starts, followed by granulation tissue formation and remodeling^[10] — no consistent relationship between collagen orientation and time after infarction is observed in literature.

Proposed mechanism

The limited and sometimes inconsistent data available prevent us from drawing definite conclusions on the mechanism determining collagen and cell orientation in the infarcted heart. The collagen orientation for mid-ventricular LCX infarcts is fairly consistent, but the deformation is not. Because of this, Fomovsky et al.^[41] have interpreted the orientation as a strain alignment response, while Zimmerman et al.^[170] have interpreted it as an influence of the pre-infarct collagen orientation. For apical LAD infarcts, deformation is fairly consistent, but collagen orientation shows more variation. An approximately random orientation and equibiaxial strain was found for rats, which can be interpreted as both strain avoidance and strain alignment. Based on the deformation and orientation results described above, collagen orientation in the infarcted myocardium mostly follows the same basic transmural gradient as is observed

for collagen and cardiomyocytes in healthy cardiac tissue^[104,131], though modifications to the pre-infarct collagen orientation occur, especially in the apical region. A preferred alignment of cells in strained direction, as modeled by Fomovsky et al.^[41] and Rouillard and Holmes^[118] agrees well with their experimental data. However, there is room for reasonable doubt, because fibroblasts do not show a preferred alignment in strained direction during in vitro experiments^[42,50,66]. Also, a strain alignment mechanism is inconsistent with the work by Zimmerman et al.^[170]

In vitro, fibroblasts tend to align themselves and their collagen matrix perpendicular to strain if possible^[42,66]. In the infarcted heart this strain avoidance may not be possible. The overall collagen orientation can be changed by synthesis and degradation^[101] and by cells applying traction forces to the collagen to change its orientation^[51,129]. If a high, external, loading is applied to collagen fibers, the cells may not be able to develop enough force to change the orientation of the collagen fibers. This may occur in the infarcted heart, as our simulations indicated that stress in circumferential direction in the LV model is periodically much higher than the active cell stress produced by the fibroblast in mid-ventrically located infarcts. Furthermore, collagen is known to degrade in a strain-dependent manner, with strained collagen being less susceptible to degradation^[162]. In the infarcted heart, this may protect strained fibers, such as collagen fibers oriented in circumferential direction in mid-ventrically located infarcts, from degradation, allowing cells and collagen to orient in strained direction. This effect may be of special importance during the first days after infarction, when degradation of the pre-existing matrix occurs^[141]. We thus propose that the pre-infarct collagen orientation is used as scaffold to produce the scar collagen orientation in a loading-dependent manner, with high loading providing resistance to fibroblast-based remodeling, thus increasing the importance of the initial collagen orientation. This implies that in rat apical infarcts, where limited or no preferred orientation is observed, either loading is small enough for fibroblast-based remodeling, or there are initially enough fibers and there is enough load in all direction to obtain a random orientation. All in all, according to our proposed mechanism, there are two regimes determining cell and collagen orientation in tissues: a cell-based strain avoidance mechanism at low loading and a collagen-based mechanism at high loading, where fibers in strained directions are not reoriented and cells co-align with collagen according to contact guidance.

Implications

Our hypothesis that cells and collagen avoid strain at low loads due to collagen co-aligning with strain avoiding cells, while cells and collagen align in directions of high stress or strain at high loads due to co-alignment of cells with collagen that they are unable to reorient, has important implications both for future experiments and clinical applications. In current in vitro experiments, a change of cell and collagen orientation towards the cyclically strained direction is not observed, though collagen fibers in the core of experimental tissues do not always orient away from cyclic strain^[42,66]. We hypothesize that the amount of loading and initial structure are critical, and propose investigating cell and collagen alignment in random and aligned constructs experiencing limited loading, as well as the kind of high cyclic loading that is representative for the heart. It may be necessary to reduce loading in engineered constructs, e.g. by

applying cyclic compression instead of extension, to allow a cell and collagen reorientation response. A cardiac-like combination of internal pressure and cyclic extension may be of special importance, as this can lead to an oppositely signed stress and strain in materials of limited compressibility and indicate the relative importance of stress and strain on the orientation response. Investigating the influence of the duration of loading, and of the relative amounts of cells and collagen is also expected to be important. If the ability of cells to change the orientation of highly loaded collagen fibers is indeed low, it may require a lot of time to change an initial structure, if possible.

In vivo, conclusive data on the relative influence of initial collagen orientation and deformation on collagen orientation are required. An important step in this direction can be made by modifying infarct deformation in a controlled manner, e.g. by using an anisotropic reinforcement to the heart as was done by Fomovsky et al.^[40]. Measuring strain at different transmural depths throughout the cardiac cycle and at different time points after infarction, as well as measuring the collagen structure and cell orientation at different transmural depths and time points after infarction will then provide essential data. Doing this for both apical and mid-ventricular infarcts and possibly different animals may show whether there are inherent differences between these situations.

If the collagen structure that develops in the infarcted area depends on the loading intensity as hypothesized, this has important clinical implications for the use of left ventricular assist devices (LVAD's). These devices unload the heart, and are therefore, based on our hypothesis, expected to allow fibroblasts more freedom to remodel collagen in a strain avoiding manner. Collagen orientation may thus develop an opposite orientation in normally loaded and LVAD unloaded hearts, which is important when designing a therapy, especially if it aims at obtaining anisotropic material properties. To our knowledge the collagen orientation in LVAD assisted infarcted tissue has not been investigated yet, and we believe this would provide valuable knowledge on the mechanism underlying collagen and cell orientation in the infarcted heart.

5.5 CONCLUSION

Based on our results, we suggest that the collagen orientation in infarcted hearts is not caused by a co-alignment of collagen with fibroblasts that orient based on deformation. Instead, we hypothesize that in the infarcted heart, fibroblasts are not able to change the orientation of highly loaded collagen, so the fibroblasts align with collagen instead of reorienting it. This implies cells and collagen orient differently depending on the intensity of the load they experience, and the initial collagen orientation is of special importance under high loading.

APPENDIX

Active stress in the basic unit of the muscle fiber, the sarcomere, is modelled via a contractile element in series with an elastic element (stiffness: E_a). Active stress depends on time elapsed since activation t_a , total sarcomere length l_s and contractile element length l_c and is defined as^[17]:

$$\sigma_a = \frac{l_s}{l_{s0}} f_{iso}(l_c) f_{twitch}(t_a, l_s) E_a (l_s - l_c) \quad (5.14)$$

where f_{iso} and f_{twitch} describe the length and time dependence of the active stress. These are defined as:

$$f_{iso}(l_c) = \begin{cases} T_0 \tanh^2(a_l(l_c - l_{c0})) & \text{if } l_c \geq l_{c0} \\ 0 & \text{if } l_c < l_{c0} \end{cases} \quad (5.15)$$

$$f_{twitch}(t_a, l_s) = \begin{cases} 0 & \text{if } 0 > t_a \\ \tanh^2\left(\frac{t_a}{\tau_r}\right) \tanh^2\left(\frac{t_{max}-t_a}{\tau_d}\right) & \text{if } 0 \leq t_a \leq t_{max} \\ 0 & \text{if } t_a > t_{max} \end{cases} \quad (5.16)$$

with $t_{max} = b(l_s - l_d)$ the duration of the twitch. Contractile element length changes in time according to:

$$\frac{dl_c}{dt} = (E_a(l_s - l_c) - 1)v_0. \quad (5.17)$$

For each model parameter a description and the used value are given in Table 5.5. All nodes in the model were simultaneously activated following Kerckhoffs et al.^[72], at intervals of 800 ms, the simulated duration of one cardiac cycle.

Table 5.5: Active material parameters^[17].

parameter	meaning	value	unit
l_{s0}	sarcomere length in stress-free state	1.9	μm
E_a	stiffness series elastic element	20	μm^{-1}
T_0	reference active stress	160	kPa
a_l	increase in active stress with contractile element length	2	μm
l_{c0}	contractile element length below which active stress is zero	1.5	μm
τ_r	rise time active stress	75	ms
τ_d	decay time active stress	150	ms
b	increase in twitch duration with sarcomere length	160	$\text{ms } \mu\text{m}^{-1}$
l_d	(extrapolated) sarcomere length where twitch duration is zero	-0.5	μm
v_0	unloaded sarcomere shortening velocity	0.0075	$\mu\text{m s}^{-1}$

Chapter 6

General discussion

6.1 INTRODUCTION

Over the last decades, an increasing number of patients experiencing a myocardial infarction have survived the initial attack. These patients have healing or healed infarcts^[10,59]. Healing may be beneficial initially^[59], but, on the long term, detrimental remodeling may occur, leading to heart failure^[43,65,68]. Developing treatments for MI patients that prevent detrimental remodeling is therefore important. Such a treatment could be based on injecting microtissues: small tissue-like constructs, consisting of cells embedded in a biomaterial. The role of the cells is to improve cardiac function by restoring contractile functionality, while the biomaterial mechanically supports the heart and provides a suitable environment for the cells. In this thesis, I have investigated various aspects of such an approach via computational modeling. I have concentrated on the mechanical environment in the heart — including to what extent this can be controlled via a microtissue — in relation to cellular behavior, specifically cellular orientation. As part of the mechanical environment both passive inputs (e.g. stiffness) that can only lead to cellular behavior when cells actively sense their environment, and active inputs (e.g. applied deformation) that influence cells whether or not the cell is actively sensing, were taken into account. The results of this work have implications for microtissue-based cardiac regeneration. Furthermore, the model that is developed to describe active cellular mechanosensing and cellular orientation in response to a mechanical environment is generic and applicable to investigate and/or predict how cells orient during tissue engineering, for example. In this chapter, I will discuss the main findings of this thesis, the benefits and limitations of the models used, and the implications of the results for both microtissue-based cardiac repair and (the modeling of) how cells sense and respond to their local environment in general, as well as interesting directions for future research.

6.2 MAIN FINDINGS

Limited control over microtissue mechanical environment via stiffness

When a microtissue containing cells is embedded in the heart, the cells are expected to influence macroscale mechanics, e.g. by cellular contraction. How the cells behave is affected by their mechanical environment. The mechanical environment is determined in part by (passive) microtissue properties, such as local stiffness, which can be sensed by the cells. However, the macroscale mechanical environment will also influence the local mechanical environment inside the microtissue. Specifically, active cyclic cardiac deformation will lead to deformation of a microtissue embedded in the heart. The magnitude of this deformation depends on the material properties of both microtissue and environment. The deformation in the microtissue can likely be controlled by varying microtissue stiffness. In Chapter 2, it was investigated to what extent strain in the microtissue can be controlled by changing microtissue stiffness. A computational model representing a spherical microtissue embedded in a deforming environment was used to assess the influence of microtissue stiffness on microtissue strain. The strain applied to the macro-environment was constant. Reducing microtissue stiffness increased the strain in the microtissue. This shows that some control over microtissue deformation via microtissue stiffness is possible. However, the maximal

average strain obtained in the microtissue, for a microtissue stiffness of less than 0.01 times the environmental stiffness, was only 2.5 times the deformation applied to the environment. Thus, there is a limited range within which control over strain, relative to the strain in the surrounding tissue, is possible. Furthermore, the strain in the microtissue was heterogeneous. The amount of heterogeneity depended strongly on the contact definition between microtissue and environment. Heterogeneity was limited if the microtissue was fixed to the environment in both normal and shear direction, while heterogeneity was much larger if the microtissue was fixed to the environment in normal direction, while frictionless sliding was allowed in shear direction. This heterogeneity further limits the range within which microtissue strain can be controlled.

Model describing cellular mechanosensing and response via stress fibers

To understand and predict the outcome of a therapy for myocardial infarction involving microtissues, it is essential to understand and predict how the cells in the microtissue will respond to their local environment. In Chapter 3, a computational model was developed to describe an important aspect of cellular behavior: the synthesis and degradation of actin stress fibers, depending on the stress that is actively sensed with these fibers. This mechanism is expected to be similar for various adhering cell types. Therefore, the model was not based on a specific cell type, but on adhering cells in general. Because actin stress fibers have a molecular motor unit that is similar to muscle fibers, stress fiber stress in the model was defined comparable to muscle force in Hill's muscle model. The stress in stress fibers in a certain direction depended on their strain and strain rate. Increased strain magnitude and shortening rate reduced fiber stress. This stress had a critical influence on the stress fiber distribution that developed in the model, because stress fibers were mainly synthesized in directions of high stress. A generally applicable model should be able to describe the stress fiber distribution in response to any mechanical environment. Therefore, the model was tested against a range of stress fiber orientation responses described in literature. This included stress fibers preferably orienting perpendicular to cyclic strain when resistance to deformation in this direction was large, but in strained direction when resistance to deformation perpendicular to cyclic strain was small. For all situations tested, the model accurately described the experimentally observed trends in stress fiber distribution.

Model quantitatively describes cell orientation in small tissues

To more rigorously test the model, a quantitative validation was performed using 3D small scale tissues (Chapter 4). Cells were cultured in such tissues that were either constrained uniaxially or biaxially. Local stress fiber orientation in these tissues was determined. This situation was simulated with the model described previously, and stress fiber orientation was determined in the same regions as those studied experimentally. In both experiment and simulation, stress fibers mainly developed in directions in which resistance to deformation was high. In the center of biaxially constrained tissues, resistance was high in all directions and a random orientation was observed. In uniaxially constrained tissues and near the edge of the tissue, on the other hand, resistance to deformation perpendicular to the free edge or constraint was reduced, leading to a preferred alignment in constrained direction and parallel to the edge. Quantitative

comparison of experimental and simulated stress fiber distributions in general showed good agreement. This further increases confidence in the model.

Collagen in infarct does not co-align with cells that orient in response to mechanics

After validation, the stress fiber orientation model was applied to the infarcted heart (Chapter 5). Stress fiber orientation was predicted and compared to an experimentally observed collagen orientation^[41] for infarcts at different locations (apex and mid-ventricle) and of different shapes. This was done to determine whether the observed collagen orientation was caused by collagen co-aligning with cellular stress fibers, orienting in response to their mechanical environment. Deformation in the infarcted heart was estimated with a previously developed model of the left ventricle^[17]. This deformation was similar to the deformation of the infarcts for which collagen orientation was determined. This cyclic deformation was applied to the stress fiber orientation model. The calculated stress fiber orientation was random for an apical infarct, as was observed experimentally. For mid-ventricular infarcts with different shapes, the model predicted a preference for the longitudinal direction, while a circumferential collagen orientation was observed experimentally. This indicates that, assuming cellular deformation is similar to the macroscale deformation of the infarcted tissue, the collagen orientation observed experimentally is not due to collagen co-aligning with cells and their stress fibers that orient in response to their mechanical environment.

6.3 MODELS

All of the modeling approaches described in this thesis have benefits and limitations, which are discussed below. A comparison to relevant models described in literature is also given.

Interaction between microtissue and environment

The model used to describe the mechanical interaction between macro-environment and microtissue (Chapter 2) has several limitations. For instance, no active contractility is included in the environment, which makes it only suitable for infarcted tissue in which no contractility is left. In addition, visco-elasticity of the microtissue is not included. Also, the geometry of both microtissue and environment are schematic and the microtissue is assumed to exactly replace part of the environmental tissue, without initial stress or strain in microtissue or environment. Furthermore, the applied displacement was much simpler than the complex and time-dependent loading of the actual heart. It is therefore clear that the current model cannot be used to determine the precise mechanical environment experienced by cells in a microtissue. This is acceptable, however, because our aim was not to determine a precise mechanical environment, but to better understand the interaction between macro-environment and microtissue and to determine the level of control over microtissue strain that is possible via microtissue stiffness. The model is sufficient to answer these questions, when focusing on the additional deformation of the microtissue, due to the cyclic deformation of the infarcted environment. Visco-elasticity and initial stresses or strains may influence average strain, but a large influence on the cyclic strain magnitude due to cyclic environmental strain is not expected. Because deformation results were taken

relative to the deformation applied to the environment, changes in environmental deformation do not significantly influence results. A similar reasoning holds for microtissue and environmental stiffness: by investigating deformation as function of the ratio between microtissue and environmental stiffness, the influence of uncertainties in environmental stiffness is minimized. By investigating two extreme cases for the contact between microtissue and environment, a realistic deformation result is expected to lie in between the two extremes tested.

Stress fiber-based cell orientation model

Whether or not the use of microtissues to regenerate the heart after myocardial infarction is successful, will depend among other factors on the behavior of the cells inside the microtissues. This behavior is influenced by the mechanical environment sensed by the cells. Therefore, a model was developed to describe how cells actively sense their environment with their actin stress fibers, and the resulting synthesis and degradation of these fibers (Chapter 3).

The combination of cells, including their stress fibers, and their substrate or surrounding matrix was modeled as a continuum. This greatly simplifies the model and is reasonable when relevant length scales are significantly larger than the dimensions of the microstructure^[93] as was the case in the work described in this thesis. With the current continuum assumption, the way the cells adhere to their environment was not explicitly simulated. Focal adhesions connect the stress fibers to the extracellular matrix, and are thus required for mechanosensing. In 2D culture, they are known to actively react to their mechanical environment by becoming larger when increased stress is applied to them^[121]. This effect is not taken into account in the current model. Furthermore, (collagen) contact guidance was not simulated. The precise mechanism leading to this preference of cells to orient parallel to oriented structures has not been elucidated. Mechanical effects, such as cells being able to develop more stress parallel to the matrix fibers, may play a role. To model such effects, single cell simulations are required. Modeling the stress fibers in a cell as a continuum may then be less applicable and discrete effects such as the location of adhesions may play a role, as well as the bending resistance of actin fibers. Still, the current model has been applied to provide increased insight on contact guidance in a single cell adhered to a fiber of a similar, μm , scale^[4].

In the model, actin stress fibers were the main cellular component modeled, and attention was focused on the active stress they generate. In reality, the actin cytoskeleton may also have a passive contribution to the mechanical properties of the cell. Furthermore, other components than actin may play a role in determining the mechanical properties of a cell. These effects were lumped, by incorporating an exponential passive stress-strain curve for actin fibers in extension, and a neo-Hookean material representing not only cellular components other than actin, but also the stiffness of the local environment of the cell. This is a limitation when cellular mechanical properties are not dominated by actin-myosin contractility, such as in non-adhering cells.

Actin-myosin contractility was simulated with a Hill muscle model, as actin stress fibers and muscle fibers have a similar structure. However, behavior of stress fiber and muscle sarcomeres is not completely the same^[20]. Further refinement of the relationship between stress fiber deformation and active contractile stress may thus be

needed. Comparison of the deformation of microposts constraining a microtissue in experiment and simulation showed qualitative agreement and a similar order of magnitude (Chapter 4), providing confidence in the force predicted by the model.

Increased active stress in a direction was simulated to lead to an increased synthesis of stress fibers in the same direction. In general, this assumption agrees well with reality. However, increased degradation under low stress, as assumed by Deshpande et al.^[29] may lead to similar results. The model can easily be modified to incorporate this, if necessary.

The stress definition in combination with a preferred stress fiber alignment in directions with high stress leads to an asymmetric strain avoidance response during cyclic strain: cells will orient away from the strained direction more strongly during the shortening than during the lengthening part of the cycle. Therefore, the calculated stress fiber distribution not only depends on strain amplitude and frequency, but it may also depend on asymmetry of the waveform. Tondon et al.^[137] investigated various asymmetric waveforms, and found that cells responded more strongly to the rate of lengthening than to the rate of shortening. This seems to contradict with our model. However, as the total period of the waveform was kept constant, an increased rate of lengthening corresponded to a longer shortening period. In the model, an increased shortening period may have a larger strain avoiding effect than an increased shortening rate.

The modeled stress fibers have a constant reference length. In reality, actin stress fibers may change their reference length^[71] to maintain homeostasis in a changing environment. If such an effect was implemented in the current model by letting stress fibers adjust their reference length towards their current length, then in static conditions the reference length would be adjusted until it is equal to the current length. Therefore, in static equilibrium, stress fiber stress would always have the same maximal value, and cells would not orient in response to differences in substrate stiffness, which is unwanted. A consequence of the current implementation is, that stress fibers orient away from static extension and remain reoriented. If stress fibers can adjust their reference length, then any cellular response to static extension would be transient. To the best of my knowledge, stress fiber orientation under static strain in a biaxially constrained environment has not been studied yet. If cells can indeed adjust and do not reorient, the model should be modified to incorporate this effect.

Although improvements are still possible, in the cases studied, the model described in this thesis performed well. It can therefore accurately describe the development of a preferred stress fiber orientation in cell populations under static conditions — when a passive mechanical environment provides a certain, possibly anisotropic, resistance to deformation — and/or in dynamic conditions — when a cyclic deformation of certain amplitude and frequency provides a stimulus to the cells to orient away from the strained direction.

Left ventricle model combined with cell orientation model

The previously described stress fiber-based cell orientation model was applied to the infarcted heart, assuming a left ventricular infarction (Chapter 5). This was done by estimating the deformation of cells in the infarcted region via a model of the left ventricle^[17], and then applying this deformation to the cell orientation model. The healthy

left ventricle model was validated and the calculated deformations were similar to the deformation in the experiment that was simulated. However, this comparison was performed for a single deformation value, while the actual deformation was cyclic. Some minor differences may thus occur, but they are not expected to have a significant influence on the outcome of predicted cell orientation.

Cell deformation was assumed to equal the deformation of the infarcted material, as if the cells are parallel to the cardiac tissue and have a much smaller stiffness than their surroundings. However, mechanical interaction between cells and the infarcted tissue may occur. Local stiffness may increase due to the presence of the cells, and therefore deformation due to external loading may reduce. Cells may also actively contract and apply additional loading to the infarcted tissue, causing deformation. While cell deformation may differ from myocardial deformation, the direction of largest cyclic strain and thus the predicted cell orientation is not expected to be influenced unless the cell becomes extremely anisotropic.

Comparison to models in literature

INTERACTION BETWEEN MICROTISSUE AND ENVIRONMENT

Several researchers have simulated an infarcted heart to which a (bio)material was delivered^[39,76,145,154]. However, they all focussed on the influence of this material on macroscale parameters, such as stroke volume or myocardial wall stress. To the best of my knowledge, the local mechanical environment in the delivered material was not investigated previously.

CELL MODEL

Various mechanical models of the cell are described in literature. The cytoskeleton has been modeled as a strictly passive material using an open-cell foam approach without including cellular contractility, and as a stress-supported structure where a pre-existing tensile stress (prestress) is required to stabilize the structure^[127]. Active sensing of the mechanical environment is possible via the prestress^[27], but an active response to what is sensed is not yet incorporated in these models. When cells do not actively respond to their environment on the time scale investigated, this type of model may provide realistic cellular behavior. Furthermore, the passive behavior of the currently described actively contracting model may be improved using ideas from this type of models.

In contrast to passive cell material models, mechanoregulatory models include an active cellular response such as cell differentiation and proliferation^[18,130] or bone remodeling^[96], without an actively mechanosensing cytoskeleton. Such an approach is only valid if the mechanics of the environment dominate local cellular mechanics, which is not the case for contracting cells in a relatively soft environment, such as the engineered tissues described in this thesis. Also, a law determining cell behavior is required. The stress fiber-based cell orientation model described in this thesis may be able to increase understanding as to what such a law should be.

Force dipoles have been used as a course-grained approach to modeling cell contractility^[124]. The magnitude and orientation of this dipole can be adjusted by the cells to obtain an optimal stress or strain in the adjacent matrix while minimizing energy expenditure^[120]. This way of modeling is a powerful tool to qualitatively explain the

level and orientation of cell contractility that is optimal. However, the various analytical modeling approaches used to model different aspects of cellular contractility, limit the use as a general model for cell contractility in response to a possibly complex mechanical environment; a finite element implementation, as is used in the current thesis, is more suitable in this case.

Kaunas et al.^[71] simulated the reorientation in response to cyclic stretch of a discrete number of fibers. Because cytoskeletal force is incorporated in this model, mechanical interaction with the environment and active mechanosensing are possible in principle. However, the response to a passive mechanical stimulus (substrate stiffness) was not investigated. In contrast to this model, the stress fiber-based cell orientation model described in this thesis was validated with both active and passive mechanical stimuli and stress fibers were modeled as continuum, which is more computationally efficient for large amounts of fibers.

The cell model described in this thesis is based on and most similar to the models by Deshpande et al.^[29] and Vernerey and Farsad^[142]. In all of these models, the development of stress fibers in response to a mechanical environment is modeled and implemented in a finite element code via a continuum approach. The model by Vernerey and Farsad^[142] was formulated as a constraint mixture approach, including an isotropic passive cytoskeleton, fluid cytosol, and dissolved globular actin monomers, besides actin stress fibers. This makes it suitable when the flow of fluid and monomer in the cell is important. The response of this model in a dynamic environment has not been investigated, and based on the equations, the model cannot predict a strain rate-dependent strain avoidance response, unlike the cell model described in this thesis. The model by Deshpande et al.^[29] was applied to both a static and a dynamic environment^[153], but different parameters were required to obtain realistic results in both situation. The stress fiber model described in this thesis can simulate cell orientation in static and dynamic situations with a single parameter set. Additionally, a realistic response to a combination of both types of stimuli is obtained, and no external activation stimulus is required, unlike in the model by Deshpande et al.^[29].

CELL ORIENTATION IN INFARCTED HEART

Many models of the infarcted heart using finite element analysis have been described, with different assumptions and levels of complexity^[14,16,52,62,107,108,166]. These models were mainly used to understand how cardiac function is reduced in the infarcted heart, and which factors influence the reduction in function. To the extent of my knowledge, finite element models were not previously used to study the local mechanical environment in the heart and its influence on the behavior of cells present in or delivered to the heart. Fomovsky et al.^[41] did develop an agent-based model to describe cell orientation in the infarcted heart, assuming cells preferable oriented in (cyclically) strained direction. The outcome of their simulations agreed well with their experimental results, but the assumption of strain alignment does not agree with commonly observed cell behavior in vitro. Thus, while this modeling approach^[41] more accurately describes their experimental results than the modeling approach described in this thesis (Chapter 5), which is based on in vitro cell behavior, it does not explain in which situations the model is valid or why cells behave the way they do.

6.4 IMPLICATIONS AND FUTURE RESEARCH

The work presented in this thesis has implications and points towards interesting directions of further research for (the modeling of) cellular mechanosensing and -responding and for microtissue-based cardiac regeneration approaches.

Modeling how cells sense and respond to their environment

The stress fiber-based cell orientation model reported in this thesis (Chapter 3) describes several effects observed during *in vitro* experiments. This implies that the principles in the model are reasonable and thus that

- cells orient in directions in which they sense mechanical resistance in static situations
- cells orient away from dynamic strain and that this effect is more pronounced with increased strain amplitude and shortening velocity
- there is competition between both if both effects play a role.

Furthermore, the simulated stress fiber orientations corresponded to observed stress fiber orientations in small scale tissue constructs, indicating these principles are the main determinants of stress fiber orientation in these constructs, in which new tissue is formed.

The model describes cell behavior in a generic sense. It allows extension, e.g. to include collagen fibers and their remodeling^[85]. Collagen is the main load bearing protein in tissues. Therefore collagen production, degradation and reorientation strongly influence the tissue's mechanical properties. When the model is extended to include collagen remodeling by the cells, mechanical interaction between a collagenous tissue and its surroundings is possible. Cells then not only respond to their environment, but also influence it. This allows many phenomena related to tissue engineering to be described, such as the collagen fiber alignment in cruciform gels with different arm widths and in engineered vascular tissues^[85].

While the model accurately described many phenomena that are observed in *in vitro* studies, collagen orientation in the infarcted heart could not be predicted, indicating cell orientation is not determined by its local mechanical environment, as defined by the model, but by e.g. collagen contact guidance. In the future, the model should be extended to include this phenomenon, either by simulating the discrete geometry of cells and collagen fibers, if the model predicts contact guidance on this smaller length scale, or by incorporating an additional orientation stimulus to the cells.

Furthermore, dynamic simulations with realistic geometries currently require much computational time. Several time steps per cycle must be simulated, while the development of an orientation on a much larger time scale is of interest. Modifying the model to include an average effect of cyclic deformation and therefore allow larger time steps would greatly improve the practical usability of the model.

Other potential limitations to the model, such as a non-changing reference length, are expected to only be relevant in specific situations. I therefore propose they should only be addressed if relevant to the specific situation that is simulated.

Microtissue-based cardiac regeneration

Strain heterogeneity was observed in the microtissue (Chapter 2). This indicates that cells in different parts of a microtissue may feel different stimuli, and may thus respond in a different manner. Experimentally cells have been shown to, for example, change their orientation only if strain exceeds a certain magnitude^[12]. Heterogeneity may thus limit control over cellular behavior and should be limited, e.g. by adhering the microtissue to its environment.

Furthermore, to obtain a certain fold change in microtissue deformation relative to macroscale deformation, a much larger fold change in microtissue stiffness was required. Cells may respond to stiffness as well as strain. When stiffness is extremely low, local stiffness may have a larger influence on cellular behavior than local deformation. Attention was focused on microtissues with lower stiffness than their surroundings. This was done because the infarcted heart is thought to be stiff^[7], while a native stiffness might be more suitable for cellular behavior such as cardiomyocyte beating^[32]. However, the simulations with the infarcted left ventricle indicate a large cyclic deformation (>20%) may occur in the heart. If this is amplified inside a microtissue that is softer than its environment, it may damage the cells^[12]. Thus, it may not be beneficial to control cellular deformation by increasing it; it may be necessary to reduce cellular deformation. However, this requires stiff microtissues, that may not stimulate cells towards cardiac differentiation^[33]. Thus, our results imply cells will experience a non-physiologically high stiffness or strain. Future research may show which combination of stiffness and strain in the applicable range is most suitable for cardiac regeneration.

Besides stiffness and deformation, the structure of the environment surrounding a cell may be important (Chapter 5). In the infarcted heart, a preferred collagen orientation may guide cellular orientation. When cells are embedded in a microtissue, they may no longer sense the cardiac structure and may respond to a local structure in the microtissue, if present. Microtissues having a certain structure can likely be created if an anisotropic scaffold is used. However, if these are delivered to the heart via a catheter, control over the orientation of the microtissue with respect to the heart may not be possible. Larger structures, on the scale of the heart, may be necessary to control local anisotropy. Further experimental research is required to determine the relative influence of local stiffness, local deformation, cardiac structure and local structure stimuli on the different components of cellular behavior in microtissues and other approaches to cardiac regeneration involving cells and a biomaterial.

To improve understanding and rational design of cell-based cardiac regeneration in the future, a combination of in vivo experiments, in vitro experiments, and computational modeling is most promising. In vivo experiments are necessary to determine which factors are important and should be incorporated in an in vitro approach. If an in vitro model reflects cellular behavior in a microtissue, it can be used to vary various parameters and determine the relative influence of contributing factors. Once these aspects are known, they should be incorporated in the computational cell orientation model that is developed in this thesis. From this extended model, a multiscale model can be developed that not only takes into account the influence of the environment on cellular behavior, but also the influence of cellular behavior, such as collagen

remodeling and active contraction after differentiation, on cardiac mechanics. This will aid in determining the influence of parameter variations within a therapeutic approach, such as changing microtissue stiffness, and to compare different therapeutic approaches, such as injecting cells in microtissues versus injecting cells in an in situ gelling biomaterial.

Thus, while experimental evidence is essential, computational modeling may also play an important role when designing a new therapy for MI patients. A model is always a simplification of reality and when a model performs well, this indicates the hypotheses underlying the model are reasonable, improving understanding of the situation modeled. Once a validated model is developed, it can easily be used to determine the influence of various parameters, limiting experimental testing to the sets of parameters that are most promising based on computational results. Reducing the amount of experiments is of special importance in a biological setting, as it not only reduces costs, but also the amount of animal testing necessary. Such advantages of using a computational modeling approach are not only valid for therapies aiming at MI patients; computational modeling may also improve understanding and rational design of therapies for other (cardiac) diseases. Also, elements of a model for designing new therapies for MI patients may be used when modeling other situations, e.g. a macroscale heart model may also be applied to other cardiac diseases and a cell orientation model may be useful when simulating the in situ engineering of other tissues such as heart valves.

6.5 CONCLUSION

In this thesis, computational modeling was used to study a microtissue-based approach to cardiac regeneration. The importance of adhering microtissues to their surroundings to control the local mechanical environment in the microtissue was shown. Furthermore, a model was developed that describes cells sensing their mechanical environment via actin stress fibers, and responding by remodeling these actin stress fibers. In the infarcted heart, cell and stress fiber orientation were not governed by such sensing of the mechanical environment as included in the model when a microtissue was not present. In this case, collagen contact guidance may play an important role in determining cellular orientation. However, for newly forming in vitro tissue constructs the model performed well, both statically and dynamically. It can therefore be used as a tool to predict cell orientation during in vitro tissue engineering approaches and possibly in initially unstructured microtissues in the heart, and as starting-point when developing more complex models of tissue mechanics, e.g. models including collagen remodeling.

Bibliography

- [1] (2006) Diagram of the human heart. [http://en.wikipedia.org/wiki/File:Diagram_of_the_human_heart_\(cropped\).svg](http://en.wikipedia.org/wiki/File:Diagram_of_the_human_heart_(cropped).svg)
- [2] Akhyari P, Fedak PWM, Weisel RD, Lee TyJ, Verma S, Mickle DAG, Li Rk (2002) Mechanical stretch regimen enhances the formation of bioengineered autologous cardiac muscle grafts. *Circulation* 106(12 Suppl 1):I137–I142, doi: 10.1161/01.cir.0000032893.55215.fc
- [3] Akimoto S, Mitsumata M, Sasaguri T, Yoshida Y (2000) Laminar Shear Stress Inhibits Vascular Endothelial Cell Proliferation by Inducing Cyclin-Dependent Kinase Inhibitor p21Sdi1/Cip1/Waf1. *Circ Res* 86(2):185–190, doi: 10.1161/01.RES.86.2.185
- [4] Argento G (2014) Biomechanical design of an electrospun scaffold for in situ cardiovascular tissue engineering. PhD thesis, Eindhoven University of Technology
- [5] Asparuhova MB, Gelman L, Chiquet M (2009) Role of the actin cytoskeleton in tuning cellular responses to external mechanical stress. *Scand J Med Sci Sports* 19(4):490–499, doi:10.1111/j.1600-0838.2009.00928.x
- [6] Azhari H, Weiss JL, Rogers WJ, Siu CO, Shapiro EP (1995) A noninvasive comparative study of myocardial strains in ischemic canine hearts using tagged MRI in 3-D. *Am J Physiol Heart Circ Physiol* 268(5):H1918–H1926
- [7] Berry MF, Engler AJ, Woo YJ, Pirolli TJ, Bish LT, Jayasankar V, Morine KJ, Gardner TJ, Discher DE, Sweeney HL (2006) Mesenchymal stem cell injection after myocardial infarction improves myocardial compliance. *Am J Physiol Heart Circ Physiol* 290(6):H2196–H2203, doi:10.1152/ajpheart.01017.2005
- [8] Bilodeau K, Mantovani D (2006) Bioreactors for tissue engineering: focus on mechanical constraints. A comparative review. *Tissue Eng* 12(8):2367–2383, doi:10.1089/ten.2006.12.2367

- [9] Birk DE, Trelstad RL (1984) Extracellular compartments in matrix morphogenesis: collagen fibril, bundle, and lamellar formation by corneal fibroblasts. *J Cell Biol* 99(6):2024–2033
- [10] Blankesteyn WM, Creemers E, Lutgens E, Cleutjens JP, Daemen MJ, Smits JF (2001) Dynamics of cardiac wound healing following myocardial infarction: observations in genetically altered mice. *Acta Physiol Scand* 173(1):75–82, doi: 10.1046/j.1365-201X.2001.00887.x
- [11] Boateng S, Sanborn T (2013) Acute myocardial infarction. *Dis Mon* 59(3):83–96, doi:10.1016/j.disamonth.2012.12.004
- [12] Boccafoschi F, Bosetti M, Gatti S, Cannas M (2007) Dynamic fibroblast cultures: response to mechanical stretching. *Cell Adh Migr* 1(3):124–128
- [13] Boersma E, Mercado N, Poldermans D, Gardien M, Vos J, Simoons ML (2003) Acute myocardial infarction. *Lancet* 361(9360):847–858, doi:10.1016/S0140-6736(03)12712-2
- [14] Bogen DK, Rabinowitz SA, Needleman A, McMahon TA, Abelmann WH (1980) An analysis of the mechanical disadvantage of myocardial infarction in the canine left ventricle. *Circ Res* 47(5):728–741
- [15] Bovendeerd PH, Arts T, Huyghe JM, van Campen DH, Reneman RS (1992) Dependence of local left ventricular wall mechanics on myocardial fiber orientation: a model study. *J Biomech* 25(10):1129–1140
- [16] Bovendeerd PH, Arts T, Delhaas T, Huyghe JM, van Campen DH, Reneman RS (1996) Regional wall mechanics in the ischemic left ventricle: numerical modeling and dog experiments. *Am J Physiol Heart Circ Physiol* 270(1):H398–H410
- [17] Bovendeerd PHM, Kroon W, Delhaas T (2009) Determinants of left ventricular shear strain. *Am J Physiol Heart Circ Physiol* 297(3):H1058–H1068, doi: 10.1152/ajpheart.01334.2008
- [18] Boyle CJ, Lennon AB, Prendergast PJ (2011) In silico prediction of the mechanobiological response of arterial tissue: application to angioplasty and stenting. *J Biomech Eng* 133(8):081001, doi:10.1115/1.4004492
- [19] Buck RC (1980) Reorientation response of cells to repeated stretch and recoil of the substratum. *Exp Cell Res* 127(2):470–474
- [20] Burrige K, Wittchen ES (2013) The tension mounts: stress fibers as force-generating mechanotransducers. *J Cell Biol* 200(1):9–19, doi: 10.1083/jcb.201210090
- [21] Chavakis E, Koyanagi M, Dimmeler S (2010) Enhancing the outcome of cell therapy for cardiac repair: progress from bench to bedside and back. *Circulation* 121(2):325–335, doi:10.1161/CIRCULATIONAHA.109.901405

- [22] Chen TJ, Wu CC, Su FC (2012) Mechanical models of the cellular cytoskeletal network for the analysis of intracellular mechanical properties and force distributions: a review. *Med Eng Phys* 34(10):1375–1386, doi:10.1016/j.medengphy.2012.08.007
- [23] Chien K, Domian I, Parker K (2008) Cardiogenesis and the complex biology of regenerative cardiovascular medicine. *Sci Signal* 322:1494–1497
- [24] Chiron S, Tomczak C, Duperray A, Lainé J, Bonne G, Eder A, Hansen A, Eschenhagen T, Verdier C, Coirault C (2012) Complex interactions between human myoblasts and the surrounding 3D fibrin-based matrix. *PLoS One* 7(4):e36173, doi:10.1371/journal.pone.0036173
- [25] Christman KL, Lee RJ (2006) Biomaterials for the treatment of myocardial infarction. *J Am Coll Cardiol* 48(5):907–913, doi:10.1016/j.jacc.2006.06.005
- [26] Dartsch PC, Betz E (1989) Response of cultured endothelial cells to mechanical stimulation. *Basic Res Cardiol* 84(3):268–281
- [27] De Santis G, Lennon aB, Boschetti F, Verheghe B, Verdonck P, Prendergast PJ (2011) How can cells sense the elasticity of a substrate? An analysis using a cell tensegrity model. *Eur Cell Mater* 22:202–213
- [28] Deguchi S, Sato M (2009) Biomechanical properties of actin stress fibers of non-motile cells. *Biorheology* 46(2):93–105, doi:10.3233/BIR-2009-0528
- [29] Deshpande VS, McMeeking RM, Evans AG (2006) A bio-chemo-mechanical model for cell contractility. *Proc Natl Acad Sci U S A* 103(38):14015–14020, doi:10.1073/pnas.0605837103
- [30] Discher DE, Mooney DJ, Zandstra PW (2009) Growth factors, matrices, and forces combine and control stem cells. *Science* 324(5935):1673–1677, doi:10.1126/science.1171643
- [31] Driessen NJB, Mol A, Bouten CVC, Baaijens FPT (2007) Modeling the mechanics of tissue-engineered human heart valve leaflets. *J Biomech* 40(2):325–334, doi:10.1016/j.jbiomech.2006.01.009
- [32] Engler AJ, Sweeney HL, Discher DE, Schwarzbauer JE (2007) Extracellular matrix elasticity directs stem cell differentiation. *J Musculoskelet Neuronal Interact* 7(4):335
- [33] Engler AJ, Carag-Krieger C, Johnson CP, Raab M, Tang HY, Speicher DW, Sanger JW, Sanger JM, Discher DE (2008) Embryonic cardiomyocytes beat best on a matrix with heart-like elasticity: scar-like rigidity inhibits beating. *J Cell Sci* 121(Pt 22):3794–3802, doi:10.1242/jcs.029678
- [34] Estes BT, Gimble JM, Guilak F (2004) Mechanical signals as regulators of stem cell fate. *Curr Top Dev Biol* 60:91–126, doi:10.1016/S0070-2153(04)60004-4

- [35] Falschlehner C, Schaefer U, Walczak H (2009) Following TRAIL's path in the immune system. *Immunology* 127(2):145–154, doi:10.1111/j.1365-2567.2009.03058.x
- [36] Faust U, Hampe N, Rubner W, Kirchgessner N, Safran S, Hoffmann B, Merkel R (2011) Cyclic stress at mHz frequencies aligns fibroblasts in direction of zero strain. *PLoS One* 6(12):e28963, doi:10.1371/journal.pone.0028963
- [37] Fink C, Ergün S, Kralisch D, Remmers U, Weil J, Eschenhagen T (2000) Chronic stretch of engineered heart tissue induces hypertrophy and functional improvement. *FASEB J* 14(5):669–679
- [38] Fomovsky GM, Holmes JW (2010) Evolution of scar structure, mechanics, and ventricular function after myocardial infarction in the rat. *Am J Physiol Heart Circ Physiol* 298(1):H221–H228, doi:10.1152/ajpheart.00495.2009
- [39] Fomovsky GM, Macadangang JR, Ailawadi G, Holmes JW (2011) Model-based design of mechanical therapies for myocardial infarction. *J Cardiovasc Transl Res* 4(1):82–91, doi:10.1007/s12265-010-9241-3
- [40] Fomovsky GM, Clark SA, Parker KM, Ailawadi G, Holmes JW (2012) Anisotropic reinforcement of acute anteroapical infarcts improves pump function. *Circ Heart Fail* 5(4):515–522, doi:10.1161/CIRCHEARTFAILURE.111.965731
- [41] Fomovsky GM, Rouillard AD, Holmes JW (2012) Regional mechanics determine collagen fiber structure in healing myocardial infarcts. *J Mol Cell Cardiol* 52(5):1083–1090, doi:10.1016/j.yjmcc.2012.02.012
- [42] Foolen J, Deshpande VS, Kanters FMW, Baaijens FPT (2012) The influence of matrix integrity on stress-fiber remodeling in 3D. *Biomaterials* 33(30):7508–7518, doi:10.1016/j.biomaterials.2012.06.103
- [43] Fraccarollo D, Galuppo P, Bauersachs J (2012) Novel therapeutic approaches to post-infarction remodelling. *Cardiovasc Res* 94(2):293–303, doi:10.1093/cvr/cvs109
- [44] Frangi AF, Niessen WJ, Vincken KL, Viergever MA (1998) Multiscale vessel enhancement filtering. In: Wells WM, Colchester A, Delp SL (eds) *Med. Image Comput. Comput. Interv. - MICCAI'98*, Springer Berlin Heidelberg, pp 130–137, doi:10.1007/BFb0056195
- [45] Gaudette GR, Cohen IS (2006) Cardiac regeneration: materials can improve the passive properties of myocardium, but cell therapy must do more. *Circulation* 114(24):2575–2577, doi:10.1161/CIRCULATIONAHA.106.668707
- [46] Gaudron P, Eilles C, Kugler I, Ertl G (1993) Progressive left ventricular dysfunction and remodeling after myocardial infarction. Potential mechanisms and early predictors. *Circulation* 87(3):755–763, doi:10.1161/01.CIR.87.3.755

- [47] Gauvin R, Parenteau-Bareil R, Larouche D, Marcoux H, Bisson F, Bonnet A, Auger FA, Bolduc S, Germain L (2011) Dynamic mechanical stimulations induce anisotropy and improve the tensile properties of engineered tissues produced without exogenous scaffolding. *Acta Biomater* 7(9):3294–3301, doi:10.1016/j.actbio.2011.05.034
- [48] Ghibaudo M, Saez A, Trichet L, Xayaphoummine A, Browaeys J, Silberzan P, Buguin A, Ladoux B (2008) Traction forces and rigidity sensing regulate cell functions. *Soft Matter* 4(9):1836–1843, doi:10.1039/b804103b
- [49] Goldstein JA (2012) Acute right ventricular infarction: insights for the interventional era. *Curr Probl Cardiol* 37(12):533–557, doi:10.1016/j.cpcardiol.2012.05.001
- [50] Gould RA, Chin K, Santisakultarm TP, Dropkin A, Richards JM, Schaffer CB, Butcher JT (2012) Cyclic strain anisotropy regulates valvular interstitial cell phenotype and tissue remodeling in three-dimensional culture. *Acta Biomater* 8(5):1710–1719, doi:10.1016/j.actbio.2012.01.006
- [51] Grenier G, Rémy-Zolghadri M, Larouche D, Gauvin R, Baker K, Bergeron F, Dupuis D, Langelier E, Rancourt D, Auger Fa, Germain L (2005) Tissue reorganization in response to mechanical load increases functionality. *Tissue Eng* 11(1-2):90–100, doi:10.1089/ten.2005.11.90
- [52] Guccione JM, Moonly SM, Moustakidis P, Costa KD, Moulton MJ, Ratcliffe MB, Pasque MK (2001) Mechanism underlying mechanical dysfunction in the border zone of left ventricular aneurysm: a finite element model study. *Ann Thorac Surg* 71(2):654–662
- [53] Gupta KB, Ratcliffe MB, Fallert MA, Edmunds LH, Bogen DK (1994) Changes in passive mechanical stiffness of myocardial tissue with aneurysm formation. *Circulation* 89(5):2315–2326
- [54] Hamilton DW, Maul TM, Vorp DA (2004) Characterization of the response of bone marrow-derived progenitor cells to cyclic strain: implications for vascular tissue-engineering applications. *Tissue Eng* 10(3-4):361–369, doi:10.1089/107632704323061726
- [55] Henshaw DR, Attia E, Bhargava M, Hannafin JA (2006) Canine ACL fibroblast integrin expression and cell alignment in response to cyclic tensile strain in three-dimensional collagen gels. *J Orthop Res* 24(3):481–490, doi:10.1002/jor.20050
- [56] Hirayama Y, Sumpio BE (2007) Role of ligand-specific integrins in endothelial cell alignment and elongation induced by cyclic strain. *Endothelium* 14(6):275–283, doi:10.1080/10623320701746248
- [57] Holmes JW, Yamashita H, Waldman LK, Covell JW (1994) Scar remodeling and transmural deformation after infarction in the pig. *Circulation* 90(1):411–420

- [58] Holmes JW, Nuñez JA, Covell JW (1997) Functional implications of myocardial scar structure. *Am J Physiol Heart Circ Physiol* 272(5):H2123–H2130
- [59] Holmes JW, Borg TK, Covell JW (2005) Structure and mechanics of healing myocardial infarcts. *Annu Rev Biomed Eng* 7:223–253, doi: 10.1146/annurev.bioeng.7.060804.100453
- [60] Hu S, Eberhard L, Chen J, Love JC, Butler JP, Fredberg JJ, Whitesides GM, Wang N (2004) Mechanical anisotropy of adherent cells probed by a three-dimensional magnetic twisting device. *Am J Physiol Cell Physiol* 287(5):C1184–C1191, doi:10.1152/ajpcell.00224.2004
- [61] Jacot JG, Martin JC, Hunt DL (2010) Mechanobiology of cardiomyocyte development. *J Biomech* 43(1):93–98, doi:10.1016/j.jbiomech.2009.09.014
- [62] Janz RF, Waldron RJ (1978) Predicted effect of chronic apical aneurysms on the passive stiffness of the human left ventricle. *Circ Res* 42(2):255–263, doi: 10.1161/01.RES.42.2.255
- [63] Jeremy RW, Allman KC, Bautovitch G, Harris PJ (1989) Patterns of left ventricular dilation during the six months after myocardial infarction. *J Am Coll Cardiol* 13(2):304–310
- [64] Jiang XJ, Wang T, Li XY, Wu DQ, Zheng ZB, Zhang JF, Chen JL, Peng B, Jiang H, Huang C, Zhang XZ (2009) Injection of a novel synthetic hydrogel preserves left ventricle function after myocardial infarction. *J Biomed Mater Res A* 90(2):472–477, doi:10.1002/jbm.a.32118
- [65] Johnson TD, Christman KL (2013) Injectable hydrogel therapies and their delivery strategies for treating myocardial infarction. *Expert Opin Drug Deliv* 10(1):59–72, doi:10.1517/17425247.2013.739156
- [66] de Jonge N, Kanters FMW, Baaijens FPT, Bouten CVC (2013) Strain-induced collagen organization at the micro-level in fibrin-based engineered tissue constructs. *Ann Biomed Eng* 41(4):763–774, doi:10.1007/s10439-012-0704-3
- [67] Jungbauer S, Gao H, Spatz JP, Kemkemer R (2008) Two characteristic regimes in frequency-dependent dynamic reorientation of fibroblasts on cyclically stretched substrates. *Biophys J* 95(7):3470–3478, doi: 10.1529/biophysj.107.128611
- [68] de Kam PJ, Nicolosi GL, Voors AA, van den Berg MP, Brouwer J, van Veldhuisen DJ, Barlera S, Maggioni AP, Giannuzzi P, Temporelli PL, Latini R, van Gilst WH (2002) Prediction of 6 months left ventricular dilatation after myocardial infarction in relation to cardiac morbidity and mortality. Application of a new dilatation model to GISSI-3 data. *Eur Heart J* 23(7):536–542, doi: 10.1053/euhj.2001.2820

- [69] Kaunas R, Nguyen P, Usami S, Chien S (2005) Cooperative effects of Rho and mechanical stretch on stress fiber organization. *Proc Natl Acad Sci U S A* 102(44):15895–15900, doi:10.1073/pnas.0506041102
- [70] Kaunas R, Usami S, Chien S (2006) Regulation of stretch-induced JNK activation by stress fiber orientation. *Cell Signal* 18(11):1924–1931, doi:10.1016/j.cellsig.2006.02.008
- [71] Kaunas R, Hsu HJ, Deguchi S (2011) Sarcomeric model of stretch-induced stress fiber reorganization. *Cell Health Cytoskelet* 3(1):13–22, doi:10.2147/CHC.S14984
- [72] Kerckhoffs RCP, Bovendeerd PHM, Kotte JCS, Prinzen FW, Smits K, Arts T (2003) Homogeneity of cardiac contraction despite physiological asynchrony of depolarization: a model study. *Ann Biomed Eng* 31(5):536–547, doi:10.1114/1.1566447
- [73] Kikuchi K, Poss K (2012) Cardiac regenerative capacity and mechanisms. *Annu Rev Cell Dev Biol* 28:719–741, doi:10.1146/annurev-cellbio-101011-155739.Cardiac
- [74] Knöll R, Marston S (2012) On mechanosensation, acto/myosin interaction, and hypertrophy. *Trends Cardiovasc Med* 22(1):17–22, doi:10.1016/j.tcm.2012.06.005
- [75] Korhonen RK, Julkunen P, Wilson W, Herzog W (2008) Importance of collagen orientation and depth-dependent fixed charge densities of cartilage on mechanical behavior of chondrocytes. *J Biomech Eng* 130(2):021003, doi:10.1115/1.2898725
- [76] Kortsmits J, Davies NH, Miller R, Macadangdang JR, Zilla P, Franz T (2013) The effect of hydrogel injection on cardiac function and myocardial mechanics in a computational post-infarction model. doi:10.1080/10255842.2012.656611, <http://www.ncbi.nlm.nih.gov/pubmed/22439799>
- [77] Langer F, Rodriguez F, Cheng A, Ortiz S, Harrington KB, Zasio MK, Daughters GT, Criscione JC, Ingels NB, Miller DC (2007) Alterations in lateral left ventricular wall transmural strains during acute circumflex and anterior descending coronary occlusion. *Ann Thorac Surg* 84(1):51–60, doi:10.1016/j.athoracsur.2007.03.041
- [78] Lebedev VI, Laikov DN (1999) A quadrature formula for the sphere of the 131st algebraic order of accuracy. *Dokl Math* 59(3):477–481
- [79] Lee IC, Wang JH, Lee YT, Young TH (2007) The differentiation of mesenchymal stem cells by mechanical stress or/and co-culture system. *Biochem Biophys Res Commun* 352(1):147–152, doi:10.1016/j.bbrc.2006.10.170
- [80] Lee J, Terracciano CM (2010) Cell therapy for cardiac repair. *Br Med Bull* 94:65–80, doi:10.1093/bmb/ldq005

- [81] Legant WR, Pathak A, Yang MT, Deshpande VS, McMeeking RM, Chen CS (2009) Microfabricated tissue gauges to measure and manipulate forces from 3D microtissues. *Proc Natl Acad Sci U S A* 106(25):10097–10102, doi: 10.1073/pnas.0900174106
- [82] Li S, Guan JL, Chien S (2005) Biochemistry and biomechanics of cell motility. *Annu Rev Biomed Eng* 7:105–150, doi: 10.1146/annurev.bioeng.7.060804.100340
- [83] Lipinski MJ, Biondi-Zoccai GGL, Abbate A, Khianey R, Sheiban I, Bartunek J, Vanderheyden M, Kim HS, Kang HJ, Strauer BE, Vetrovec GW (2007) Impact of intracoronary cell therapy on left ventricular function in the setting of acute myocardial infarction: a collaborative systematic review and meta-analysis of controlled clinical trials. *J Am Coll Cardiol* 50(18):1761–1767, doi: 10.1016/j.jacc.2007.07.041
- [84] Lo CM, Wang HB, Dembo M, Wang YL (2000) Cell movement is guided by the rigidity of the substrate. *Biophys J* 79(1):144–152, doi:10.1016/S0006-3495(00)76279-5
- [85] Loerakker S, Obbink-Huizer C, Baaijens FPT (2013) A physically motivated constitutive model for cell-mediated compaction and collagen remodeling in soft tissues. *Biomech Model Mechanobiol* doi:10.1007/s10237-013-0549-1
- [86] Malliaras K, Marban E (2011) Cardiac cell therapy: where we've been, where we are, and where we should be headed. *Br Med Bull* 98(1):161–185, doi: 10.1093/bmb/ldr018
- [87] Mann DL (1999) Mechanisms and models in heart failure: A combinatorial approach. *Circulation* 100(9):999–1008
- [88] Marieb EN (2004) Human anatomy and physiology. 6th edn, Pearson Benjamin Cummings, San Francisco, chap 18, pp 676–707
- [89] van Marion M (2013) The interplay between the extracellular environment and cardiomyocyte progenitor cells for material based cardiac repair. PhD thesis, Eindhoven University of Technology
- [90] van Marion MH, Bax NAM, van Spreeuwel ACC, van der Schaft DWJ, Bouten CVC (2013) Material-based Engineering Strategies for Cardiac Regeneration. *Curr Pharm Des*
- [91] Martin-Rendon E, Brunskill S, Dorée C, Hyde C, Watt S, Mathur A, Stanworth S (2008) Stem cell treatment for acute myocardial infarction. *Cochrane Database Syst Rev* (4):CD006536, doi:10.1002/14651858.CD006536.pub2
- [92] McCain ML, Parker KK (2011) Mechanotransduction: the role of mechanical stress, myocyte shape, and cytoskeletal architecture on cardiac function. *Pflugers Arch* 462(1):89–104, doi:10.1007/s00424-011-0951-4

- [93] Mofrad MR (2009) Rheology of the Cytoskeleton. *Annu Rev Fluid Mech* 41(1):433–453, doi:10.1146/annurev.fluid.010908.165236
- [94] Mookadam F, Moustafa SE (2009) Prevention of late postmyocardial infarction left ventricular remodeling: an update. *Curr Heart Fail Rep* 6(4):245–253
- [95] Moore GW, Hutchins GM, Bulkley BH, Tseng JS, Ki PF (1980) Constituents of the human ventricular myocardium: connective tissue hyperplasia accompanying muscular hypertrophy. *Am Heart J* 100(5):610–616
- [96] Mulvihill BM, Prendergast PJ (2008) An algorithm for bone mechanore-sponsiveness: implementation to study the effect of patient-specific cell mechanosensitivity on trabecular bone loss. *Comput Methods Biomech Biomed Engin* 11(5):443–451, doi:10.1080/10255840802136150
- [97] Nash M, Hunter P (2000) Computational mechanics of the heart. *J Elast* 61(1):113–141, doi:10.1023/A:1011084330767
- [98] Neidlinger-Wilke C, Grood ES, Wang JH-C, Brand RA, Claes L (2001) Cell alignment is induced by cyclic changes in cell length: studies of cells grown in cyclically stretched substrates. *J Orthop Res* 19(2):286–293, doi:10.1016/S0736-0266(00)00029-2
- [99] Nemir S, West JL (2010) Synthetic materials in the study of cell response to substrate rigidity. *Ann Biomed Eng* 38(1):2–20, doi:10.1007/s10439-009-9811-1
- [100] Ngu H, Feng Y, Lu L, Oswald SJ, Longmore GD, Yin FCP (2010) Effect of focal adhesion proteins on endothelial cell adhesion, motility and orientation response to cyclic strain. *Ann Biomed Eng* 38(1):208–222, doi:10.1007/s10439-009-9826-7
- [101] Nguyen TD, Liang R, Woo SLy, Burton SD, Wu C, Almarza A, Sacks MS, Abramowitch S (2009) Effects of cell seeding and cyclic stretch on the fiber remodeling in an extracellular matrix-derived bioscaffold. *Tissue Eng Part A* 15(4):957–963, doi:10.1089/ten.tea.2007.0384
- [102] Nieponice A, Maul TM, Cumer JM, Soletti L, Vorp DA (2007) Mechanical stimulation induces morphological and phenotypic changes in bone marrow-derived progenitor cells within a three-dimensional fibrin matrix. *J Biomed Mater Res A* 81(3):523–530, doi:10.1002/jbm.a.31041
- [103] Obbink-Huizer C, Oomens CWJ, Loerakker S, Foolen J, Bouten CVC, Baaijens FPT (2014) Computational model predicts cell orientation in response to a range of mechanical stimuli. *Biomech Model Mechanobiol* 13(1):227–236, doi:10.1007/s10237-013-0501-4
- [104] Omens JH, Milkes DE, Covell JW (1995) Effects of pressure overload on the passive mechanics of the rat left ventricle. *Ann Biomed Eng* 23(2):152–163

- [105] Omens JH, Miller TR, Covell JW (1997) Relationship between passive tissue strain and collagen uncoiling during healing of infarcted myocardium. *Cardiovasc Res* 33(2):351–358
- [106] Pelham RJ, Wang YI (1997) Cell locomotion and focal adhesions are regulated by substrate flexibility. *Proc Natl Acad Sci U S A* 94(25):13661–13665
- [107] Perl M, Horowitz A (1987) Mechanical model for the simulation of ischaemia and infarction of the left ventricle. *Med Biol Eng Comput* 25(3):284–288
- [108] Perl M, Horowitz A, Sideman S (1986) Comprehensive model for the simulation of left ventricle mechanics. Part 1. Model description and simulation procedure. *Med Biol Eng Comput* 24(2):145–149
- [109] Pfeffer MA, Braunwald E (1990) Ventricular remodeling after myocardial infarction. Experimental observations and clinical implications. *Circulation* 81(4):1161–1172
- [110] Porter KE, Turner NA (2009) Cardiac fibroblasts: at the heart of myocardial remodeling. *Pharmacol Ther* 123(2):255–278, doi: 10.1016/j.pharmthera.2009.05.002
- [111] Quarterman RL, Moonly S, Wallace AW, Guccione J, Ratcliffe MB (2002) A finite element model of left ventricular cellular transplantation in dilated cardiomyopathy. *ASAIO J* 48(5):508–513, doi: 10.1097/01.MAT.0000026353.66193.6B
- [112] Rane AA, Chuang JS, Shah A, Hu DP, Dalton ND, Gu Y, Peterson KL, Omens JH, Christman KL (2011) Increased infarct wall thickness by a bio-inert material is insufficient to prevent negative left ventricular remodeling after myocardial infarction. *PLoS One* 6(6):e21571, doi:10.1371/journal.pone.0021571
- [113] Ravichandran R, Venugopal JR, Sundarajan S, Mukherjee S, Ramakrishna S (2012) Minimally invasive cell-seeded biomaterial systems for injectable/epicardial implantation in ischemic heart disease. *Int J Nanomedicine* 7:5969–5994, doi:10.2147/IJN.S37575
- [114] Reinecke H, Minami E, Zhu WZ, Laflamme MA (2008) Cardiogenic differentiation and transdifferentiation of progenitor cells. *Circ Res* 103(10):1058–1071, doi:10.1161/CIRCRESAHA.108.180588
- [115] Ricca BL, Venugopalan G, Fletcher DA (2013) To pull or be pulled: parsing the multiple modes of mechanotransduction. *Curr Opin Cell Biol* 25(5):558–564, doi:10.1016/j.ceb.2013.06.002
- [116] Riehl BD, Park JH, Kwon IK, Lim JY (2012) Mechanical stretching for tissue engineering: two-dimensional and three-dimensional constructs. *Tissue Eng Part B Rev* 18(4):288–300, doi:10.1089/ten.TEB.2011.0465

- [117] Robey TE, Saiget MK, Reinecke H, Murry CE (2008) Systems approaches to preventing transplanted cell death in cardiac repair. *J Mol Cell Cardiol* 45(4):567–581, doi:10.1016/j.yjmcc.2008.03.009
- [118] Rouillard AD, Holmes JW (2012) Mechanical regulation of fibroblast migration and collagen remodeling in healing myocardial infarcts. *J Physiol* 590:4585–4602, doi:10.1113/jphysiol.2012.229484
- [119] Saez A, Ghibaudo M, Buguin A, Silberzan P, Ladoux B (2007) Rigidity-driven growth and migration of epithelial cells on microstructured anisotropic substrates. *Proc Natl Acad Sci U S A* 104(20):8281–8286, doi:10.1073/pnas.0702259104
- [120] Safran SA, De R (2009) Nonlinear dynamics of cell orientation. *Phys Rev E* 80(6):4–7, doi:10.1103/PhysRevE.80.060901
- [121] Samarel AM (2005) Costameres, focal adhesions, and cardiomyocyte mechanotransduction. *Am J Physiol Heart Circ Physiol* 289(6):H2291–H2301, doi:10.1152/ajpheart.00749.2005
- [122] Savadjiev P, Strijkers GJ, Bakermans AJ, Piuze E, Zucker SW, Siddiqi K (2012) Heart wall myofibers are arranged in minimal surfaces to optimize organ function. *Proc Natl Acad Sci U S A* 109(24):9248–9253, doi:10.1073/pnas.1120785109
- [123] Schulman I, Hare J (2012) Key developments in stem cell therapy in cardiology. *Regen Med* 7:17–24
- [124] Schwarz US, Safran SA (2013) Physics of adherent cells. *Rev Mod Phys* 85(3):1327–1381
- [125] Shirinsky VP, Antonov AS, Birukov KG, Sobolevsky AV, Romanov YA, Kabaeva NV, Antonova GN, Smirnov VN (1989) Mechano-chemical control of human endothelium orientation and size. *J Cell Biol* 109(1):331–339
- [126] Singelyn JM, Christman KL (2010) Injectable materials for the treatment of myocardial infarction and heart failure: the promise of decellularized matrices. *J Cardiovasc Transl Res* 3(5):478–486, doi:10.1007/s12265-010-9202-x
- [127] Stamenović D, Ingber DE (2002) Models of cytoskeletal mechanics of adherent cells. *Biomech Model Mechanobiol* 1(1):95–108, doi:10.1007/s10237-002-0009-9
- [128] Standley PR, Cammarata A, Nolan BP, Purgason CT, Stanley MA, Camaratta A (2002) Cyclic stretch induces vascular smooth muscle cell alignment via NO signaling. *Am J Physiol Heart Circ Physiol* 283(5):H1907–H1914, doi:10.1152/ajpheart.01043.2001
- [129] Stopak D, Harris AK (1982) Connective tissue morphogenesis by fibroblast traction. I. Tissue culture observations. *Dev Biol* 90(2):383–398, doi:10.1016/0012-1606(82)90388-8

- [130] Stops AJF, Harrison NM, Haugh MG, O'Brien FJ, McHugh PE (2010) Local and regional mechanical characterisation of a collagen-glycosaminoglycan scaffold using high-resolution finite element analysis. *J Mech Behav Biomed Mater* 3(4):292–302, doi:10.1016/j.jmbbm.2009.12.003
- [131] Streeter DD, Spotnitz HM, Patel DP, Ross J, Sonnenblick EH (1969) Fiber orientation in the canine left ventricle during diastole and systole. *Circ Res* 24(3):339–347
- [132] Stricker J, Falzone T, Gardel ML (2010) Mechanics of the F-actin cytoskeleton. *J Biomech* 43(1):9–14, doi:10.1016/j.jbiomech.2009.09.003
- [133] Sun Y, Weber KT (2000) Infarct scar: a dynamic tissue. *Cardiovasc Res* 46(2):250–256
- [134] Takehara N, Matsubara H (2011) Cardiac regeneration therapy: connections to cardiac physiology. *Am J Physiol Heart Circ Physiol* 301(6):H2169–H2180, doi:10.1152/ajpheart.00768.2011
- [135] Terrovitis JV, Smith RR, Marbán E (2010) Assessment and optimization of cell engraftment after transplantation into the heart. *Circ Res* 106(3):479–494, doi:10.1161/CIRCRESAHA.109.208991
- [136] Thygesen K, Alpert JS, White HD, Jaffe AS, Apple FS, Galvani M, Katus HA, Newby LK, Ravkilde J, Chaitman B, Clemmensen PM, Dellborg M, Hod H, Porela P, Underwood R, Bax JJ, Beller G, Bonow R, Van der Wall EE, Bassand JP, Wijns W, Ferguson TB, Steg PG, Uretsky BF, Williams DO, Armstrong PW, Antman EM, Fox KA, Hamm CW, Ohman EM, Simoons ML, Poole-Wilson PA, Gurfinkel EP, Lopez-Sendon JL, Pais P, Mendis S, Zhu JR, Walentin LC, Fernández-Avilés F, Fox KM, Parkhomenko AN, Priori SG, Tendera M, Voipio-Pulkki LM, Vahanian A, Camm AJ, De Caterina R, Dean V, Dickstein K, Filippatos G, Funck-Brentano C, Hellemans I, Kristensen SD, McGregor K, Sechtem U, Silber S, Widimsky P, Zamorano JL, Morais J, Brener S, Harrington R, Morrow D, Lim M, Martinez-Rios Ma, Steinhubl S, Levine GN, Gibler WB, Goff D, Tubaro M, Dudek D, Al-Attar N (2007) Universal definition of myocardial infarction. *Circulation* 116(22):2634–2653, doi:10.1161/CIRCULATIONAHA.107.187397
- [137] Tondon A, Hsu HJ, Kaunas R (2011) Dependence of cyclic stretch-induced stress fiber reorientation on stretch waveform. *J Biomech* 45(5):728–735, doi:10.1016/j.jbiomech.2011.11.012
- [138] Topalian S, Ginsberg F, Parrillo JE (2008) Cardiogenic shock. *Crit Care Med* 36(1 (Suppl)):S66–S74, doi:10.1097/01.CCM.0000296268.57993.90
- [139] Topol EJ (2003) Current status and future prospects for acute myocardial infarction therapy. *Circulation* 108(16 Suppl 1):III6–III13, doi:10.1161/01.CIR.0000086950.37612.7b

- [140] Ubbink SWJ, Bovendeerd PHM, Delhaas T, Arts T, van de Vosse FN (2006) Towards model-based analysis of cardiac MR tagging data: relation between left ventricular shear strain and myofiber orientation. *Med Image Anal* 10(4):632–641, doi:10.1016/j.media.2006.04.001
- [141] Vanhoutte D, Schellings M, Pinto Y, Heymans S (2006) Relevance of matrix metalloproteinases and their inhibitors after myocardial infarction: a temporal and spatial window. *Cardiovasc Res* 69(3):604–613, doi:10.1016/j.cardiores.2005.10.002
- [142] Vernerey FJ, Farsad M (2011) A constrained mixture approach to mechanosensing and force generation in contractile cells. *J Mech Behav Biomed Mater* 4(8):1683–1699, doi:10.1016/j.jmbbm.2011.05.022
- [143] Villarreal FJ, Lew WY, Waldman LK, Covell JW (1991) Transmural myocardial deformation in the ischemic canine left ventricle. *Circ Res* 68(2):368–381, doi:10.1161/01.RES.68.2.368
- [144] Walker JC, Ratcliffe MB, Zhang P, Wallace AW, Fata B, Hsu EW, Saloner D, Guccione JM (2005) MRI-based finite-element analysis of left ventricular aneurysm. *Am J Physiol Heart Circ Physiol* 289(2):H692–H700, doi:10.1152/ajpheart.01226.2004
- [145] Wall ST, Walker JC, Healy KE, Ratcliffe MB, Guccione JM (2006) Theoretical impact of the injection of material into the myocardium: a finite element model simulation. *Circulation* 114(24):2627–2635, doi:10.1161/CIRCULATIONAHA.106.657270
- [146] Wall ST, Yeh CC, Tu RYK, Mann MJ, Healy KE (2010) Biomimetic matrices for myocardial stabilization and stem cell transplantation. *J Biomed Mater Res A* 95(4):1055–1066, doi:10.1002/jbm.a.32904
- [147] Wallace WA, Yu PN (1975) Sudden death and the pre-hospital phase of acute myocardial infarction. *Annu Rev Med* 26(12):1–7, doi:10.1146/annurev.me.26.020175.000245
- [148] Wang F, Guan J (2010) Cellular cardiomyoplasty and cardiac tissue engineering for myocardial therapy. *Adv Drug Deliv Rev* 62(7-8):784–797, doi:10.1016/j.addr.2010.03.001
- [149] Wang H, Ip W, Boissy R, Grood ES (1995) Cell orientation response to cyclically deformed substrates: experimental validation of a cell model. *J Biomech* 28(12):1543–1552
- [150] Wang JHC, Jia F, Gilbert TW, Woo SLY (2003) Cell orientation determines the alignment of cell-produced collagenous matrix. *J Biomech* 36(1):97–102
- [151] Wehrens XHT, Doevendans PA (2004) Cardiac rupture complicating myocardial infarction. *Int J Cardiol* 95(2-3):285–292, doi:10.1016/j.ijcard.2003.06.006

- [152] Wei HM, Wong P, Hsu LF, Shim W (2009) Human bone marrow-derived adult stem cells for post-myocardial infarction cardiac repair: current status and future directions. *Singapore Med J* 50(10):935–942
- [153] Wei Z, Deshpande VS, McMeeking RM, Evans AG (2008) Analysis and interpretation of stress fiber organization in cells subject to cyclic stretch. *J Biomech Eng* 130(3):031009, doi:10.1115/1.2907745
- [154] Wenk JF, Wall ST, Peterson RC, Helgerson SL, Sabbah HN, Burger M, Stander N, Ratcliffe MB, Guccione JM (2009) A method for automatically optimizing medical devices for treating heart failure: designing polymeric injection patterns. *J Biomech Eng* 131(12):121011, doi:10.1115/1.4000165
- [155] Whittaker P (1998) Collagen organization in wound healing after myocardial injury. *Basic Res Cardiol* 93 Suppl 3:23–25
- [156] Whittaker P, Boughner DR, Kloner RA (1989) Analysis of healing after myocardial infarction using polarized light microscopy. *Am J Pathol* 134(4):879–893
- [157] Wickline SA, Verdonk ED, Wong AK, Shepard RK, Miller JG (1992) Structural remodeling of human myocardial tissue after infarction. Quantification with ultrasonic backscatter. *Circulation* 85(1):259–268, doi:10.1161/01.CIR.85.1.259
- [158] Wille JJ, Ambrosi CM, Yin FCP (2004) Comparison of the effects of cyclic stretching and compression on endothelial cell morphological responses. *J Biomech Eng* 126(5):545, doi:10.1115/1.1798053
- [159] Wilson W, van Donkelaar C, van Rietbergen B, Ito K, Huiskes R (2004) Stresses in the local collagen network of articular cartilage: a poroviscoelastic fibril-reinforced finite element study. *J Biomech* 37(3):357–366, doi:10.1016/S0021-9290(03)00267-7
- [160] Wilson W, van Donkelaar CC, van Rietbergen B, Huiskes R (2005) A fibril-reinforced poroviscoelastic swelling model for articular cartilage. *J Biomech* 38(6):1195–1204, doi:10.1016/j.jbiomech.2004.07.003
- [161] Wilson W, Huyghe JM, van Donkelaar CC (2007) Depth-dependent compressive equilibrium properties of articular cartilage explained by its composition. *Biomech Model Mechanobiol* 6(1-2):43–53, doi:10.1007/s10237-006-0044-z
- [162] Wyatt KEK, Bourne JW, Torzilli Pa (2009) Deformation-dependent enzyme mechanokinetic cleavage of type I collagen. *J Biomech Eng* 131(5):051004, doi:10.1115/1.3078177
- [163] Yan KC, Nair K, Sun W (2010) Three dimensional multi-scale modelling and analysis of cell damage in cell-encapsulated alginate constructs. *J Biomech* 43(6):1031–1038, doi:10.1016/j.jbiomech.2009.12.018

- [164] Yasuda S, Shimokawa H (2009) Acute myocardial infarction: the enduring challenge for cardiac protection and survival. *Circ J* 73:2000–2008
- [165] Ye Z, Zhou Y, Cai H, Tan W (2011) Myocardial regeneration: Roles of stem cells and hydrogels. *Adv Drug Deliv Rev* 63(8):688–697, doi: 10.1016/j.addr.2011.02.007
- [166] Yettram AL, Vinson CA, Gibson DG (1979) Influence of the distribution of stiffness in the human left ventricular myocardium on shape change in diastole. *Med Biol Eng Comput* 17(5):553–562
- [167] Yoshigi M, Clark EB, Yost HJ (2003) Quantification of stretch-induced cytoskeletal remodeling in vascular endothelial cells by image processing. *Cytometry A* 55(2):109–118, doi:10.1002/cyto.a.10076
- [168] Zemel A, Rehfeldt F, Brown AEX, Discher DE, Safran SA (2010) Optimal matrix rigidity for stress fiber polarization in stem cells. *Nat Phys* 6(6):468–473, doi:10.1038/nphys1613
- [169] Zhu JH, Chen CL, Flavahan S, Harr J, Su B, Flavahan NA (2011) Cyclic stretch stimulates vascular smooth muscle cell alignment by redox-dependent activation of Notch3. *Am J Physiol Heart Circ Physiol* 300(5):H1770–H1780, doi: 10.1152/ajpheart.00535.2010
- [170] Zimmerman SD, Karlon WJ, Holmes JW, Omens JH, Covell JW (2000) Structural and mechanical factors influencing infarct scar collagen organization. *Am J Physiol Heart Circ Physiol* 278(1):H194–H200

Samenvatting

Een hartaanval of hartinfarct is één van de meest voorkomende doodsoorzaken in de westerse wereld. De zuurstoftoevoer naar een deel van het hart wordt onderbroken, waardoor daar massaal cardiomyocyten (hartspiercellen) sterven. Omdat het natuurlijke vermogen van het hart om zichzelf te herstellen beperkt is, wordt er na een infarct littekenweefsel gevormd dat niet kan samentrekken. Hierdoor functioneert het hart minder goed. Het kan op lange termijn leiden tot schadelijke remodelering van het hart en uiteindelijk hartfalen. Er is onderzoek gedaan naar therapieën die gebruik maken van stamcellen om hartinfarctpatiënten te behandelen, met als doel om het spierweefsel in het hart te regenereren (herscheppen). Helaas is de gunstige werking van stamceltherapieën tot nog toe maar beperkt. Slechts een klein deel van de cellen die in het hart gebracht worden blijven daar ook en de stamcellen die blijven, differentiëren vrijwel nooit tot cardiomyocyten. Er is gedacht dat de stamcellen beter in het hart blijven zitten wanneer ze ingebed worden in een biomateriaal en zo kleine weefselachtige structuren (microweefsels) vormen. Het gebruik van een biomateriaal zorgt er voor, dat er meer controle mogelijk is over de lokale omgeving van de cel. Omdat cellen gevoelig zijn voor de mechanica van hun omgeving, is het te verwachten dat meer controle over de omgeving van cellen leidt tot meer controle over het gedrag van de cellen. Om de cellen een werkend onderdeel van het hart te laten zijn, moet er niet alleen aan een aantal biologische vereisten voldaan worden; het is ook nodig dat de cellen de juiste richting hebben. Het doel van dit proefschrift was het ontwikkelen van een theoretisch raamwerk en computermodel om, met het oog op het regenereren van het hart met behulp van microweefsels, de oriëntatie van cellen in reactie op mechanische stimulansen te analyseren en voorspellen.

Als eerste stap richting dit doel is onderzocht in hoeverre de lokale mechanische omgeving van cellen in een microweefsel beheerst kan worden (hoofdstuk 2). De lokale mechanische omgeving van de cellen wordt deels bepaald door de eigenschappen van het microweefsel, zoals de microweefselstijfheid die door de cellen waargenomen kan worden, en deels door de mechanica van het hart als geheel (de macro-omgeving), waaronder de ritmische vervorming van het hart die leidt tot vervorming van microweefsels in het hart. Om te bepalen wat de invloed van de stijfheid van het microweefsel op de vervorming van het microweefsel is, werd een computer-

model van een bolvormig microweefsel omgeven door een vervormende omgeving gebruikt. Bij vermindering van de microweefselstijfheid nam de microweefselrek toe; er was dus enige controle over de rek van het microweefsel mogelijk via de stijfheid van het microweefsel. Echter, de maximale gemiddelde microweefselrek was slechts $2^{1/2}$ keer de rek die opgelegd werd aan de omgeving, terwijl de microweefselstijfheid een honderdste van de stijfheid van de omgeving was. Dit betekent dat er slechts binnen een beperkt bereik controle over de microweefselrek via de microweefselstijfheid mogelijk was. Ook was de rek verschillend in verschillende delen van het microweefsel. Hoe groot dit effect was, hing af van de manier waarop microweefsel en omgeving met elkaar verbonden waren. Het effect was het kleinst wanneer ze zowel in normaal- als in afschuifrichting aan elkaar verbonden waren. Deze heterogeniteit perkt het bereik waarbinnen controle over de microweefselrek mogelijk is verder in. De in dit hoofdstuk beschreven resultaten kunnen gebruikt worden om in te schatten welke rekniveaus realistisch zijn om tijdens in vitro experimenten op te leggen. Ook laten de resultaten zien dat het gunstig is om microweefsels aan hun omgeving vast te zetten wanneer controle over de rek in het microweefsel belangrijk is.

In hoofdstuk 3 werd de aandacht verschoven naar de celschaal en celoriëntatie. Veel hechtende cellen hebben interne vezels, vooral in de lengterichting van de cel. Cellen kunnen spanning uitoefenen op hun omgeving via deze vezels, die 'stress-fibers' (*spanningsvezels*) worden genoemd en een moleculaire opbouw hebben die lijkt op die van spiervezels. Er werd een computermodel ontwikkeld om de opbouw en afbraak van stress-fibers te beschrijven. In het model konden stress-fibers aangemaakt worden in een aantal richtingen. De spanning in stress-fibers in elke richting was gebaseerd op het Hill model, een veelgebruikt model om de kracht die een spier levert te beschrijven. Deze spanning was maximaal wanneer rek en verkortingsnelheid gelijk waren aan nul en nam af wanneer de absolute rek en verkortingsnelheid toenamen. Een hoge spanning in stress-fibers in een bepaalde richting leidde tot een toegenomen stress-fiberproductie in deze richting. Met dit model ontwikkelden zich vooral stress-fibers loodrecht op richtingen die cyclisch gerekt werden, in de stijfste richting op een anisotrope ondergrond en in de ingeklemde richting wanneer andere richtingen niet ingeklemd waren, zelfs als deze ingeklemde richting cyclisch gerekt werd. Al deze fenomenen zijn ook in in vitro modelsystemen waargenomen. Deze resultaten laten zien dat het model veelbelovend is als hulpmiddel om de oriëntatie van cellen als reactie op mechanische stimulansen te analyseren en voorspellen.

Als volgende stap (hoofdstuk 4) werd het model toegepast op kleine 3D weefsels. Deze weefsel werden of in één richting (uniaxiaal) of in twee richtingen (biaxiaal) ingeklemd. Hierdoor ervoeren cellen in elk van de weefseltypen een verschillende mechanische omgeving. Door de specifieke manier waarop de weefsels ingeklemd werden, was de lokale mechanische omgeving binnenin elk weefsel heterogeen. Derhalve was een grondige validatie van het model mogelijk door deze experimenten te simuleren en een kwantitatieve vergelijking te maken tussen de gesimuleerde en experimentele stress-fiberoriëntatie in elk deel van de weefsels. In zowel experiment als simulatie ontwikkelden zich vooral stress-fibers in richtingen waarin de weerstand tegen vervorming groot was. In het midden van biaxiaal ingeklemde weefsels was de weerstand hoog in alle richtingen en was er geen voorkeursrichting. Voor uniaxiaal ingeklemde weefsels en bij de rand van de weefsels was de weerstand tegen

vervorming loodrecht op de rand of ingeklemde richting lager. Hierdoor ontstond een oriëntatie in ingeklemde richting of parallel aan de rand. Over het algemeen kwamen de experimentele en gesimuleerde stress-fiberdistributies kwantitatief overeen.

In hoofdstuk 5 werd het ontwikkelde model toegepast op het hart. In weefsels zoals myocardium hebben cellen en collageenvezels normaal gesproken dezelfde richting. Door de celoriëntatie die door het model voorspeld wordt te vergelijken met een experimenteel waargenomen collageenoriëntatie, is het mogelijk om te bepalen of het waarschijnlijk is dat de overeenkomende oriëntatie veroorzaakt wordt door de cellen. De stress-fiberoriëntatie werd voorspeld op basis van de lokale vervorming in een geïnfarceerd hart, die werd bepaald met een bestaand model van de linker ventrikel. De voorspelde oriëntatie werd vergeleken met een experimenteel waargenomen collageenoriëntatie die in de literatuur beschreven is, voor infarcten op verschillende plekken (apex en midden op het ventrikel) en met verschillende vormen. Voor het infarct bij de apex werd voorspeld dat er geen voorkeursrichting was. Dit kwam overeen met de experimenteel waargenomen collageenoriëntatie. Echter, voor de infarcten midden op het ventrikel werd, ongeacht de infarctvorm, een voorkeur voor de longitudinale richting voorspeld, terwijl een circumferentiële collageenoriëntatie experimenteel was waargenomen. Als de vervorming van de cel vergelijkbaar is met de vervorming van geïnfarceerd hartweefsel, dan is de waargenomen collageenoriëntatie niet het gevolg van collageen dat in dezelfde richting gaat liggen als cellen, die oriënteren op basis van hun mechanische omgeving. Dit geeft aan dat het ontwikkelde model in de huidige toestand niet direct toegepast kan worden op het geïnfarceerde hart en wijst richting de lokale structuur (bijvoorbeeld de lokale collageenoriëntatie) als belangrijk aspect van de omgeving van de cel. Het is interessant om in de toekomst het model uit te breiden met de lokale structuur en de neiging van cellen om parallel aan die structuur te gaan liggen (*contact guidance*).

Al met al laat dit proefschrift zien dat computermodelleren een wezenlijke bijdrage kan leveren aan het begrijpen en voorspellen van celoriëntatiegedrag, wat belangrijk is voor strategieën om het hart te repareren, bijvoorbeeld door microweefsels te injecteren.

Dankwoord

Hoewel alleen mijn naam op het kaft staat, was dit proefschrift er nooit gekomen als ik het helemaal alleen had moeten doen. Daarom wil ik graag de volgende mensen bedanken:

- *Mijn (co-)promotoren*: Bedankt voor de kans om te promoveren en jullie begeleiding, enthousiasme en vermogen steeds het meeste uit mijn resultaten te halen. *Frank*, jouw snelle en scherpe inzichten gaven vaak nieuwe richting aan dit project. *Carlijn*, jouw drive voor zowel wetenschap als mensen is heel bijzonder. Bedankt ook voor het uitzonderlijk nauwkeurig lezen van alles wat ik geschreven heb. *Cees*, jouw deur stond altijd open; bedankt voor je peptalks en je vaste vertrouwen dat mijn werk de moeite waard is.
- *Professors Doevendans, Deshpande and Van de Vosse, and René van Donkelaar*: Thank you for taking the time to review my thesis and for taking part in the committee.
- *Jasper*: Jouw experimenten waren een bron van inspiratie voor mij. Bedankt voor de prettige samenwerking die resulteerde in de artikelen die als hoofdstuk 3 en 4 in dit proefschrift zijn opgenomen.
- *Peter Bovendeerd*: Het combineren van beide modellen leverde nieuwe inzichten op, al was het niet altijd wat we hoopten. Bedankt voor de hulp en het meedenken.
- *Mieke*: We hebben niet zo veel samengewerkt als ik in het begin verwachtte, maar het was goed om samen in SMARTCARE te zitten, en we hebben toch maar mooi allebei een boekje gemaakt (en een dochter gekregen). Fijn dat je mijn paranimf wilt zijn!
- *My fellow modellers, including Sandra, Giulia and Sol*: I've appreciated and enjoyed our biweekly meetings and discussions. It was good not to be the single soul on the 'modeling-island' in the STBE-group!
- *The cardiac regeneration groep, in het bijzonder Noortje, Ariane, Mieke en Carlijn*: Al was ik een beetje een vreemde eend in de bijt, het was erg interessant

om iets meer te begrijpen van jullie manier om naar het hart te kijken. En daarnaast is zijn jullie een erg gezellige en hartelijke groep!

- *My office-mates in WH 4.11*: I've truly appreciated the working atmosphere in 4.11, quiet enough to work, but also suitable to share the small joys, annoyances and questions of every day PhD student life. *Anna Catharina*, het was gezellig om gedurende al die 4 jaar van mijn promotie tegenover je te zitten. Ik ben blij dat je er 30 oktober bij zult zijn als mijn paranimf.
- En verder iedereen op vloer 4 die de werktijd, (lunch)pauzes, cursussen en congressen makkelijker en leuker heeft gemaakt: bedankt!
- *Ichthus Zeilkampen*: Ontspanning is ook broodnodig en hoe kan dat beter dan in the middle of nowhere (a.k.a. Sandfirden) op een zeilboot? Ik wil alle mensen die ik de afgelopen jaren bij Ichthus Zeilkampen heb ontmoet hartelijk bedanken voor de mooie weekends en weken, waarin ik veel geleerd heb, niet alleen over bomen, schoten, kikkers en lijken, maar ook over vertrouwen hebben en ervoor gaan.
- *Mijn vrienden — met name Claire, Evianne, Marleen & Joris, Renske, Cora & Carst, Lisanne & Elbert, Bert & Hanna, Arjan & Judith, Christiaan & Lia en de Tribunalisten*: Bedankt voor alle spelletjes, zwemuurtjes, thee, bruiloften, zeilpartijen en gewoon het samenzijn!
- *Mijn familie — papa & mama, Lydia & Jörgen, Yvonne, oma, Henk & Elske, Wouter, Jorien & Geoffrey, Robbert en Wessel, Maurits en Anna Querinda*: Bedankt voor jullie interesse in mij en mijn onderzoek en de gezelligheid van het bij elkaar zijn en horen. *Papa en mama*, fijn dat ik bij jullie altijd thuis mag zijn (ook letterlijk in het eerste jaar!) *Henk en Elske*, ik kan me geen fijnere schoonouders wensen! *Yvonne*, ook voor jou een speciaal woordje, ik vind het jammer dat je er nu niet bij kan zijn, maar ik ben blij en trots dat je de persoon bent die je bent, wat er voor zorgt dat je er nu niet bij bent. *Anna Querinda*, toen ik begon met promoveren had ik totaal niet gedacht dat jij er nu zou zijn, en nu je er bent, blijf ik me verwonderen over hoe mooi, gaaf en tov je bent! Daarbij valt een proefschrift in het niet. *Maurits*, je bent een deel van mij geworden... Jouw relativeringsvermogen en humor houden mij stabiel en het leven is zo veel rijker met jou! Ik kijk uit naar alle avonturen die we hopelijk nog samen mogen beleven.
- *Mijn hemelse God, Vader en Redder*: U bent de oorsprong van mijn leven en ik heb U elke stap van de weg nodig (gehad).

Curriculum Vitae

Christine Obbink-Huizer was born on 28 March 1986 in Veldhoven, The Netherlands. After finishing secondary school (gymnasium) in 2004 at Christiaan Huygens College in Eindhoven, she obtained her bachelor's degree in biomedical engineering at Eindhoven University of Technology in 2007. She then moved to Enschede and obtained her master's degree in biomedical engineering at Twente University in 2009. She graduated within the Laboratory of Biomechanical Engineering on "The influence of the rib cage on the mechanical behavior of the ten year old spine — a finite element study". In the same year, she started a PhD project at Eindhoven University of Technology, department of Biomedical Engineering, Soft Tissue Biomechanics and Engineering group, of which the results are presented in this dissertation. Since 2013 she is employed in the same group as a researcher.

List of Publications

- **C. Obbink-Huizer**, C.W.J. Oomens, P.H.M. Bovendeerd, C.V.C. Bouten, F.P.T. Baaijens *Collagen and fibroblast orientation in the infarcted heart: cause and consequence*. Manuscript in preparation.
- G. Argento, **C. Obbink-Huizer**, E. Fioretta, C.W.J. Oomens, C.V.C. Bouten, F.P.T. Baaijens *Influence of substrate geometry on cell contact guidance*. Manuscript in preparation.
- **C. Obbink-Huizer**, J. Foolen, C.W.J. Oomens, M. Borochin, C.S. Chen, C.V.C. Bouten, F.P.T. Baaijens (2014) *Computational and experimental investigation of local stress fiber orientation in uniaxially and biaxially constrained microtissues*. Biomech Model Mechanobiol. doi: 10.1007/s10237-014-0554-z. Available online.
- S. Loerakker, **C. Obbink-Huizer**, F.P.T. Baaijens (2013) *A physically motivated constitutive model for cell-mediated compaction and collagen remodeling in soft tissues*. Biomech Model Mechanobiol. doi: 10.1007/s10237-013-0549-1. Available online.
- **C. Obbink-Huizer**, C.W.J. Oomens, S. Loerakker, J. Foolen, C.V.C. Bouten, F.P.T. Baaijens (2014) *Computational model predicts cell orientation in response to a range of mechanical stimuli*. Biomech Model Mechanobiol. 13(1):227-236 doi: 10.1007/s10237-013-0501-4